STRUCTURE-FUNCTION RELATIONSHIPS IN THE AUDITORY BRAINSTEM

Sarah Gleiss

Graduate School of
Systemic Neurosciences
LMU Munich

STRUCTURE-FUNCTION RELATIONSHIPS IN THE AUDITORY BRAINSTEM

Sarah Gleiss

Dissertation der Graduate School of Systemic Neurosciences

der

Ludwig-Maximilians-Universität München

03.05.2017

First reviewer and supervisor: Prof. Dr. Felix Felmy

Second reviewer: Prof. Dr. Benedikt Grothe

Third reviewer: Dr. Ana Magnusson

Date of oral defense: 21.02.2017

Contents

Abstract

Neurons of nuclei in the auditory brainstem show a high degree of specialization towards the integration of incoming auditory stimuli. As the function of the medial superior olive (MSO) and dorsal nucleus of lateral lemniscus (DNLL) are known these are structures ideally suited to investigate structure-function relationships during development as well as in the mature system.

Neurons in the MSO are known to compute sound source location by the precise integration of synaptic inputs. Thereby they are able to resolve interaural time differences (ITDs) with submillisecond precision. Towards this fast signal integration MSO neurons show biophysical and synaptical specializations. The main biophysical specialization being the developmentally downregulated input resistance that enables a faster membrane time constant. The basis for this decreased input resistance is thought to be the presence of hyperpolarization activated cation and voltage-gated potassium channels. So far studies on voltage-gated potassium channels focused on the presence of low voltage activated potassium channels. It is not expected though that these are the only potassium channels present. In fact, a whole subset of different voltage gated potassium channels was found to be expressed in the mature MSO.

Additionally, during development excitatory and inhibitory inputs refine towards an anatomical arrangement with mainly somatic inhibition and dendritic excitation. The refinement of inhibitory inputs happens during late postnatal development and has been shown to be experience-dependent. Neither the time window nor the exact refinements of excitatory inputs has been studied yet, nor

whether these refinements are also dependent on experience.

I could show that excitatory inputs refine from N-Methyl-D-Aspartat receptor (NMDAR) and α-amino-3-hydroxy-5-methyl-4-isoxazolepropionic acid receptor (AMPAR) currents to mainly AMPAR currents after postnatal day (P)13. This developmental refinement period is accompanied by a period of high NMDAR currents and calcium permeability of the present receptors at P13 indicating a time window for plasticity around this age. Most of these refinements seemed to happen independent of experience. Further, the data suggests that some refinements of excitatory inputs are most likely activity-dependent.

The MSO sends its ITD information as a rate code to the DNLL. Here, the information content is enhanced in comparison to the MSO. The DNLL is special as it has two forms of inhibition that work on very different time scales. Its physiological hallmark is a slow reciprocal inhibition that has been implicated in echo suppression and can outlast auditory stimulation by tens of milliseconds. The presence of NMDARs in the mature DNLL is established *in-vitro* and indicated in vivo, but their computational and functional role for information processing has not yet been fully elucidated. Using in vivo experiments it could be shown that NMDARs increase the overall firing rate, thereby decreasing the length of persistent inhibition in a level dependent way.

1. Introduction

All sensory systems are able to extract and interpret different physical parameters from the surrounding world. In contrast to other sensory systems, the auditory system faces a special task, as the spatial representation of different sound sources is not encoded in the auditory periphery. Thus, the relevant auditory information must be extracted from subtle cues. Another main difference to other sensory systems is the presence of at least three additional synapses between the sound waves that hit the ear and the auditory cortex. This indicates the need for complex computations in the auditory nuclei up-stream of the cochlea. In addition, the information content representation increases on the way from the cochlea to the auditory nuclei and stresses the need for their high specialization. This high degree of neuronal specialization in the auditory brainstem is united by a main common motive; the quest for precise temporal computation.

In the following studies, this high degree of neuronal specialization is used to investigate structure-function relationships in the mature and the developing system. To point out their degree of specialization, relevant structures, their neuronal morphology and biophysical properties are reviewed. Additionally, a short overview of developmental processes and their dependency on correlated temporal cues is provided.

1.1 Cues for sound localization

One example for fast signal integration in the auditory brainstem is the extraction of sound source location. Sound source location can be analyzed in

different ways either depending on monaural or binaural cues. On the one hand, the sound energy across different frequency bands is compared (spectral cues; Blauert, 1997; Figure 1, A) or the difference in movement of the two eardrums is analyzed (Grothe et al., 2010). While spectral cues are monaural cues in the vertical plane, the latter are binaural cues. Binaural cues are analyzed in two different ways, either by comparing the interaural time difference (ITD; Figure 1, C) or interaural level difference (ILD; Figure 1, B).

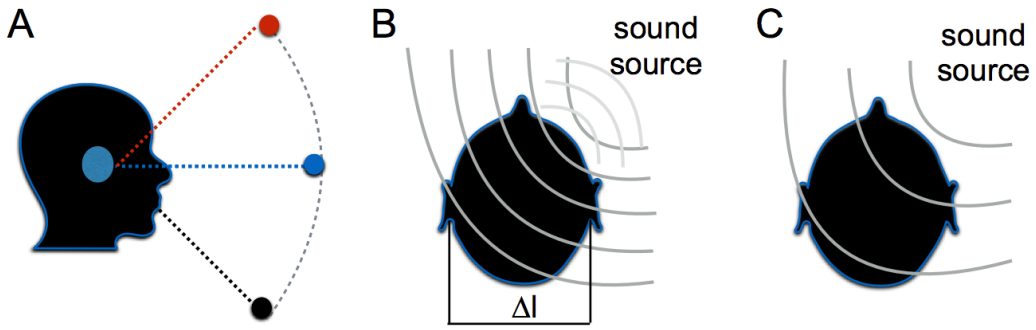

Figure 1: Different strategies to extract sound location. A: Spectral notches are monaural cues that can be used to localize a sound source. Here, the interaction of a broadband sound with the head shows that mostly the outer ear is used to extract sound location. When the sound source is shifted from below to above the horizon the central notch shifts to higher frequencies. B: ILDs are used for the detection of high frequencies above ~ 2 kHz. Here, the shadowing effect of the head attenuates the level of the sound at the ear further from the source. C: ITDs are used for frequencies below 2 kHz. Here, the physical separation of the ears causes sounds arriving from the side hit to the closer ear first. Modified after Grothe et al., 2010.

ILDs are created by the shadowing effect of the head, which occurs at frequencies higher than ~2 kHz. This shadowing creates increasingly large differences in the intensity of sounds at the two ears (for review see: Grothe et al., 2010; Figure 1, B). ILDs are thought to be computed in the lateral superior olive (LSO; Boudreau & Tsuchitani, 1968). The LSO gets excitatory inputs from spherical bushy cells in the ipsilateral anteroventral cochlear nucleus. Globular

bushy cells from the contralateral antero-ventral cochlear nucleus send inhibitory projections via the medial trapezoid body (MNTB). The computation of these inputs leads to the characteristic ILD function. In the LSO, neurons are mainly excited by sounds from the ipsilateral side and inhibited from sounds on the contralateral side (Boudreau et al., 1968).

In contrast to high frequency sounds (> 2 kHz), low frequency sounds (< 2 kHz) are not attenuated enough by the head to create ILDs. Instead, for low frequencies, the difference in the arrival times at the two ears is used to localize a sound. This only works for frequencies with a longer wavelength than head width, roughly frequencies lower than ~2 kHz. Thus, the smallest detectable ITD is dependent on head size. In humans for example the smallest detectable ITD is ~10 µs but in gerbils it is no more than 100 ms (for review see: Grothe, 2003; Grothe & Pecka, 2014).

ITDs are computed by neurons in the medial superior olive (MSO) that are able to detect the arrival times of sounds in a sub-millisecond time scale. Therefore, they have to compute the incoming excitatory and inhibitory inputs in an extremely precise manner, much more than many other neurons in the brain. It has been shown that the excitation alone is not enough to resolve ITDs, and thereby sound source location. But that inhibition plays a crucial role in shifting the peak of the rate response curve into the physiological relevant range (Brand et al., 2002; Grothe et al., 2010; McAlpine et al., 2001; Myoga et al., 2014). Thus, the incoming excitation forms the framework towards ITD detection, while the inhibition is important towards the fine-tuning of ITD curves, and consequently exact sound localization.

1.2 Neuronal basis for ITD computation

Neurons in the MSO are highly specialized for rapid computation. They show several specializations in their neuronal morphology towards this function, as well as their synaptic inputs and intrinsic electrophysiological properties. They have a bipolar morphology and typically one to two dendrites emerging from each soma side 180° to each other (Figure 2, B). MSO neurons are arranged in a single para-sagittal plane with their dendrites extending orthogonally with respect to the dorso-ventral axis of the nucleus (Rautenberg et al., 2009; Stotler, 1953). Distal parts of MSO dendrites have been shown to increase in diameter and thereby decrease axial resistance during development (Rautenberg et al., 2009).

The excitatory inputs are mainly mediated by AMPARs (Couchman et al.; 2012) and emerge from spherical bushy cells of the cochlear nuclei (Figure 2, A; Grothe et al., 2010). Inhibition most likely comes from both LNTBs and the MNTB that in turn receives rapid excitation from globular bushy cells (Figure 2, A). This inhibition is fast, phase-locked (Grothe, 2003; Magnusson et al., 2005; McAlpine et al., 2002; Smith et al., 1998) and has been shown to play a role in adjusting the slope of the ITD (Brand et al., 2002; Myoga et al., 2014; but see: Roberts et al., 2013; van der Heijden et al., 2013). An additional specialization of these excitatory and inhibitory inputs is their synaptic arrangement with dendritic excitation and mainly somatic inhibition (Figure 2, B; Couchman et al., 2012).

ITD computation is based not only on the integration of these fast, excitatory glutamatergic with fast glycinergic inhibitory inputs, but also on many biophysical specializations, which enable fast signal integration (Smith et al., 2000; Myoga et al., 2009; Golding et al., 2012).

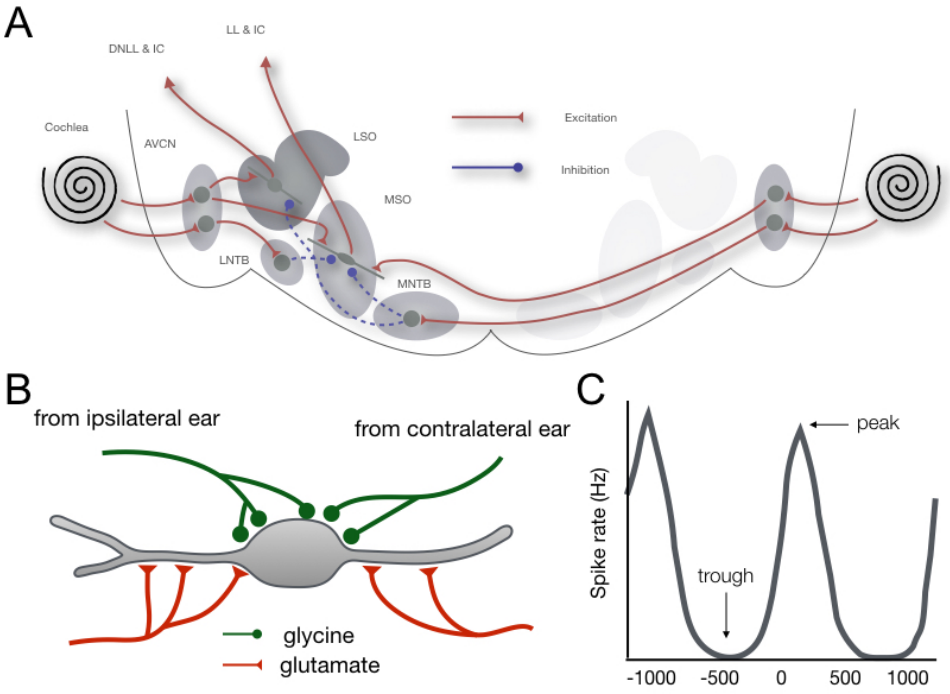

Figure 2: MSO input pattern. A: SOC circuit and inputs to the MSO. Excitatory inputs come from ipsi- and contralateral antero-ventral cochlear nucleus. Inhibition comes from ipsilateral LNTB and MNTB. B: Anatomical organization of excitatory and inhibitory inputs. Glutamatergic excitation mainly targets the dendrites of mature MSO neurons while inhibition is soma-targeted. C: Typical ITD function of a MSO neuron. Y-axis is the spike rate in Hz and x-axis shows ITD in µs. (Adapted from Grothe et al., 2010; Couchman et al., 2012)

During development, MSO neurons decrease their input resistance to decrease their membrane time constant to enable faster input integration (Scott et al., 2005). This decrease in input resistance is based on the presence of voltage-gated ion channels, as hyperpolarization activated cation channels (I_h; Baumann et al., 2013; Khurana et al., 2012) and voltage-gated potassium channels (Lv; Barnes-Davies et al., 2004; Khurana et al., 201; Mathews et al., 2010; Scott et al., 2005). Potassium currents bring the membrane potential closer to the potassium equilibrium potential and thus away from the firing threshold.

1.2.1 AMPARs and NMDARs

In general, the in the MSO mainly present AMPARs are low-affinity ionotropic transmembrane receptors gated by glutamate that mediate fast excitatory neurotransmission (Zito et al., 2009; for reviews see, Dingledine et al., 1999; König et al., 2000). Therefore AMPARs are ideally suited for fast signal integration in the MSO. Their channel kinetics and permeability, also to calcium depend on their subunit composition (Hollmann & Heinemann, 1994). AMPARs are pentameric complexes that are composed of up to four different subunits (for review see Trussell et al., 1999). These are named GluR1 – GluR4, each of which is subject to alternative splicing into flip/flop variants as well as RNA editing (Hollmann & Heinemann, 1994). AMPARs containing flop dominated splice variants (Lambolez et al., 1996; Mosbacher et al., 1994) and especially those that are composed mainly of GluR4 and lack GluR2 have the fastest channel kinetics (Geiger et al., 1995; Mosbacher et al., 1994). In the vast majority of AMPARs the GluR4 subunit predominates (fore review see, Dingledine et al., 1999). While the GluR4 subunit has high calcium permeability (Jonas et al., 1994), the GluR2 subunit mediates calcium impermeability (Burnashev et al., 1992; Geiger et al., 1995; König et al., 2001). During development AMPAR kinetics increase, for example the fast and slow time constants of AMPAR time constants decrease (Koike-Tani et al., 2005).

Additionally, the deactivation time constant becomes faster (Koike-Tanie et al., 2005) thereby potentially shaping the decay of excitatory postsynaptic currents (Koike-Tanie et al., 2005). Thus, developmental changes in AMPARs can shape synaptic transmission. In the mature MSO AMPARs are the receptors that are

predominantly present mainly at the dendrites (Clark 1969; Couchman et al., 2012; Kil et al., 1995; Smith et al., 1993; Stotler 1953).

NMDARs are high-affinity ionotropic receptors that are also gated by glutamate (Schneggenburger et al., 1993). In general, they show high calcium permeability and a voltage-dependent magnesium block (Burnashev et al., 1995; Schneggenburger et al., 1993). NMDAR opening requires the coincidence of both presynaptic glutamate release and a strong postsynaptic depolarization to relive the magnesium block of the channel (Mayer et al., 1984; Nowak et al., 1984). Functional NMDARs are heteromers that consist of two obligatory GluN1 subunits and two regulatory subunits. Usually the regulatory subunits are GluN2 subunits, of which four isoforms are known to exist (GluN2A, B, C and D). Channels that contain the GluN2A and B subunit are more sensitive to magnesium block compared to GluN2C or D containing channels (Monyer et al., 1994). The obligatory GluN1 subunit also contains the allosteric glycine-binding site of the receptor (Furukawa et al., 2005).

1.2.2 Potassium channels

Potassium channels are important for many neuronal functions, including action potential repolarization, resting membrane potential, excitability, and spiking characteristics (for reviews see: Gutman et al., 2005; Johnston et al., 2010). They are generally separated into high-voltage activated (HVA) and low-voltage activated (LVA) channels. HVA channels are generally more relevant for suprathreshold events, because of the high voltage required to open them, whereas LVA channels are more relevant for subthreshold dynamics, as they are

more prone to be opened at rest (for reviews see: Gutman et al., 2005; Johnston et al., 2010).

For example Kv2 and Kv3 belong to the HVA channel family (for review see: Gutman et al., 2005). Whereby, LVA channels open upon small depolarizations from resting membrane potential. Kv1, Kv4 and Kv7 channels belong to the LVA channels (for review see: Gutman et al., 2005). These channels can thereby shape EPSP size and influence AP coupling. Another type of LVA channel needs prior hyperpolarization and creates a transient potassium channel current the so called A-type current (Johnston et al., 2008). An example for an A-type current mediating channel is Kv4 (for review see Gutman et al., 2005).

Neurons in the MNTB of mice express a multitude of Kv channels. In the MNTB the LVA channels Kv1.1 and Kv1.2 are important for AP timing and low jitter (Brew & Forsythe, 1995; Dodson et al., 2002; Gittelman & Tempel, 2006; Kopp-Scheinpflug et al., 2003), while Kv3 channels enable high firing rates (Brew & Forsythe, 1995; Rudy & McBain, 2001; Wang et al., 1998a). Thus, showing that a multitude of Kv channels is required for correct functioning of a neuron.

However, in the MSO, only the presence of LVA channels has been shown so far (Scott et al., 2005; Mathews et al., 2010). LVA channels in the MSO are biased towards soma and proximal dendrites, and the presence of mainly Kv1.1 within the MSO has been hypothesized (Scott et al., 2005; Mathews et al., 2010). Somatically expressed LVA channels mediating the A-type current could be activated by prior hyperpolarization through an IPSP. They could then play a role in shifting the EPSP peak towards ITD detection (Myoga et al., 2014). Additionally, simulated EPSPs at the distal dendrites of MSO neurons reach deflections of up

to 70 mV (Mathews et al., 2010). Consequently, EPSPs at the distal dendrites of MSO neurons could activate HVA channels.

Taken together, MSO neurons show several biophysical specializations towards fast signal integration. After initial connections are formed they undergo several refinement processes. With these refinement processes synapses are strengthened or weakened and thereby their projection pattern can change.

1.3 Circuit formation

During developmental circuit formation, precisely organized and adjusted synaptic inputs have to be established. One of the first steps is the migration of neurons to their target location, followed by axonal pathfinding and crude topography generation. These can depend on activity-independent and -dependent processes. Activity-independent processes often depend on genetic factors, usually the expression of different guidance cues (Cramer et al., 2014; Howell et al., 2007). Alternatively, activity-dependent processes can depend on internal factors such as spontaneous activity or external factors such as sensory-evoked activity (Figure 3; Cramer et al., 2014; Friauf et al., 1999). Early axonal pathfinding is mostly an activity-independent process because it depends on the expression of transcription factors and guidance molecules (for review see Caines & Cook; 1995; Tessier-Lavigne & Goodman, 1996). In the auditory system, axons of the ventral cochlear nucleus cross the midline and project bilaterally to the superior olivary complex (SOC) by using *netrin-1* and *slit-1* as guidance molecules (Howell et al., 2007).

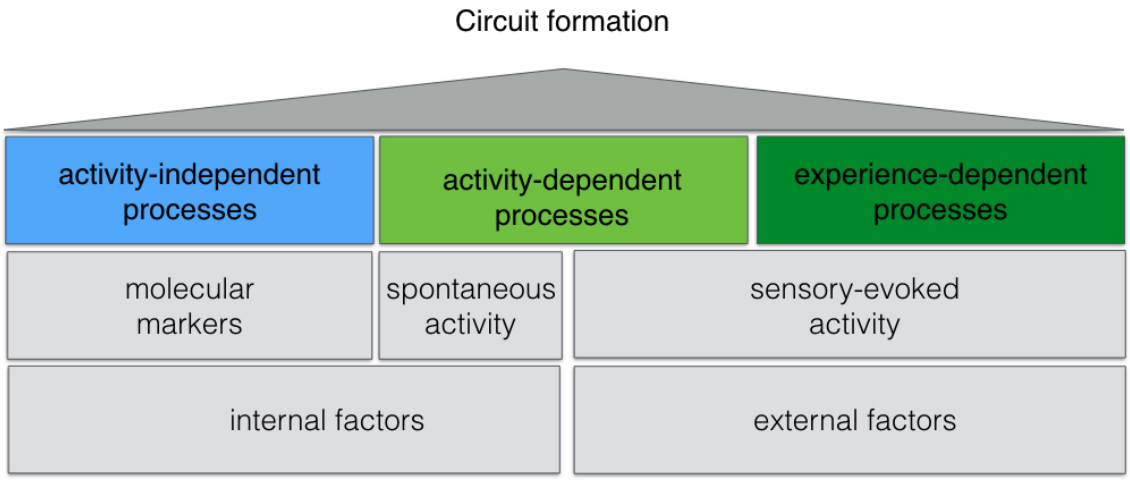

Figure 3: Circuit formation depends on activity-independent as well as activity-dependent processes. Experience has also been shown to have an influence on circuit refinement processes. Activity-independent processes depend on the expression of molecular markers that in turn depends on internal factors. In contrast, activity-dependent processes depend on spontaneous activity and sensory-evoked activity. Spontaneous activity also relies on internal factors. However, sensory-evoked activity involves input from the external world to drive neuronal activity. The same is true for experience-dependent processes that are also dependent on the external world. Here, the difference to activity-dependent processes is that they are patterned cues that have the spatio-temporal properties as in the natural environment. Modified from Friauf & Lohmann, 1999.

The formation of topographically organized synaptic inputs to LSO, MSO and MNTB happens already before or around birth (Kandler et al., 1993; Sanes et al., 1993; Smith et al., 2000; Taschenberger et al., 2000), showing that crude circuit formation and tonotopic organization is independent of acoustically evoked activity (Kandler & Friauf, 1993; Kil et al., 1995; Person et al., 2004; Sanes & Takacs, 1993). However, spontaneous activity that is generated by transmitter release in the inner ear and activates auditory nerve fibers (Beutner et al., 2001; Glowatzki et al., 2002; Johnson et al., 2011; Tritsch et al., 2007, 2010) could guide the process in an activity-dependent way. As has been shown for the visual system, for example, where spontaneous activity generated in the retina plays a role during the formation of the retinogeniculate projection (Shatz, 1990a).

For refinements of the established connections in the auditory brainstem activity, driven synaptic transmission has been shown to be important (Rogowski et al., 1981; Walger et al., 1993, 1997). Central mechanisms that underly activity-dependent synaptic refinements include long-term potentiation, depression (LTP, LTD, respectively; for review see Malenka & Bear, 2004) and spike time dependent plasticity (for review see Debanne & Poo, 2010). LTP has been defined as a long-lasting increase in synaptic efficacy following a brief high-frequency stimulation (Bliss et al., 1973), while LTD describes the activity-dependent reduction in the efficacy of synapses, generally from lower frequency stimulation. STDP also takes the timing of the incoming inputs into account (for review see Debanne & Po, 2010), where only synaptic inputs timed in close relation to spiking output are modified. For the MSO it has been proposed that inhibitory synapses are refined by STDP mechanisms (Leibold & van der Hemmen, 2005). In this case, inhibitory synapses that fired before the occurrence of a MSO AP are strengthened, and those that fired simultaneously or later are weakened (Leibold & van der Hemmen, 2005). Indeed, inhibitory inputs have been shown to be developmentally refined from dendritic and somatic targeted to somatic targeted inhibition (Kapfer et al., 2002; Werthat et al., 2008). This refinement has been shown to be disrupted when exposing the animals to omnidirectional noise during late postnatal development (Kapfer et al., 2002; Werthat et al., 2008). This absence of most spatial cues prevented synaptic pruning of glycinergic inputs (Kapfer et al., 2002; Werthat et al., 2008) and eliminated ITD tuning asymmetry (Kapfer et al., 2002; Magnusson et al., 2005; Seidl & Grothe, 2005; Werthat et al., 2008). The found ITD tuning asymmetry of noise-reared animals resembled that

found when blocking glycinergic inhibition (Brand et al., 2002; Seidl & Grothe, 2005). Thus, binaural input with temporal correlation is important for the refinement of inhibitory inputs. Therefore STDP seems to be the mechanism by which inhibitory inputs are refined (Leibold & van der Hemmen, 2005). There is currently no clear experimental proof for which kind of plasticity mechanism is present in the MSO. Additionally, the refinement processes of excitatory inputs and whether they also depend on experience have not been investigated, yet.

There are also refinement processes that are activity but not experience-dependent. This has been shown for the visual system, where dark-rearing lead to only modest changes in orientation selectivity but lid suture had devastating effects (White et al., 2001). Thus, it is important to differentiate between activity-, and not experience-dependent refinement processes. In the remainder of this work, “activity-dependent processes” will be referred to as dependent on activity *per se.* Thus, omnidirectional noise means high rates of binaural activity that show no or little temporal correlation. “Experience-dependent processes” will be seen as dependent on the experience of stimuli with correlated temporal features. Consequently, refinement processes that depend on experience will be persistently disturbed when put in omnidirectional noise. In contrast, activity-dependent processes will refine or even show a faster maturation.

In general, another of way of developmentally enhancing temporal is to decrease cell capacity by reducing dendritic complexity (Rautenberg et al., 2009; Rietzel et al., 1998). Additionally, the synaptic morphology can change (Ford et al., 2009) allowing faster clearance of the synaptic cleft (Cathala et al., 2003) and accelerating the decay times of synaptic currents. A change in receptor

composition as well as receptor subunit composition can lead to accelerated synapse kinetics (for review see: Takahashi).

NMDAR mediated synaptic activity together with a postsynaptic increase in calcium, has been shown to be essential for activity-dependent refinement processes in the mammalian brain (Malenka et al., 2004). The NMDAR is special in that sense as it serves as a coincidence detector itself. It needs presynaptic activation for glutamate release together with postsynaptic depolarization to remove the magnesium block (Mayer et al., 1984, Nowak et al., 1984). Thus, NMDAR plasticity mechanisms are based on a coincidence detector formed by the voltage-dependent magnesium block (Forsythe et al., 1988; Mayer et al., 1984; Nowak et al., 1984), which is supposed to suppress NMDAR signaling at resting potentials (Kleinschmidt et al., 1987; Constantine-Paton, 1998).

Due to their slow kinetics, NMDARs would be expected to be developmentally downregulated in the auditory system (Futai et al., 2001; Franks et al., 2005). Nevertheless, in some auditory nuclei, NMDARs persist throughout development. For example in the MNTB and the DNLL NMDAR, currents accelerate and are maintained during maturity (Steinert et al., 2010). However, their synaptic current is small and their functional role most likely changes during development. It has been proposed that NMDAR calcium permeability could play a role in nitric oxide signaling (Steinert et al., 2010).

However, MSO neurons are not that fast from hearing onset, also biophysiological cell properties have to develop towards faster signal processing. This development towards ITD detection in the gerbil MSO outlasts late postnatal development. Its neurons show ITD sensitivity already around P15 (Seidl & Grothe,

2005). Around P10 and P12 the initial phase of hearing onset occurs, their thresholds reach adult levels and the ITD curve is fine-tuned around P15 (McFadden et al., 1996; Seidl & Grothe, 2005; Woolf et al., 1984). This is achieved amongst others, by decreasing the input resistance, which decreases the membrane time constant like in other nuclei (Franzen et al., 2015; Kandler et al., 1995; Magnusson et al., 2005; Scott et al., 2005). This developmental decrease in input resistance is mostly due to the increase in co-expression of hyperpolarization activated cation and Kv1 potassium channels (Bal & Oertel, 2000; Baumann et al., 2013; Golding et al., 1995; Khurana et al., 2011; Leao et al., 2006; Mathews et al., 2010), as well as a decrease in dendritic arborisation (Rautenberg et al., 2009). Thereby MSO neurons have a large resting conductance that in turn reduces the membrane time constant. These changes again lead to changes in AP properties as measured at the soma, for example their half-width, amplitude and shape as described for the MSO (Scott et al., 2005) and the MNTB (Taschenberger et al., 2000).

1.4 Persistent inhibition

The MSO together with the contralateral LSO send their excitatory projections to the ipsilateral dorsal nucleus of lateral lemniscus (DNLL; Glendenning et al., 1981; Shneiderman et al., 1988; Oliver, 2000; Siveke et al., 2006; Kelly et al., 2009). One of the two present types of inhibition in the DNLL operates on a slower time scale than the so far discussed ITD computation. This slow pathway in the DNLL is mediated via a reciprocal inhibitory GABAergic projection from the contralateral DNLL (Figure 4, Adams et al., 1984; Chen et al.,

1999; Kelly et al., 2009). It generates a long-lasting inhibition that can outlast an auditory stimulus by tens of milliseconds (Figure 4, Burger et al., 2001; Pecka et al., 2007; Yang et al., 1994). This so-called persistent inhibition is one of the main physiological hallmarks of DNLL neurons and has been implicated in the suppression of sound information during reverberations (Ammer et al., 2012; Burger et al., 2001; Pecka et al., 2007; Yang et al., 1994). Neurons in the DNLL are able to maintain firing rates in response to high input frequencies by NMDAR-dependent amplification of firing (Porres et al., 2011).

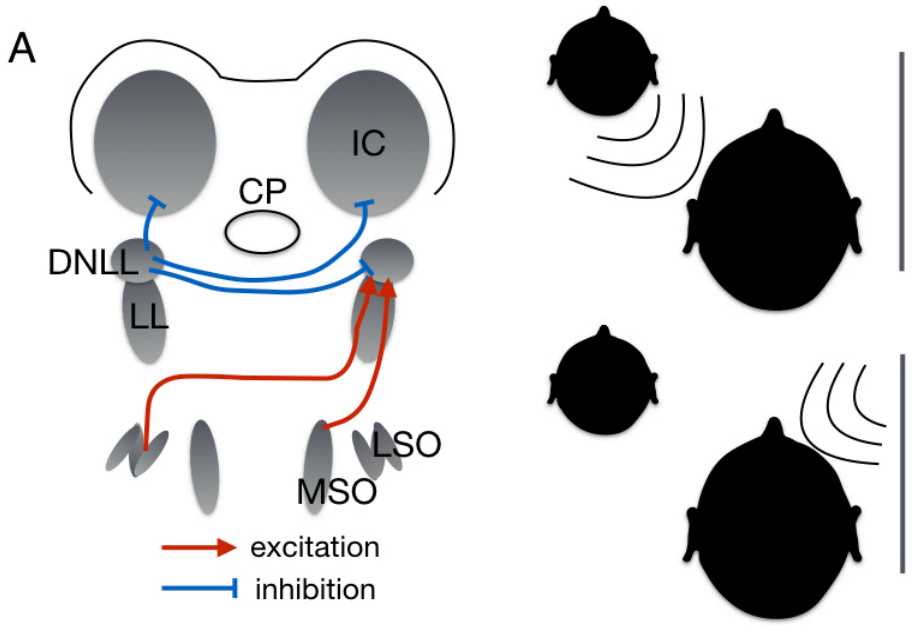

Figure 4: DNLL circuit and persistent inhibition. A: Input pattern on the DNLL and projections from the DNLL to the Inferior colliculus (IC). Excitatory projections from ipsilateral MSO and contralateral LSO target the DNLL. Reciprocal inhibitory connection via the commissure of Probst (CP) connects the two DNLL nuclei and causes persistent inhibition. B: Sound from a sound source arriving at the left ear via the direct pathway. C: Activation of the left LSO and/or right MSO. These then activate the right DNLL that then inhibits neurons in both ICs and the left DNLL.

Thereby achieved capability to faithfully generate APs to each stimulation event is most likely critical for the synaptic mechanism by which the GABAergic output of this circuit is extended to enable stimulus outlasting inhibition (Figure 4).

The presence of electrogenic NMDAR signaling is well established *in-vitro* (Ammer et al., 2012; Fu et al., 1997; Porres et al., 2011; Wu et al., 1995) and *in-vivo* (Chen et al., 1999; Kelly et al., 2000). Their functional role *in-vivo* during auditory stimulation has not been evaluated, yet.

DNLL neurons not only integrate persistent inhibition to suppress sound information in reverberant surroundings, but also process ITD and ILD information & Grothe, 2005). Thus, the DNLL has, in addition to the slow pathway, a fast counterpart for the computation of ILD and even enhancement of ITD information (Kuwada et al., 2006; Pecka et al., 2010). This enhancement of ITD information is achieved by reducing the inter-trial response variability for low frequencies and by increasing the dynamic range in neurons with higher (> 800 Hz) best frequencies (Pecka et al., 2010; Porres et al., 2011). The latter is achieved by reducing the trough (Figure 2, C) rates of the response curve while keeping the peak response rates high (Pecka et al., 2010).

1.5 Motivation

The aim of this thesis was to get a better understanding of structure-function relationships in the auditory brainstem. Towards this aim I investigated biophysiological and synaptic properties of highly specialized neurons of auditory brainstem nuclei during development and in the mature system. The MSO is one of the fastest nuclei in the brain, which makes it an interesting structure to study biophysical specializations towards temporal precision. One of these biophysical specializations is the high resting conductance, partly based on the expression of Kv channels. For the MSO so far, only the expression of low voltage activated Kv

channels has been hypothesized. However, neurons of other brainstem nuclei as for example the MNTB have been described to express a high multitude of Kv channels. Therefore, in the first study I investigated the multitude of potassium channels expressed in the mature MSO. To achieve this, it was important to first map all channels that are being expressed along the whole neuron.

MSO neurons receive highly specialized synaptic inputs that are crucial for ITD detection. While the refinement of inhibitory inputs has been studied, that of excitatory inputs remains unclear. In the second part of the study I used calcium imaging and *in-vitro* recordings to evaluate the developmental changes in postsynaptic receptor composition and currents. Inhibitory input refinement has been shown to be experience-dependent. Therefore in the following it was tested whether the observed refinements are dependent on activity or experience. To do so, one group of animals was raised in omnidirectional noise, which masked most of the spatio-temporal information.

The DNLL is another brainstem nucleus that receives ITD and ILD information from the MSO and LSO. It is special in that it possesses two forms of inhibition, one that operates on a relatively slow time scale that enables the suppression of echolocation information. This pathway stands in contrast to the fast coincidence detector neurons in the MSO. In the next study I aimed to understand the role of synaptic NDMARs in the persistent inhibition-mediating pathway in the mature system.

2. Methods & Materials

2.1 Animals

All experiments were approved by institutional guidelines and national and regional laws. Animal protocols were reviewed and approved by the Regierung of Oberbayern according to the Deutsches Tierschutzgesetz (55.2-1-54-2532.8-148-12). Mongolian gerbils (Meriones unguiculatus) of both sexes were used for the experiments. Animals were aged to postnatal day (P) 11 - 90 to represent all stages of auditory development. They were obtained from the Institute's own breeding colony and housed in a temperature-controlled room (23° C) with a fixed 12-hour light - dark cycle. Animals had access to water and food *ad libitum* and were housed in pairs with pups for breeding purposes or otherwise in groups when grown up (> P30).

2.2 Immunohistochemistry

The overall preparation and staining procedure used in the lab has been described previously (Couchman et al., 2012; Franzen et al., 2015; Werthat et al., 2008). However, as there are some adaptations at several stages the exact procedure is described below.

2.2.1 Preparation

Animals were anesthetized with pentobarbital (20 mg/kg body weight). When the animals showed no hindleg withdrawal reflex anymore, the skin on the

thorax was lifted and a small cut in the skin covering the sternum was made. This opening was then used to cut open the thorax laterally at both sites open. The resulting piece was lifted up and fixated with forceps, exposing the heart. An injection cannula (0.3x12 mm) attached to a perfusion pump system was placed into the left ventricle. Immediately after turning on the perfusion pump the right atrium was opened with a small cut. First, Ringer/Heparin was pumped through the vessels for about 2 – 3 minutes to clean the blood system. Next, the fixative, 4 % paraformaldehyde (PFA) was pumped through the system for about 30 minutes. After the perfusion the brain was removed and post-fixed in 50 ml 4 % PFA overnight at 4° C on a shaker.

2.2.2 Staining

The same staining protocol was used for all antibodies (Table 1 & 2). After overnight incubation in 4 % PFA, brains were washed in 0.1 M phosphate buffered saline (PBS; 10 mM Na_2HPO_4, pH7.4, 2 mM KH_2PO_4, 137 mM NaCl, 2.7 mM KCl) for 5 minutes at room temperature (RT). To get slices containing the SOC or DNLL, brains were cut at an approximately 20° or 40° angle, respectively, at the caudal end of the cortex using a scalpel. Brainstem sections of 50 - 70 µm thickness were obtained using a vibratome (Leica VT 1200S, Leica Microsystems). These slices were then washed four times in 0.1 M PBS for five minutes each on RT. Subsequently sections were blocked in 1 ml blocking solution (BS, 0.3 % Triton, 1 % saponin, 0.1 % bovine serum albumin, diluted in PBS) for 1 hour on a shaker at RT to reduce nonspecific binding of antibodies. The same BS was used to dilute the primary antibodies that were diluted in 0.5 ml for each well, containing

up to three sections. Primary antibodies were incubated for 48 h on a shaker at 4° C. The sections were then washed additionally eight times in 0.1 M PBS to ensure the removal of surplus unbound antibodies. Secondary antibodies were then incubated in 0.5 ml BS per well for 3 h at RT on a shaker. Finally, slices were washed in 1 ml 0.1 M PBS for 5 minutes four times at RT and then mounted in Vectashield on slides (76 x 26 mm, Thermo Scientific, Gerhard Menzel GmbH, Braunschweig). Control peptides were stained using the exact same procedure with the supplier-specified dilutions at slices from the same brain as for the experimental antibody stain. All stainings were performed in replicates of three animals.

Antigen	Host	Type	Amino-acid residues	Dilution	Company	Cat#	2nd AB
NR1	Rabbit	Polyclonal		1:500	SantaCruz	sc-9058	Cy3
NR2A	Rabbit	Polyclonal	41-53	1:500	Alomone Labs	AGC-002	Cy3
NR2B	Rabbit	Polyclonal	323-337	1:500	Alomone Labs	AGC-003	Cy3
NR2C	Rabbit	Polyclonal	365-377	1:500	Alomone Labs	AGC-018	Cy3
NR2D	Rabbit	Polyclonal	345-359	1:500	Alomone Labs	AGC-020	Cy3
GluR2	Mouse	Polyclonal	175-430	1:100	Millipore	MAB-397	Cy3
GluR4	Rabbit	Polyclonal	179-193	1:500	Alomone Labs	AGC-005	Cy3
MAP2	Chicken	Polyclonal		1:1000	Neuromics ACRIS	CH22103	AMCA/ A488
S100ß	Rabbit	Polyclonal		1:500	swant	37	A488
SV2	Mouse	Polyclonal		1:500	DSHB	SV-a1SV2c	

Table 1: Antibody list: List of all used primary antibodies and their host, type and used secondary antibodies for the developmental study of Ca^{2+} influx sites in the MSO (see section 3.1.2). MAP2, S100β and SV2 were used for the K^+ channel expression (see section 3.1.1) and binaural processing study in the DNLL (see section 3.1.3) as well.

Antigen	Host	Type	Amino-acid residues	Dilution	Company	Cat#	2nd AB
Kv1.1	Rabbit	Polyclonal	6-24	1:200	Alomone Labs	APC-009	Cy3/A488
Kv1.1 (extr.)	Rabbit	Polyclonal	778-910	1:200	Alomone Labs	APC-161	Cy3
Kv1.1	Mouse	Polyclonal	416-495	1:100	NeuroMab	75-008	DyLight549
Kv1.2	Rabbit	Polyclonal	193-206	1:200	Alomone Labs	APC-010	Cy3
Kv1.2	Mouse	Polyclonal	458-476	1:500	NeuroMab	75-008	DyLight549
Kv1.4	Rabbit	Polyclonal	417-499	1:100	Alomone Labs	APC-007	Cy3
Kv1.6	Rabbit	Polyclonal	428-499	1:200	Alomone Labs	APC-003	Cy3
Kv2.1	Rabbit	Polyclonal	589-655	1:200	Alomone Labs	APC-012	Cy3
Kv2.2	Rabbit	Polyclonal	859-873	1:200	Alomone Labs	APC-120	Cy3
Kv3.1b	Rabbit	Polyclonal	567-585	1:200	Alomone Labs	APC-014	Cy3
Kv3.2	Rabbit	Polyclonal	184-204	1:200	Alomone Labs	APC-011	Cy3
Kv3.3	Rabbit	Polyclonal	701-718	1:200	Alomone Labs	APC-102	Cy3
Kv3.4	Rabbit	Polyclonal	177-195	1:200	Alomone Labs	APC-019	Cy3
Kv4.1	Rabbit	Polyclonal	538-550	1:200	Alomone Labs	APC-119	Cy3
Kv4.2	Rabbit	Polyclonal	454-469	1:200	Alomone Labs	APC-023	Cy3
Kv4.3	Rabbit	Polyclonal	454-469	1:200	Alomone Labs	APC-017	Cy3
Kvß2	Rabbit	Polyclonal	20-34	1:500	Alomone Labs	APC-117 A	A488

Table 2: Antibody list: List of all antibodies used and their host, type and used secondary antibodies during the K^+ channel study in the mature MSO (see section 3.1.1).

Conjugate	Host	Antigen	Dilution	Company	Cat#
Cy3	Donkey	Rabbit	1:400	Dianova	711-165-152
A488	Donkey IgG (H+L)	Rabbit	1:200	Molecular Probes	A21206
DyLight549	Goat IgG2b	Mouse	1:500	Dianova	115-505-207
AMCA	Donkey	Chicken	1:200	Dianova	703-156-155

Table 3: Antibody list: List of all used secondary antibodies and their host and type.

2.2.3 Imaging and confocal microscopy

Confocal scans were taken with a Leica TCS SPL System (Leica, Wetzlar, Germany). Single cell images were taken in stacks with a 63x objective (1.32 NA) and a z-step size of 0.63 µm leading to a voxel size of 481.47 x 481.47 × 630 nm^3. Neurons of the DNLL were scanned with a 1.5x zoom, leading to a pixel size of 321.29 × 321.29 nm^2.

The different fluorophores were excited with three lasers: an Argon laser was used to excite Alexa 488 with an excitation wavelength of 488 nm (emission filter: 494 - 555 nm), a diode-pumped solid state laser was used to excite Cy3 with 561 nm (emission filter: 565 - 606 nm) and DyLight 649 was excited with a wavelength of 633 nm (emission filter: 640 - 740 nm) using a helium - neon laser. Consecutive dual or triple wavelength line scans were Kalman-averaged 5 times. Z-chromatic shift between color channels was corrected for RGB stacks in ImageJ (National Institute of Health, USA). Montages of RGB optical sections and maximum-intensity projections were assembled into tables by using custom - written ImageJ plugins and Photoshop CS software (Adobe). Final image arrangement and scale bar creation were done using Igor Pro (Wavemetrics).

2.2.4 Analysis

To analyze Kv subunit distribution, the staining intensity in arbitrary units (a.u.) was plotted against position for the neuronal marker microtubule associated protein-2 (MAP2) and for Kvx.x. Next the two resulting intensity distributions were fitted with a Gaussian fit. From these Gaussian fits the half-widths were extracted. Next, the Kv-to-MAP2 ratios of the Gaussian fit half-widths were calculated to get a measure of the overlapping distribution profiles. This ratio should be 1 if Kv and MAP2 show the same spatial expression profile and larger if it is rather spread along the dendrites. The given n-values in the results section are the number of sections analyzed in this way per Kv channel.

2.3 *In-vitro* electrophysiology

The overall preparation and recording setup for in-vitro electrophysiology was performed similarly as described by Couchman et al., 2012 and Myoga et al., 2015 for the MSO recordings. Fiber stimulation experiments in the whole-cell configuration were carried out and analyzed similarly as described in Ammer et al., 2012; Porres et al., 2011 and Myoga et al., 2014. However, the exact procedure is described below in more detail.

2.3.1 Preparation

Animals were decapitated and brains were removed in either ice - cold (P11 - 14) or room temperature (P17 - 90) dissection solution containing (in mM) 50 -120 sucrose, 25 NaCl, 25 $NaHCO_3$, 2.5 KCl, 1.25 NaH_2PO_4, 3 $MgCl_2$, 0.1 $CaCl_2$, 25 glucose, 0.4 ascorbic acid, 3 myo-inositol and 2 Na-pyruvate (pH 7.4 when

bubbled with 95 % O_2 and 5 % CO_2). Subsequently, the brains were rough-cut according to the nucleus and age. For the MSO preparation, the brain was either cut once coronally at a roughly 30° angle at the caudal part of the cortex (P11 - P17, Figure 5, A) or first cut coronally and then horizontally, between cerebellum and spinal cord (P60 – P90, Figure 5, B).

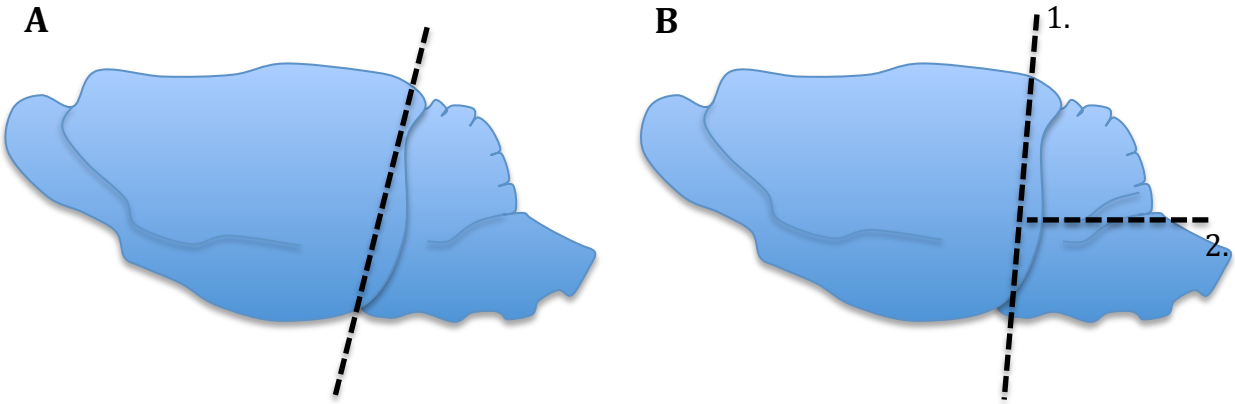

Figure 5: The two ways to prepare slices containing the MSO in young and mature gerbils. A: For MSO recordings of young gerbils (P11 - P17), the brains were cut at an angle before taking thin slices of the caudal brain part. B: The brains of mature gerbils were cut two times before slices containing the MSO were taken. First, the brain was cut at a vertical angle shortly anterior of the cerebellum (1.) and then horizontally between cerebellum and brainstem (2.).

For the MSO preparation, 200 µm thick transverse (P11 – P17) or 110 µm thick horizontal (P60 – 90) slices were made. Slices were incubated in artificial cerebral fluid solution (ACSF)-based recording solution (in mM): 125 NaCl, 25 $NaHCO_3$, 2.5 KCl, 1.25 NaH_2PO_4, 1 $MgCl_2$, 2 $CaCl_2$, 25 glucose, 0.4 ascorbic acid, 3 myo-inositol and 2 Na-pyruvate (pH 7.4 when bubbled with 95 % O_2 and 5 %) at 34.5° C for 45 min, bubbled with 5 % CO_2 and 95 % O_2. Slices were then brought to RT for the rest of the experimental day, until used.

2.3.2 Recordings

All experiments below described were performed at near physiological temperature (34 – 36° C) to mimic the natural kinetics of cellular processes. This temperature was maintained by in-line (SF-28) and bath chamber (PH-1) heaters (Warner Instruments, Biomedical Instruments) and monitored with a temperature probe placed directly next to the slice. For recordings, slices were kept in a recording chamber attached to a microscope (BXW51WI, Olympus) equipped with Dodt gradient contrast illumination (Luigs and Neumann) and continuously perfused with recording solution. Recordings were made using a computer-controlled EPC 20 USB double-clamp amplifier (HEKA, Lambrecht/Pfalz, Germany), and data was acquired with the accompanying PatchMaster (HEKA, Lambrecht/Pfalz, Germany) software.

All recordings were performed using filamented, fire-polished borosilicate glass electrodes (inner diameter: 0.86 mm; outer diameter: 1.50 mm, Harvard Apparatus Ltd., Edenbridge, Kent, UK), pulled to a resistance to the bath of 2.8 – 3.5 MΩ using a horizontal multi-step puller (DMZ-Universal Puller, Zeitz Instruments, Martinsried, Germany) and were heat-polished to ensure a smooth tip.

Electrodes were attached to an electrode-holder connected to a manometer to monitor orally-generated pipette pressure. X-y-z translation of the electrode headstage was performed with a PatchStar Micromanipulator (Scientifica Ltd., Uckfield, East Sussex, UK). The electrodes connecting the headstage with the pipette solution as well as the ground electrode were made of Ag/AgCl wire.

2.3.3 Calcium imaging

Cells were visualized with a CCD camera (QImaging Retiga™ 2000DC) connected to a second PC. On this second computer the software live acquisition (TILL Photonics GmbH, Gräfelfing, Germany) was running for real-time microscopy and fast acquisition of image series. This camera had a chip size of 1600 x 1200 pixels with one pixel having the size 7.4 x 7.4 μm^2 with a 20x objective.

2.3.4 Voltage clamp experiments

For all voltage clamp experiments (fiber stimulation, minimal stimulation and rectification experiments in the MSO) the internal solution (IC) contained (in mM): 135 Cs-Gluconate, 10 Hepes, 20 TEA-Cl, 3.3 MgCl, 2 Na_2ATP, 0.3 NaGTP, 3 $Na_2Phospho$, ZD 7288 with a pH of 7.24 and ~300 mOsm plus 30 µM Oregon Green BAPTA-1 (OGB-1, Molecular Probes). Visually identified MSO neurons were patched with an IC filled patch pipette (2.5 - 3.5 MΩ) and the access resistance was compensated to a constant residual of 2 - 3 MΩ. All data was acquired at 50 kHz and filtered at 3 kHz. Synaptic currents were evoked by local stimulation of available afferent fibers with a glass electrode (4 - 5 MΩ) filled with recording solution. To find fibers, a biphasic test pulse (0.2 ms) of about 20 V was used to identify afferent fibers of the patched cell.

Stimulation pulses were voltage pulses generated by the EPC10/2 amplifier (HEKA Elektronik) and postamplified 10 times by a linear stimulus isolator (A395; World Precision Instruments). Cells were recorded and included into the analysis when their input resistance was lower than 12 MΩ and their leak current was stable and less than 300 pA for MSO experiments.

2.3.4.1 Fiber stimulation (with calcium imaging)

To estimate the synaptically evoked calcium influx, Calcium imaging was performed simultaneously with fiber stimulation. To optimally activate NMDARs, the recording solution was modified to contain 0 mM $MgCl_2$. To block inhibitory synaptic currents, 10 µM SR and 0.5 µM strychnine was also included. The IC contained the high-affinity, nonratiometric Ca^{2+} indicator OGB-1 (30 µM) with a dissociation constant (K_d) of 195 ± 5 nM to visualize calcium influx. For these experiments the visibility of a long stretch of dendrite was an additional criterion to the electrophysiological criteria mentioned above. After an afferent fiber was found, the dendrite was then positioned in a way that it optimally spanned the imaging area. Pixel binning was set to 4 x 4, and the imaging area was cut optically within the imaging software in its extensions to 70, leading to a pixel size of 29.6 x 29.6 µm. Ninety images with an exposure time of 20 ms and a cycle time of 30 ms at a wavelength of 488 nm were taken to obtain baseline values. Then, the stimulation protocol was started. This protocol took 10 baseline images (200 ms), and then triggered the fiber stimulation. Another 80 images (1600 ms) were taken after the trigger to record the fiber-evoked signal (Figure 6, A). The following four different stimulations were used to evoke synaptic responses: a single pulse, 3 pulses at a 100 Hz, 10 pulses at a 100 Hz and 25 pulses and a 100 Hz pulse. Recovery of the signal was recorded for 550 ms for all stimuli. The procedure was always started with the single pulse and then the others in ascending order and back with an inter-trial time of about 10 s to ensure recovery to baseline. Each of these stimuli was presented three times. Finally, NMDAR

responses were isolated by blocking AMPARs with DNQX (20 µM). After 5 – 12 minutes of wash-in, each stimulus was presented additionally three times.

2.3.4.2 Minimal stimulation

During minimal fiber stimulation experiments the recording solution contained 10 µM SR and 0.5 µM strychnine and had Mg^{2+} and Ca^{2+} concentrations of 1 and 1.5 mM, respectively. As described above the search for an afferent fiber onto the cell was conducted using a test pulse. To estimate single fiber size, the afferent fiber was then stimulated with a double pulse with an inter-stimulus interval of 20 ms and a sweep interval of 5 s (Figure 6, B). The stimulation was preceded by a voltage step down to -70 mV for 10 ms. After 30 ms the 0.2 ms long stimulus was applied. The stimulus voltage was then reduced until no synaptic current was elicited anymore. Subsequently the stimulation was increased in steps of 0.5 V until a single fiber current was elicited. When the EPSC size and timing showed a low variability, it was rated as a single input. Next, the stimulation intensity was further increased in steps until the EPSC was elicited in 100 % of the times and then further until a second step in EPSC size became apparent. The experiment ended with a maximum stimulation intensity of about 35 V to be able to evaluate the maximum fiber size.

2.3.4.3 Spontaneous activity

Spontaneous miniature events were recorded with same IC and recording solution as during minimal stimulation experiments. Here, the size and frequency of excitatory spontaneous miniature events were estimated by recording resting

membrane potential without applying any voltage and only recording baseline fluctuations in membrane potential.

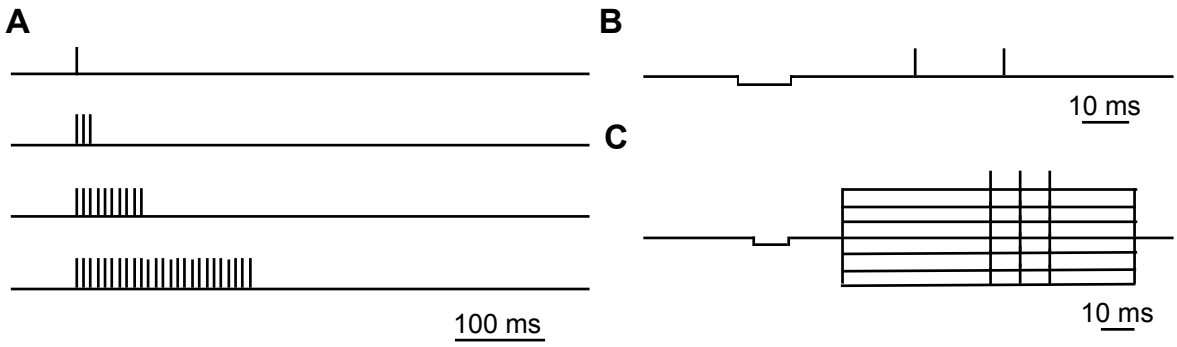

Figure 6: Stimuli used for voltage clamp experiments in the MSO. A: Four pulses used to evaluate calcium influx during synaptic stimulation mediated by present AMPARs and NMDARs. From top to bottom: single pulse, 3, 10 and 25 pulses at 100 Hz. B: Double pulse used for evaluate single fiber size. Short hyperpolarization step followed by two pulses to evoke synaptic currents C: Protocol to determine rectification of evoked currents. Also short hyperpolarization step followed by three pulses at different membrane potentials. Injected currents were varied in alternating steps from – 70 mV to 70 mV.

2.3.4.4 Rectification

During recordings of the rectification of AMPAR currents, the IC contained spermine (20 µM) to prevent the washout of endogenous intracellular polyamines (Bowie et al., 1995, Kamboj et al., 1995, Koh et al., 1995). The ACSF for recordings contained 10 µM SR-95531 and 0.5 µM strychnine to block inhibitory currents and had a $CaCl_2$ concentration of 1.5 mM and $MgCl_2$ concentration of 1 mM. The protocol used to determine the rectification varied the membrane potential from -70 to 70 mV in alternating steps of 30 mV (Figure 6, C).

2.3.5 Analysis

All *in-vitro* recordings were analyzed using custom written procedures in IgorPro (Wavemetrics). Images from calcium imaging were analyzed in ImageJ with Fiji

extensions and MatLab (Mathworks). Datasets showed normal distribution as exemplified in Figure 7 for some datasets using the normal distribution formula:

$$\frac{1}{\sigma\sqrt{2\pi}} \cdot e^{-\frac{1}{2}\left(\frac{x-\mu}{\sigma}\right)2}$$

In general normal distribution was tested by using the Anderson-Darling test with the Nullhypothesis that the data shows normal distribution otherwise the p-value is smaller than 0.05. Consequently, the normal distributed data for calcium imaging and fiber stimulation results were tested for significance using an unpaired t-test.

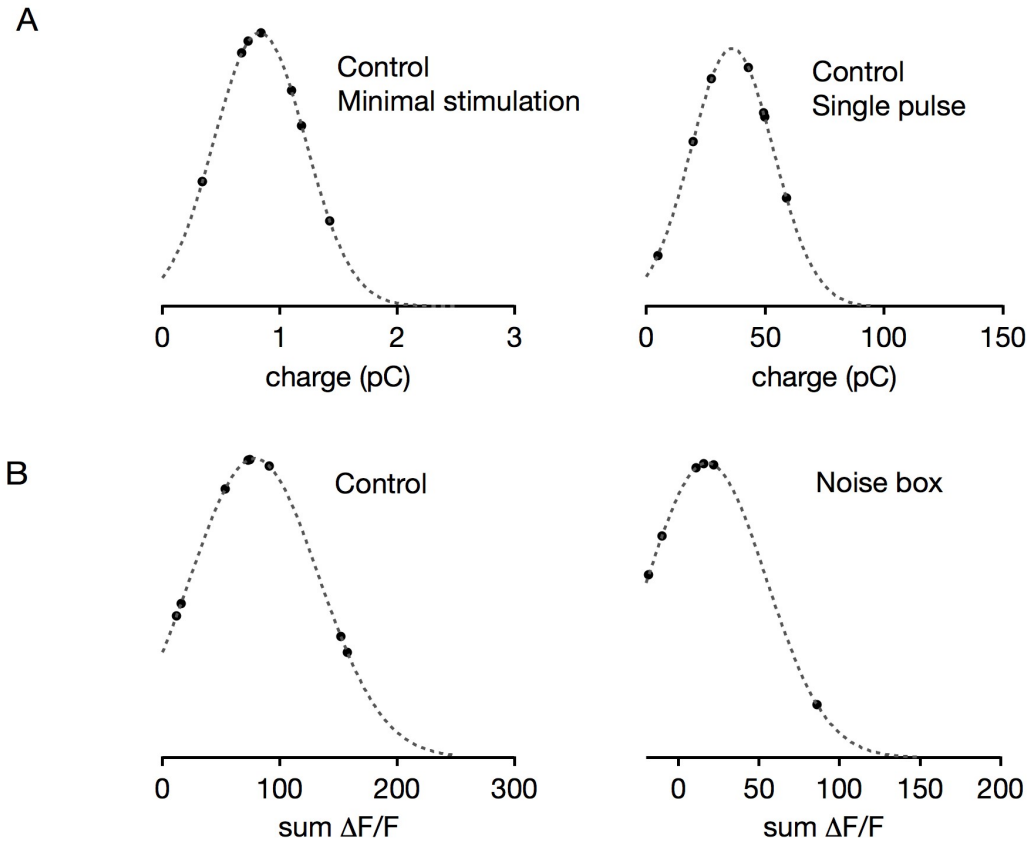

Figure 7: Normal distribution exemplified for some datasets. A: Calculated normal distribution for P11 in control condition for minimal fiber stimulation (first graph) and single pulse stimulation (second graph). B: Normal distribution graph for P14 calcium imaging in control (first graph) and noise box condition (second graph).

The t-test had to be unpaired as the two groups (control and noise box) were independent of each other. To additionally verify the usage of the t-test I also performed the Mann-Whitney-U-test that is used for non-parametric datasets. Both tests gave different p-values but all significant results were significant in both tests, the same was true for non-significant results (e.g. sum ΔF/F at P14: single pulse: unpaired t-test: p = 0.018; Mann-Whitney-U-test: p = 0.042; 3 pulses at 100 Hz: unpaired t-test: single pulse: p = 0.001; Mann-Whitney-U-test: p = 0.012; 10 pulses at 100 Hz and sum ΔF/F at P17).

2.3.5.1 Fiber stimulation

All shown values are means over three repetitions per cell for every stimulus. The evoked charge was calculated by integrating the current from EPSC onset to the end of the recording over time. The NMDAR evoked charge transfer was taken directly from the DNQX conditions. The AMPAR contribution was calculated by subtracting the NMDAR charge from the charge transfer under control conditions. Peak currents were analyzed by determining the maximum peak value in baseline (for AMPAR peak) and in DNQX recordings (for NMDAR peak). This method was chosen to ensure an adequate differentiation of AMPAR and NMDAR evoked peak currents. It is likely that the NMDAR peak is underestimated as DNQX also partially blocks NMDAR currents, but this is the case for all ages in the same way.

The evoked calcium signals were analyzed using a custom written Fiji plugin. For this analysis the dendrite was traced with a segmented line in the first image, and this line was then aligned for all images. All images were checked

again for dendrite drift and, if necessary, adjusted. Next, the images were sorted for pulse number (single, 3 at a 100 Hz, 10 at a 100 Hz and 25 at a 100 Hz) and condition (i.e. Baseline, DNQX). The created file was then imported into Matlab and in the first step ΔF/F was calculated. To get a better EPSC charge per calcium influx relationship, the ΔF/F integral was calculated. This basically means that all ΔF/F values were summed up over the length of the dendrite and duration of the response (300 ms). AMPAR and NMDAR contribution was calculated as for electrophysiological data by subtracting the DNQX signal from the baseline signal. The time constant of AMPAR currents was determined by fitting the charge curve for each cell for the single pulse stimulation.

To estimate the rough size of the calcium influx side the pixel length of the activation side was estimated by counting all connected pixels that had the respective maximum ΔF/F peak values. In this same way, the number of hotspots present was evaluated.

2.3.5.2 Minimal stimulation

The charge and peak response for a single input was calculated from the first evoked EPSC. If both pulses evoked this input, the first was analyzed to prevent contamination from synaptic depression. All values were averaged over five traces.

2.3.5.3 Spontaneous activity

Spontaneous miniature synaptic currents were scored and analyzed using custom-written IgorPro (Wavemetrics) plugins. Here, the first step was to manually

fit at least five mEPSCs: the resulting information was used to form a mEPSC template. The next plugin used this template as a kernel to differentiate between mEPSCs and noise. Everything larger than a manually set threshold that matched the time-course of the template was counted as a mEPSC. To ensure the correct categorization afterwards, every mEPSC was scored individually by eye and either kept or rejected as noise. For all cells between at least 500 and 700 mEPSCs were scored. These scored mEPSCs were then analyzed for average peak current, time course and amplitude distribution. The average peak current was used to calculate the quantal content of a fiber. This was estimated by dividing the peak of a single fiber by the average peak of a mEPSC. The time course was compared between mEPSCs and single input to exclude the possibility of asynchronous release or synaptic spillover. In this case, the quantal content estimation would not be adequate. The amplitude distribution should follow a Gaussian distribution that supports the correct score of mEPSCs. This was verified for all analyzed cells.

2.3.5.4 Rectification

To analyze the rectification of currents, the peak current was always determined for all voltage steps and averaged over five trials, respectively. These peak values were then plotted and the first four were fitted with a line for all eight voltage steps. No rectification would mean that all peak values would lie on this line. Then the rectification index was calculated by dividing the actually measured peak current by the equivalent fit value. Data was normalized to the first peak

response value. The rectification index was calculated by dividing the last (50 mV) voltage step response by the calculated fit.

2.4 Noise box

Werthat et al. (2008) and Siveke et al. (2012) describe the general setup and functioning of the noise box. The gerbils were exposed to white noise between P8/9 until the day of recording in a cage that was placed in a 100 x 80 x 80 cm^3 sound-attenuated box in a quiet room. The white noise was introduced via 12 sets of speakers (2 high- and 2 low-frequency speakers on each of the six sides) and generated from two analogue amplifiers (Brüel and Kjær). Thus, noise from two different sources was presented from each direction. The amplitude of the noise was about 75 dB SPL (RMS-value, averaging time 30 s) and never exceeded 85 dB SPL. This noise level was chosen to mask most spatial acoustic cues without damaging the cochlea or the primary auditory centers (Withington-Wray, 1990). When the animals were placed into the noise chamber, first the noise was increased in slow steps over up to 4 h to keep the stress level low for the mother and pups. The general condition of the animals was checked on a daily basis. In the litters used for recordings, no signs of abnormal behavior could be detected during the time of noise exposure. Additionally, weight and head diameter were checked prior to recordings. Food and water were provided *ad libitum*.

My colleague Delwen Franzen performed the placement of animals into the cage and supervision of the animals during noise exposure.

2.5 Electrophysiology *in-vivo*

Surgical, electrophysiological, and stimulation procedures have been described previously (Siveke et al., 2006, 2010). Stange et al., 2013 described the drug application *in-vivo* using multi-barreled electrodes. However, the exact procedure is described below in more detail.

2.5.1 Preparation

The animals were initially anesthetized using ketamine (20 %) and xylazine (2 %) diluted in 0.9 % NaCl solution with an intraperitoneal injection (0.5 ml/100 g body weight). Consequently, the head was shaved and the animal was placed on a heating mat (Harvard Homeothermic Blanket Control Unit Model #50-7129, Harvard Apparatus Inc.) to prevent hypothermia. To ensure the correct placement of the headphones the tragus of both ears were cut. Then the head was fixated with a bite bar, to keep the head stable during the preparation. Once stabilized, the skin of the head was numbed using Lidocaine (Xylocain Pumpspray dental, AstraZeneca GmbH), and cut open along the rostro-caudal axis starting from shortly behind the nose to the beginning of the neck musculature. Next, the cut-open skin and connective tissue were pushed aside laterally to expose the pericranium-covered bone. The pericranium was removed using a 0.5 mm spatula and fatty residues cleaned off of the parietal bone with Etch 35 Gel iBond (Heraeus Kulzer GmbH). The resulting surface was coated with three layers of a primer (iBond Total Etch, Heraeus Kulzer GmbH). Afterwards an UV-sensitive dental-restorative material (Charisma A3, Heraeus Kulzer GmbH) was used to

build a mounting block for rod-shaped head bar made from brass (ca. 1.5 cm length and 2 mm ∅).

After this initial preparation the animal was placed into a custom-made floating, sound attenuated, and electrically shielded recording chamber (TMC 63-504, Technical Manufacturing Corp.). During the following finalizing preparation and recording (lasting 8 to 12 h), animals were injected continuously with anesthetics (same as initial anesthesia) via an automatic pump (801 Syringe Pump; Univentor) at a flow rate of 1.7 – 2.4 µl/min, depending on body weight. The animals' blood oxygen saturation was improved by constant carbogen (95 % oxygen, 5 % carbon dioxide) supply via a custom made inhalation mask. Body temperature was kept at 37.5° C using a heating blanket and monitored by a rectal thermometer. Next, the animal was fixed with a stereotactical device in the setup (Schuller et al., 1986) by the head bar. Syringes were put through the left hindleg, right foreleg and the nose to monitor the heart rate during recordings via an oscilloscope. The animal's head was aligned according to landmarks on the skull's surface (Loskota et al., 1974). A small craniotomy for the reference electrode was drilled latero-caudal to bregma. A larger (roughly 5 mm x 10 mm) craniotomy for the recording electrode was drilled lateral to lambda and the dura was removed (Figure 8). Ringer solution was periodically applied to the exposed brain surface to prevent damage due to dehydration. The final step in the preparation was to place the headphones in the ears. The correct placement of the headphones was tested by measuring back-reflections with small microphones mounted inside the headphone apparatus and analyzed using a custom written Matlab program.

2.5.2 Recordings

All in-vivo recordings were performed with pulled borosilicate glass micropipettes (1.5 mm O.D. x 0.86 mm I.D., GC150F-10, Harvard Apparatus Ltd.) filled with 1 M horseradish peroxidase (HRP) in 1 M NaCl and had tip resistances of 7 – 10 MΩ. Electrodes were mounted on a piezo drive (Inchworm controller 8200, Burleigh Products Group Inc., USA) and controlled via a motorized manipulator (Digimatic series 164 type 161, Mitutoyo Inc.).

The manipulator was positioned to drive the electrode at a 5 or 10 ° angle vertically tilted to the contralateral side of to the skull. The DNLL was searched in a field from a surface entry point of 600 – 800 µm caudal, 1800 – 2000 µm lateral (for 5°) and 1400 – 1600 µm (for 10°) from lambda. From the brain surface, the DNLL was typically located between 4200 and 4800 µm beneath.

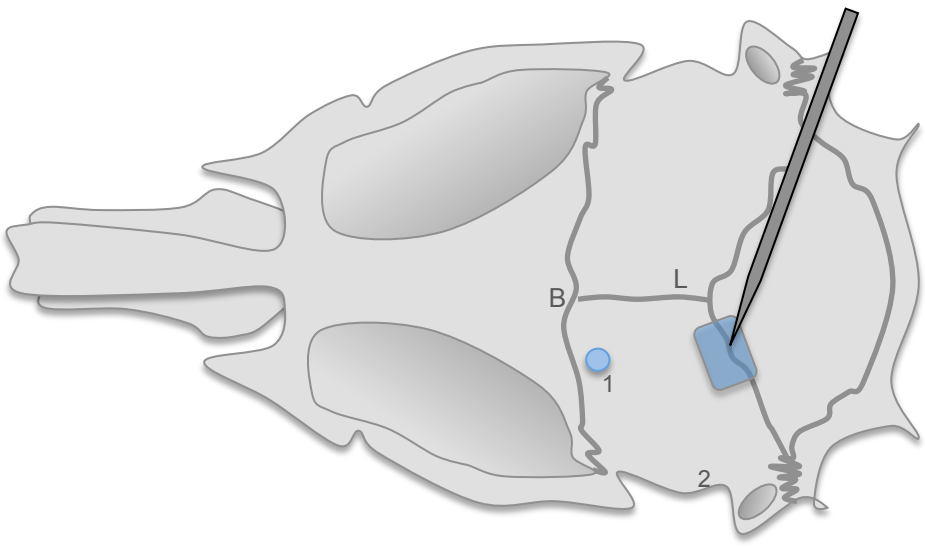

Figure 8: The position of reference and recording electrode during *in-vivo* recordings. Bregma (B) and lambda (L) were used as orientation points. For the reference electrode only a small hole was drilled (1). The hole for the recording electrode above the DNLL (2).

For recordings, the electrode signal was amplified (Electro 705, World Precision Instruments Inc.; Wide Band Amplifier TOE, 7607, Toellner GmbH) and fed to a computer via an A/D-converter (RP2.1 Tucker Davis, System 3, TDT Inc.). The incoming signal was notch filtered at 50 Hz, high-pass filtered at 300 Hz and low-pass filtered at 5 kHz bandpass filters. On the computer the Brainware software (Jan Schnupp, University of Oxford UK, for TDT) was used for online visualization and analysis of recorded spike trains. Spikes were isolated from noise by online thresholding. The resulting spike times and raw traces were recorded and saved for later analysis.

At the end of an experimental day the recording site was marked by iontophoretic application of HRP. Then the animals were euthanized by injecting 20 mg/kg body weight pentobarbital. Immediately after the injection the animals were perfused and the brains cut as described above in the section Immunohistochemistry Preparation (2.2.1). The sections were then dianimobenzidine (DAB) stained against HRP and Nissl stained to visualize labeled cell bodies. These stainings were performed using standard protocols established in the lab by a technical assistant. These stained sections were used to verify the recording site via light microscopy on an Olympus dotSlide microscope (Olympus BX61VS).

2.5.3 Pharmacology

NMDARs were blocked during recordings using D-(-)-2-Amino-5-phosphonopentanoic acid (D-AP5; 50 mM; pH = 7.4, BioTrend). This drug was applied iontophoretically using custom-made multi-barreled electrodes. The center

barrel was filled with 1 M NaCl to balance the current. Three of the other barrels were filled with drugs, and one filled with ringer solution had the same pH (7.4) as the used D-AP5 solution. Retention (+20 nA) and ejection currents (-70 pA) were applied via a Neurophore BH-2 (Harvard/Medical Systems). The drug effect on the neuronal response was recorded during, and immediately after, applying the ejection current and during the following recovery.

2.5.4 Stimulus

During *in-vivo* recordings all acoustic stimuli were digitally generated with Brainware software (Jan Schnupp) at a sampling rate of 50 or 200 kHz and converted to analogue signals. They were attenuated to the desired levels (PA5, Tucker Davis Technologies) and delivered to earphones for low frequencies (ER-2, Etymotic Research; calibrated for 100 to 15,000 Hz) or to custom-made electrostatic speakers for high frequencies (calibrated from 15 kHz to 100 kHz).

Figure 9: Acoustic stimuli used during *in-vivo* recordings. A: Stimulus to evoke persistent inhibition in neurons of the DNLL. 50 ms of spontaneous activity was followed by 200 ms pure tone at BF on the contralateral side. After 50 ms on the ipsilateral side the same tone started and lasted for 50 ms.

For each isolated unit, its best frequency, meaning the frequency at which spikes were elicited at the lowest intensity, was determined using a protocol testing all frequencies and intensities. Thus, monaural pure tones at varying

frequencies around the approximated best frequency were presented randomly at varying sound intensities. In the next protocols, its sound threshold, which is the lowest sound intensity that elicits spikes was determined using monaural and binaural pure tones. Sound threshold was determined by presenting monaural pure tones at the earlier determined best frequency (200 ms tone including 5 ms cosine rise/fall times) with randomly distributed sound intensities (5 dB steps in a range of 20 dB to 50 dB) using a repetition rate of 2 Hz. For some neurons the sensitivity to ITDs and ILDs was tested by presenting binaural correlated noise (level 20 dB above threshold) with different ILDs and ITDs (minimal range: ± 0.5/best frequency, minimal steps: 9 ITDs).

To evoke persistent inhibition, a contralateral pure tone at best frequency (200 ms tone including 5 ms cosine rise/fall times) was presented 20 dB above threshold (Figure 9). Additionally, a short louder ipsilateral pure tone (50 ms at best frequency, 40 dB above threshold) was presented starting at 50 ms after the contralateral tone. While leaving the interaural intensity difference constant, persistent inhibition was measured at five different overall sound levels (5 to 25 dB above threshold contralaterally and 25 to 45 above threshold ipsilaterally).

2.5.5 Analysis

Spikes were initially sorted on-line with Brainware. Next, offline analysis of the data was performed using self-written functions in Matlab. To determine the length of persistent inhibition, first the baseline activity during the first 50 ms was calculated. Next, the length of inhibition was defined as the time between ipsi onset and the first spike. This gave the total time of inhibition, and then the length

of ipsi stimulation was subtracted to get the length of persistent inhibition. This persistent inhibition length was averaged over 50 trials per stimulation. These differences in lengths were calculated before and after drug application as well as for different levels of stimulation. The cumulative spike number was plotted to see where and how changes occur. Towards this aim, all spikes were summed up over time. Consequently, periods of inhibition are visualized as plateaus and the slope of the curve would give information about how fast the recovery after the inhibition is.

Statistics were performed after normal distribution of the data was verified using the Anderson-Darling test with p-values bigger than 0.05 verifying normal distribution. Data showed normal distribution and were thus tested for significance using the paired t-test. In this case it had to be the paired t-test as different data of the same neuron is compared.

3. Results

3.1 Potassium channels in the MSO

The contributions to this project were the following: the idea for the project came from my supervisor Prof. Dr. Felix Felmy. I managed project organization, realization and literature research for further steps. These points were discussed on a regular basis with my supervisor. I supervised the master student, which included the preparation of procedure sheets for perfusion, antibody protocols, imaging and analysis. I taught her all the methods needed for this project and prepared a weekly plan for the first 6 weeks. For the results shown here, I supervised all of the taken steps including the imaging and image procession. Subsequent image analysis with semi-quantitative analysis was the idea of my supervisor and performed by Alisha Nabel under the supervision of Prof. Dr. Felix Felmy. I was present during meetings and took part in discussions on data. Alisha Nabel, under the supervision of Prof. Dr. Felix Felmy, assembled the final graph showing the channel distribution (Figure 15).

Neurons in the MSO are one of the most temporally precise neurons in the brain (Grothe et al., 2010). This temporal precision is achieved by cellular adaptations that allow the system to encode differences in arrival times on microsecond time scales. One of these adaptations is the developmentally reduced input resistance leading to faster membrane time constants (Scott et al., 2005). This low input resistance is, among others, achieved by the presence of Kv channels (Mathews et al., 2010; Scott et al., 2005). However, so far mostly the

presence of LVA channels has been described (Mathews et al., 2010; Scott et al., 2005).

The expression of the Kv1.1 channel has been hypothesized to be biased towards the somata and proximal dendrites of mature MSO neurons (Mathews et al., 2010; Scott et al., 2005). However, as has been shown for the MNTB, it is likely that the MSO expresses a multitude of Kv channels. The simulated large dendritic EPSPs would be especially suited to interact with HVA channels (Mathews et al., 2010). Besides LVA and HVA channels, A-type channel expression was investigated. Immunohistochemical stainings were scanned for the MSO. All used antibodies were co-immunostained with at least MAP2 to identify their expression profile on the postsynaptic neuron. Potassium channels in conjunction with MAP2, with MAP2 as reference, were used for semi-quantitative analysis.

3.1.1 Low-voltage activated potassium channels

Kv1.1 expression has already been proposed to be biased towards soma and proximal dendrites as here LVA currents are highest (Mathews et al., 2010; Scott et al., 2005). Consistently, we found Kv1.1 expression biased to soma and proximal dendrites (Figure 10, A; Mathews et al., 2010; Scott et al., 2005). For additional verification of the antibody specificity a control peptide staining in parallel to the Kv channel was performed at all times. This was processed, imaged and analyzed exactly the same way as the actual antibody. For the Kv1.1 antibody the control peptide further supported our findings (Figure 10, A). Thus, the

calculated MAP2-to-Kv1.1 ratio of 0.92 ± 0.07 (n = 14) for Kv1.1 supports an expression biased to the soma and proximal dendrites.

After having verified the protocols and tested the analysis, the expression of another LVA, Kv1.2 was investigated. Its expression was more spread into the dendrites than that of Kv1.1 (Figure 10, A & B). However, in addition to the neuronal labeling also structures surrounding the cells expressed Kv1.2 (Figure 10, B). Thus, the differentiation between pre- and postsynaptic labeling based on MAP2 was beyond this analytical approach. The control peptide staining revealed a slightly unspecific binding rate and consequently higher background staining (Figure 10, B) than for Kv1.1. Still, when comparing the Kv1.2 staining with the peptide staining, which is possible as they were scanned with the same laser settings, it was shown that Kv1.2 neuronal labeling is higher than the unspecific binding (Figure 10, B). This gave a Kv1.2 to MAP2 ratio of 1.37 ± 0.12 (n = 5) indicating a more dendritic expression pattern compared to Kv1.1 (Figure 10, B). However, as it was impossible to differentiate between pre- and postsynaptic labeling, it will be necessary to do further experiments. Kv1.6 was expressed at the soma and proximal dendrites (Figure 10, C). The control peptide staining showed the high specificity of the used antibody (Figure 10, C). Further analysis using a Gaussian fit showed that the expression of Kv1.6 was biased towards the soma and proximal dendrites. This was further confirmed by the ratio of MAP2 to Kv1.6 of 1.01 ± 0.03 (n = 8).

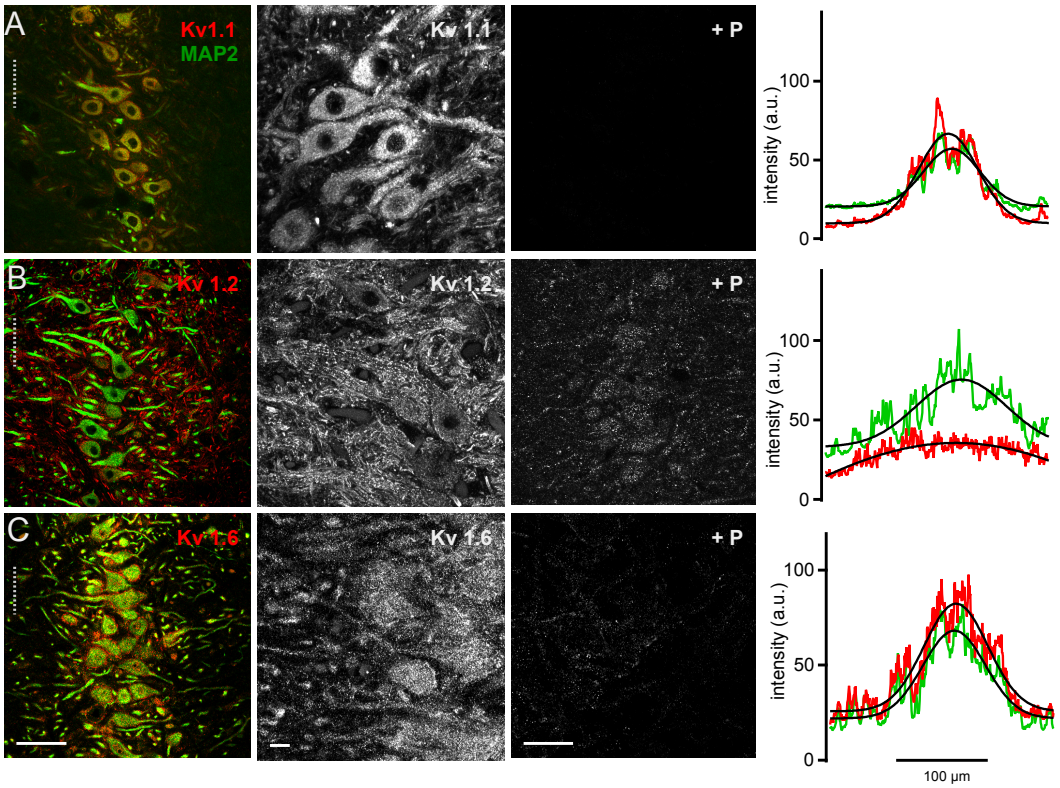

Figure 10: The expression of LVA channels in the mature MSO. The dotted lines in the first row always mark the area for the analysis. Scale bars are 50 µm for overview images and 10 µm for zoomed in grey scale. First row is always the overlay of Kv channel (red) and MAP2 (green). Second row is the zoomed in image in the Kv channel only. Third row shows the control peptide staining that was imaged with the same settings as the Kv channel image. Last row shows the result for the semi-quantitaive distribution analysis for Kv channel (red) and MAP2 (green). A: Kv1.1 expression is biased towards soma and proximal dendrites. The used antibody shows a high specificity. The semi-quantitative analysis supports the similar expression of MAP2 and Kv channel. B: The expression of Kv1.2 spreads further into the dendrites and is also present in neuron surrounding structures. This could be further supported by the peptide staining and Gaussian fits. C: Kv1.6 is expressed on MSO neurons. It was expressed on the soma and proximal dendrites. The peptide staining indicates a high specificity of the shown staining.

Taken together, the LVA channels Kv1.1, Kv1.2 and 1.6 were all found to be expressed on neurons of the mature MSO. All of these three have similar channel kinetics but show different expression profiles (for review see Gutman et al., 2005). This suggests a functional implication of Kv1.1 and Kv1.6, specifically at the soma and proximal dendrites.

3.1.2 High-voltage activated potassium channels

In MSO neurons, simulated EPSPs at the distal dendrites are large, which allows for the integration of EPSPs with HVA channels (Mathews et al., 2010). Indeed, the HVA channel Kv2.1 showed its highest expression on distal dendrites, but also on the proximal dendrites and the somata of MSO neurons (Figure 11, A). The low unspecific binding of the control peptide supported that the interpreted signal indeed represented Kv2.1 expression (Figure 11, A). Additional control stainings with lower antibody concentrations were performed in the cerebellum and motorcortex (Figure 11, D & E). Kv2.1 is supposed to be expressed in the motorcortex (Muennich et al., 2004) and in the cerebellum (Jiao et al., 2007) as it was the case (Figure 11, D & E). Consequently, the intensity profiles were plotted to quantify whether the expression is indeed distal dendrite biased. The Gaussian fit revealed a much broader Kv2.1 expression than MAP2 (Figure 11, A). Kv2.1 to MAP2 ratio was 1.46 ± 0.15 (n = 6), which supports the distal dendrite biased expression.

In addition, Kv2.2, another HVA channel, was also expressed at the whole MSO neuron (Kv2.2 to MAP2 ratio: 1.48 ± 0.20, n = 7; Figure 11, A). Here, the control peptide staining supported the specificity of the used antibody (Figure 11, B). The semi-quantitative analysis showed that Kv2.2 expression is similar to that of Kv2.1.

In summary, in addition to LVA channels, HVA channels are also expressed on neurons of the mature MSO. The HVA channels show an expression complementary to that of the investigated LVA channels. However, both Kv2.1 and 2.2 have slow channel kinetics (for review see Gutman et al., 2005).

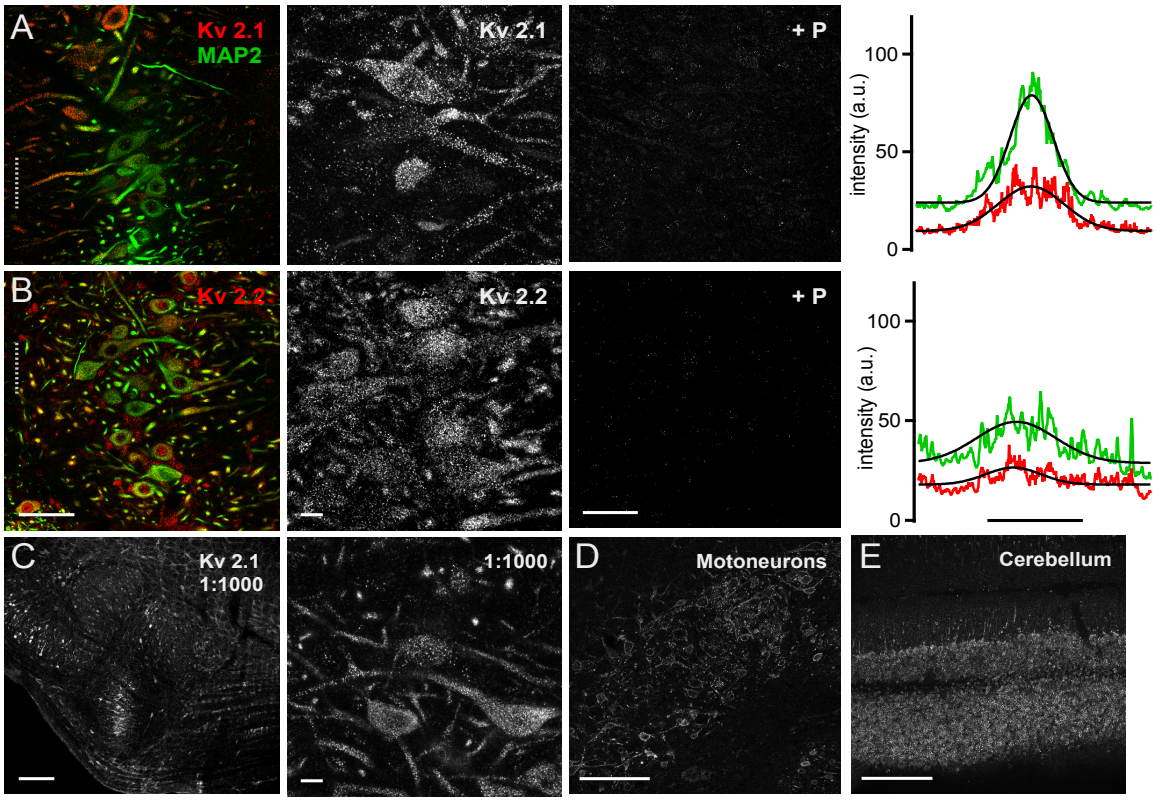

Figure 11: Kv2.1 and Kv2.2 were expressed biased to the soma and proximal dendrites. A: Kv2.1 is expressed mainly at the soma and proximal dendrites. The control peptide supports the specificity of the used antibody. This expression profile could also be shown by the Gaussian fits of Kv2.1 and MAP2. B: Kv2.2 shows a similar expression profile as Kv2.1. In contrast to Kv2.1, Kv2.2 shows nuclear labeling. The control peptide staining shows almost no signal. Comparing the MAP2 and Kv channel shows the soma and proximal dendrite biased expression. C: To further verify the described Kv2.1 expression we used a much lower antibody concentration. Still, the above described labeling is present. D & E: Additionally, we tested its expression in motorneurons and cerebellum.

There are also HVA channels with faster kinetics, for example Kv3.1b and Kv3.2 (for review see Gutman et al., 2005). To complement the study, their expression profiles were also further analyzed to see whether there is a difference in expression profiles dependent on channel kinetics. Indeed in contrast to the so far described HVA channels, Kv3.1b was expressed at soma and dendrites (Figure 12, A). However, Kv3.1b showed an additional nuclear labeling (Figure 12, A). The strong nuclear staining could hint at a low specificity of the antibody, which could be neglected with the control peptide staining (Figure 12, A). The intensity profiles of Kv3.1b and MAP2 were very much alike (Kv3.1b to MAP2 ratio of 1.25 ± 0.13;

n = 7), most likely caused by the nuclear expression. Still, it showed that the overall trend in expression was biased towards the soma and proximal dendrites.

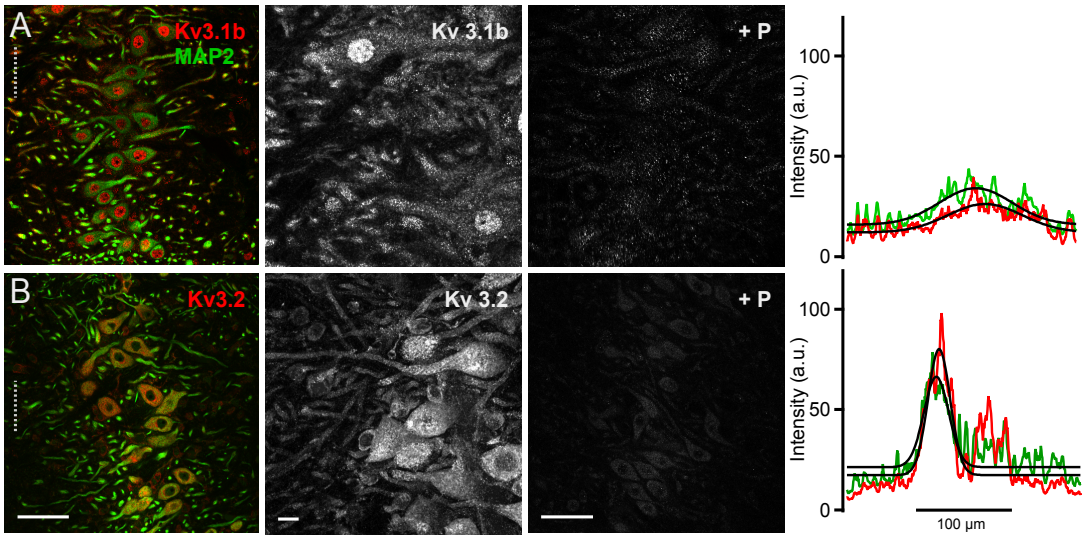

Figure 12: The HVA channels Kv3.1b and Kv3.2 that possess faster kinetics were expressed at the soma and proximal dendrites. A: Kv3.1b shows somatic and nuclear expression. Its control peptide staining has low background without a specific pattern. Kv channel and MAP2 Gaussian fits were similar, showing the soma and proximal dendrite biased expression. B: The Kv3.2 channel shows a strong soma and proximal dendrite biased expression. However, its expression spreads further into the dendrite. The Gaussian fits of Kv3.2 and MAP2 also show high similarity further proving this expression profile.

The expression profile of Kv3.2 was also biased towards soma and proximal dendrites (Figure 12, B). This result could be further corroborated by the low unspecific binding rate of the antibody (Figure 12, B). The Gaussians further supported this finding and showed that its expression is even more biased towards the soma than that of MAP2 (Kv3.2 to MAP2 ratio: 0.71 ± 0.06, n = 8).

Taken together, HVA channels possessing slow channel kinetics were expressed at the whole MSO neuron or were even biased towards the distal dendrites. These complement the observed LVA channel expression. However, there were HVA channels with faster channel kinetics that were expressed mainly

at the soma and proximal dendrites. This specific expression hints at special functions of these channels and their location.

3.1.3 A-type potassium channels

In addition to LVA and HVA channels there is a subset of channels that only open upon prior hyperpolarization. This current is called A-type current and is mediated by LVA channels also opening around resting membrane potential (for review see Gutman et al., 2005).

Kv1.4 mediates such an A-type current and was expressed strongest at the distal dendrites but also expressed at the soma (Figure 13, A). The control peptide staining additionally supports the high specificity of the used antibody (Figure 13, A). The intensity profile of Kv1.4, like the image, suggested an expression biased to the distal dendrites as its profile is shallower than that of MAP2 (Figure 13, A). This finding was further supported by the calculated ratio of 1.21 ± 0.26 (n = 6).

The Kv3.3 staining made it hard to determine its expression profile as it has a relatively high background signal (Figure 13, B). In the zoomed-in grey scale image, the somata also showed a labeling, the small dotted structures most likely were presynaptic boutons (Figure 13, B). As the staining was hard to interpret, the control peptide was of special importance because it verified the high specificity of the antibody (Figure 13, B). Thus, even the faint labeling indicates Kv3.3 expression. The intensity profiles only showed that most of Kv3.3 expression was localized at the soma and proximal dendrites (1.1 ± 0.06, n = 7; Figure 13, B).

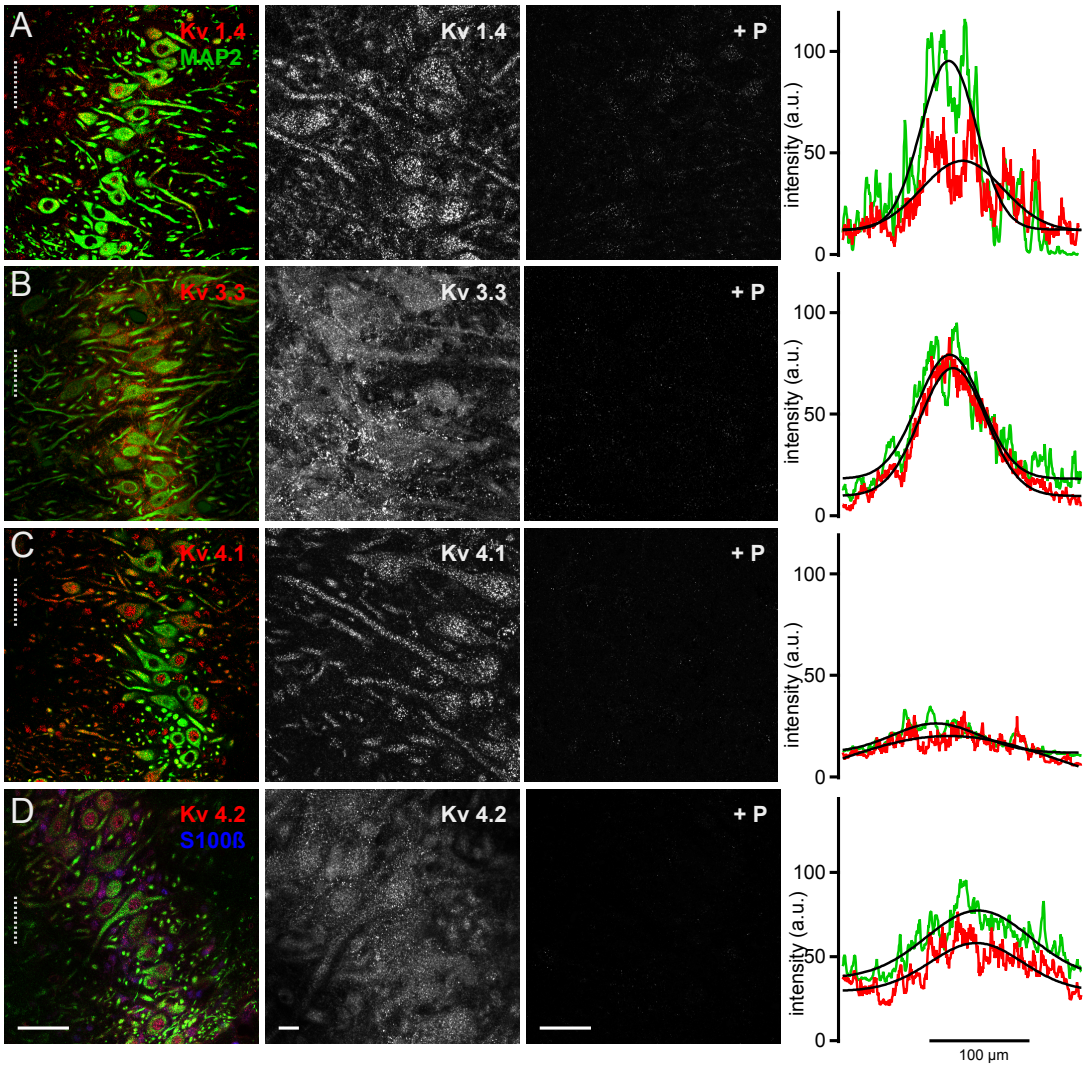

Figure 13: The expression profile of the A-type current mediating Kv channels Kv1.4, 3.3, 4.1 and 4.2. A: Kv1.4 is expressed mainly at the distal dendrites of mature MSO neurons. This could be further supported by the peptide staining and semi-quantitative analysis. B: Kv3.3 is expressed mainly in structures surrounding the soma of MSO neurons. At the soma and dendrites Kv3.3 is also expressed. The low background staining of the control peptide could show the specificity of the used antibody. Gaussian fits resemble the expression of Kv3.3 in the soma surrounding structures and thus show a soma biased expression. This underestimates its expression along the whole postsynaptic neuron. C: The expression of Kv4.1 spreads along the whole neuron and is also strong in the distal dendrites. This expression profile looks different in the Gaussian fits as the antibody shows a strong nuclear labeling. Thus, this analysis is not of special importance. D: Co-staining of Kv4.2, MAP2 and the glial marker S100β. Kv4.2 is expressed along the whole postsynaptic neuron and in glia that surround the neurons.

Expression of Kv4.1 showed high nuclear labeling that seemed to be due to specific binding as the control peptide staining showed no unspecific nuclear binding of the used antibody (Figure 13, C). The intensity profiles would imply that

Kv4.1 showed a soma and proximal dendrite biased expression (Figure 13, C). Additionally, the Kv4.1 to MAP2 ratio is 1.34 ± 0.23 (n = 4) supported this finding. However, due to the nuclear labeling this was an overestimate of somatic expression and therefore the expression seemed to be rather biased to the distal dendrites.

Kv4.2 was expressed in the MSO. However, it showed a rather diffuse expression profile including the possibility of glial labeling. (Figure 13, D). Thus, it was co-labeled with the glial marker S100β. The control peptide indicated specificity of the used antibody. This supports our findings that Kv4.2 is expressed in the soma of MSO neurons and soma surrounding glia (Kv4.2 to MAP2 ratio: 0.96 ± 0.09, n = 4).

The Kv4.3 channel was not expressed in MSO neurons but was found to be glial specific surrounding these MSO neurons (Figure 14, A). This could be further supported when one compared the glia marker with the Kv4.3 channel labeling. Here, it was stained again for the control peptide and no unspecific binding of the used antibody was observed (Figure 14, A).

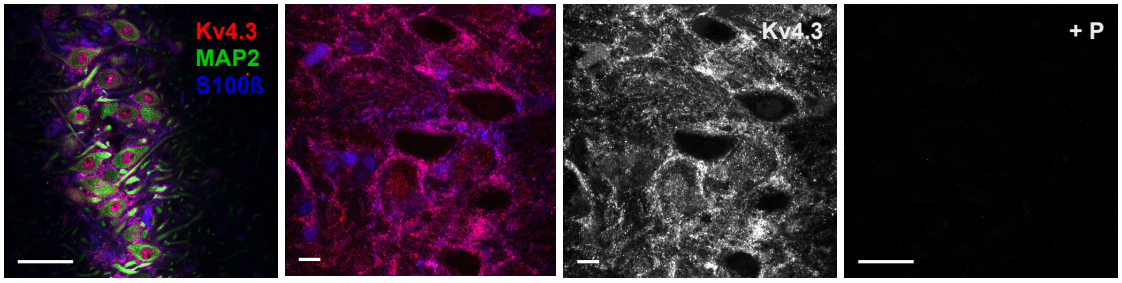

Figure 14: Kv4.3 was expressed in MSO neuron surrounding glia only. The glial marker S100β shows the same labeling pattern as Kv4.3. Looking at the control peptide it showed that the described staining was specific.

To summarize, in addition to the LVA and HVA channels, those that mediate an A-type current were also expressed on neurons of the mature MSO. Each of these showed a distinct expression profile, which partly overlap. In addition, we found Kv4.2 and 4.3 also expressed by MSO glia cells.

3.1.4 Overall expression pattern

Taken together, neurons of the mature MSO express a high variety of Kv channels, including LVA and HVA channels as well as those mediating an A-type current. To get a better understanding of possible functional implications the expression of all analyzed channels are summarized in one graph (Figure 15). Here, a clearly distinct expression pattern in neurons of the MSO depending on the Kv channel subfamily becomes evident. The LVA channels Kv1.1 and Kv1.6 showed a soma and proximal dendrite biased expression similar to MAP2 (Figure 15). Kv1.2 was expressed more distally into the dendrites than Kv1.1 and 1.6. In complement to one another, the HVA channels with slow kinetics Kv2.1, 2.2 showed a similar expression as Kv1.2. They were expressed along the whole MSO neuron and even showed a tendency to be biased towards the distal dendrites.

The fast HVA channels were localized more towards the somatic region. This was especially the case for Kv3.2, which expression was more biased towards the soma than that of MAP2, as indicated by the Gaussian ratio being smaller than 1. Receptors mediating the A-type current were expressed along the whole neuron. Here, the analyzed channels Kv1.4, Kv3.3 and Kv4.1 showed a very similar expression profile along the whole neuron.

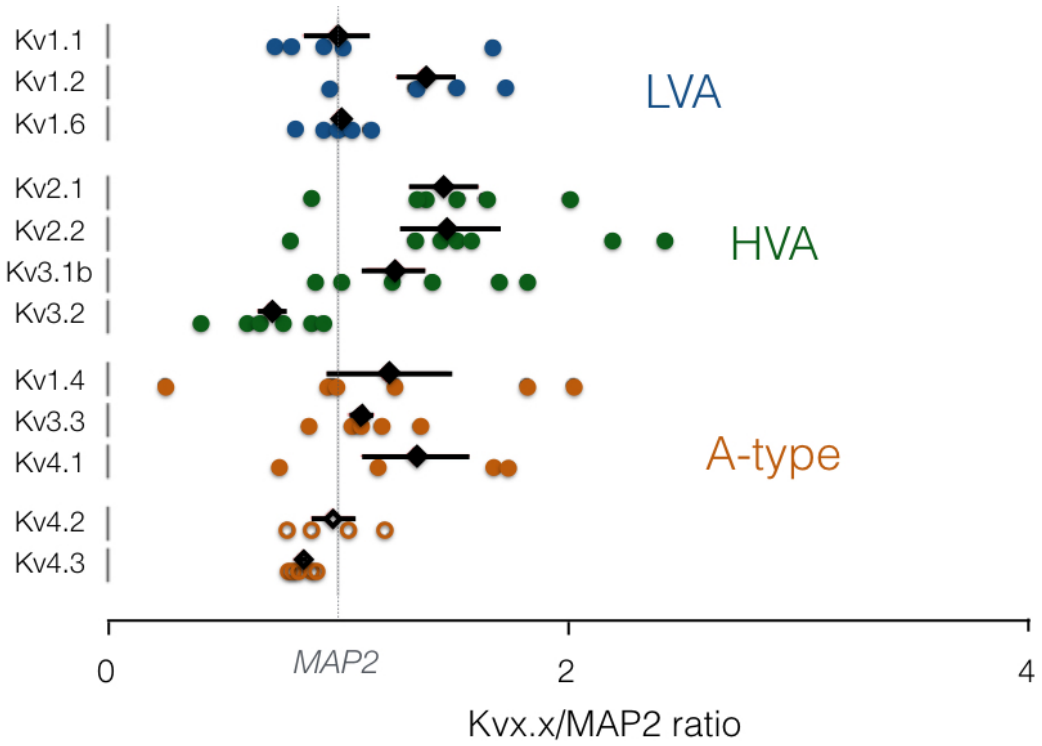

Figure 15: Kv channel distribution based on the semi-quantitative distribution analysis. Each black circle represents the value of a single cell. Blue circles show distribution of the LVA, green of the HVA and orange of the A-type potassium channels. Open circles show channels with no expression in MSO neurons. In black are the means for the corresponding Kv channel and lines show the SEM, respectively.

The A-type current mediating channels Kv4.2 and 4.3 were shown to be expressed by MSO glia. Soma surrounding glia specifically expressed these. Therefore this study showed a large diversity of Kv channels and their distinct expression profiles.

3.2 Developmental changes in calcium entry sites

Contributions towards this project: Experimental design for calcium imaging and electrophysiology towards fiber stimulation experiments came from my supervisor Prof. Dr. Felix Felmy. The idea for minimal fiber stimulation, GluR2 rectification experiments and initial thoughts on activity-dependency experiments came from me. Final experimental design for noise box experiments was evolved together with Delwen Franzen and Prof. Dr. Felix Felmy. All cells for fiber stimulation (in total: control: n = 44; noise box: n = 17) were recorded and analyzed by myself for the control and noise box condition. Two of the nine recorded cells for P11 minimal fiber stimulation experiments in control condition were recorded by my colleague Delwen Franzen. Additionally, for the noise box condition three of the P14 cells (n = 7) and three of the P17 cells (n = 7) were recorded by her. I recorded all other cells. All of these cells were analyzed by myself. All analysis and figure generation were done by myself. Calcium imaging analysis procedures were written in Matlab in collaboration with Christian Kellner.

All immunohistochemical stainings were planned, performed, imaged and further processed by me. In addition, all cells towards the analysis of the rectification index for AMPAR currents were recorded and analyzed by myself. All shown figures were generated by myself.

3.2.1 Calcium influx

Synaptic inputs onto MSO neurons are anatomically arranged with excitation mainly at the dendrites and inhibition on the soma in the mature system (Clark, 1969; Couchman et al., 2012). For inhibition it has been shown that its

synaptic refinement is experience-dependent as the exposure to omnidirectional noise persistently disturbed this refinement (Kapfer et al., 2002; Werthat et al., 2008). However, when and how the excitatory inputs refine and whether their refinement is also dependent on experience has not been elucidated yet. In the mature system excitation is glutamatergic and mainly mediated by AMPARs (Clark 1969; Couchman et al., 2012; Kil et al., 1995; Smith et al., 1993; Stotler 1953). The presence of NMDARs has been shown in the mature system, but their exact role here is not clear (Couchman et al., 2012). During development, and especially for the refinement of synaptic inputs, plasticity mechanisms play a crucial role. The presence of NMDARs and also the high calcium permeability of present receptors play an important role for plasticity and thus refinement processes (Chen et al., 1998). Consequently, the calcium permeability of the present receptors can give insight into periods of high plasticity.

In the following, AMPAR and NMDAR mediated calcium influx were investigated around and after hearing onset until maturity. Towards this aim, neurons of different ages were recorded and EPSCs were evoked by fiber stimulation. Calcium influx of the glutamate receptors present along the dendrites was evaluated by calcium imaging. The neurons were filled with an OGB-1 dye, enabling simultaneous calcium influx visualization at the synaptic site while stimulating with different trains. Four different stimulation trains were used to evoke postsynaptic EPSCs. The stimulation consisted of either a single pulse, three pulses, ten pulses or 25 pulses at 100 Hz.

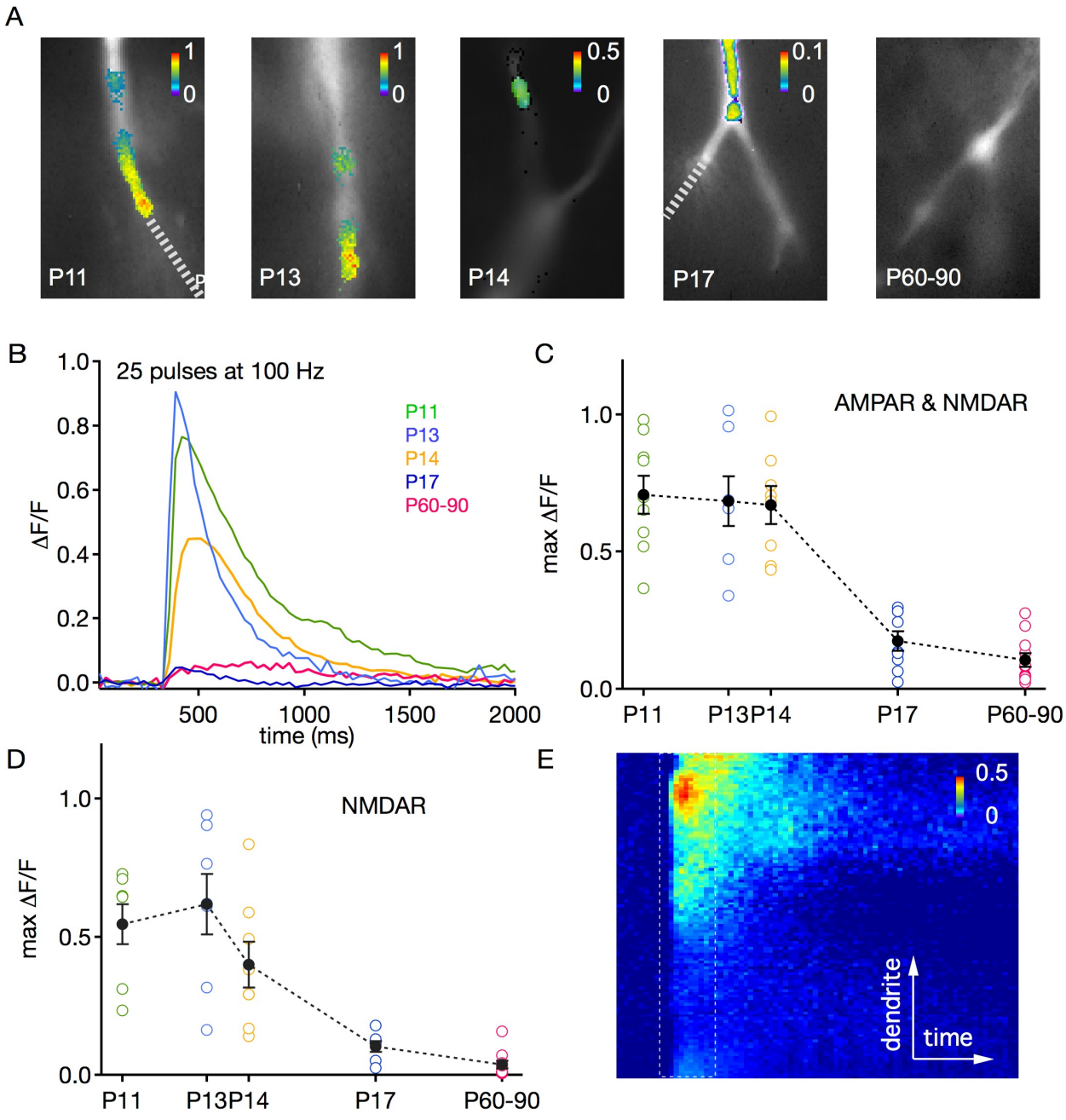

Figure 16: Developmental changes in AMPAR and NMDAR mediated calcium influx. A: Example images for all ages of the imaged dendrites for single pulse stimulation. Images are maximum projections of analyzed stack (grey scale image) plus ΔF/F projection (color code). B: Calcium influx evoked by 25 pulses at 100 Hz decreases from P11 to P60-90. ΔF/F values over the stimulation period for one cell. C & D: Closed black circles: Mean over all cells of maximally reached ΔF/F values for all analyzed ages in response to 25 pulses at 100 Hz. Each colored open circle represents a single cell, mean over three repetitions. C: Calcium influx through AMPAR and NMDAR. D: Calcium influx after AMPAR block using DNQX. E: Example kymograph for P14 cell shown in A. X-axis is time and y-axis dendrite location. During later analysis, the ΔF/F sum over the indicated time (square) was always used.

Here, an overall downregulation in calcium influx during late postnatal development was observed (Figure 16, A & C). While at P11, 25 pulses evoked a massive calcium influx (ΔF/F max: 0.9), the same stimulation train led to a strongly decreased calcium influx at P17 already (ΔF/F max: 0.08).

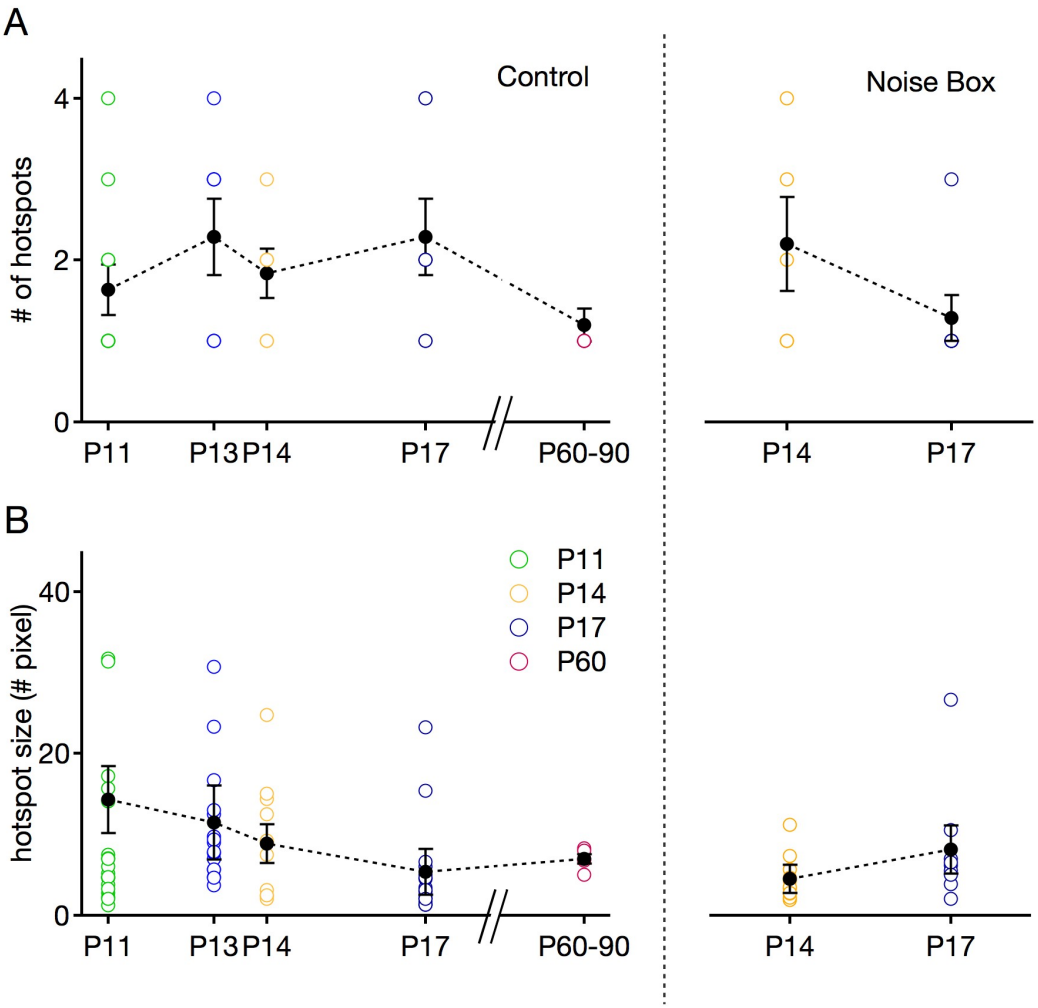

Figure 17: Calcium hotspot size and number decreased during development. A: Number of hotspots was determined by estimating the number of distinct hostpots present in kymographs. B: Estimated size of the before shown hotspots in number of pixels.

The AMPAR and NMDAR mediated calcium influx evoked by 25 pulses at 100 Hz stayed relatively constant until P14 (P11: 0.71 ± 0.07, n = 8; P13: 0.68 ± 0.09, n = 7; P14: 0.67 ± 0.07, n = 8) and decreased drastically by P17 (0.17 ± 0.04,

n = 8) and P60-90 (0.10 ± 0.03, n = 11; Figure 16, C). The same was the case for the NMDAR mediated calcium influx after AMPAR block using DNQX (Figure 16, D). However, it seemed that NMDAR calcium influx peaked at P13 (P11: 0.54 ± 0.07, n = 6; P13: 0.62 ± 0.12, n = 7; P14: 0.40 ± 0.04, n = 8; Figure 16, D).

In between experiments and especially ages the number and size of activated calcium hotspots along the dendrite varied (Figure A, E). This is most likely linked to the number of activated fibers represented by the number of activated spots on the dendrite (Figure 16, A). Therefore, the overall calcium influx depended on the spread of the calcium signal along the dendrite. This becomes particularly obvious when looking at the kymograph, which represents the calcium signal along the dendrite over time (Figure 16, A).

To roughly evaluate whether the actual number and size of calcium influx hotspots changed during development, their size was roughly estimated (Figure 17). Towards this analysis, the number of distinct hot spots with maximal ΔF/F values and their length was counted. The number of distinct hotspots decreased from P11 (1.64 ± 0.31; n = 11) to P60-90 (1.2 ± 0.2; n = 5; Figure 17, A). In addition, their size decreased throughout development (P11: 11.40 ± 3.89; P13: 10.70 ± 3.71, n = 7; P14: 9.31 ± 3.02, n = 6; P60-90: 7.00 ± 0.58; Figure 17, B). Thus, solely analyzing the peak ΔF/F values would underestimate the actual calcium influx if multiple hotspots were present. Therefore, it was necessary to sum up the ΔF/F values along the dendrite over time (30 ms) to get a better measure for the overall calcium influx. When comparing peak ΔF/F values with the summed ΔF/F values the overall trend stays. However, the summed ΔF/F values were seen as the more accurate representation of the actual calcium influx.

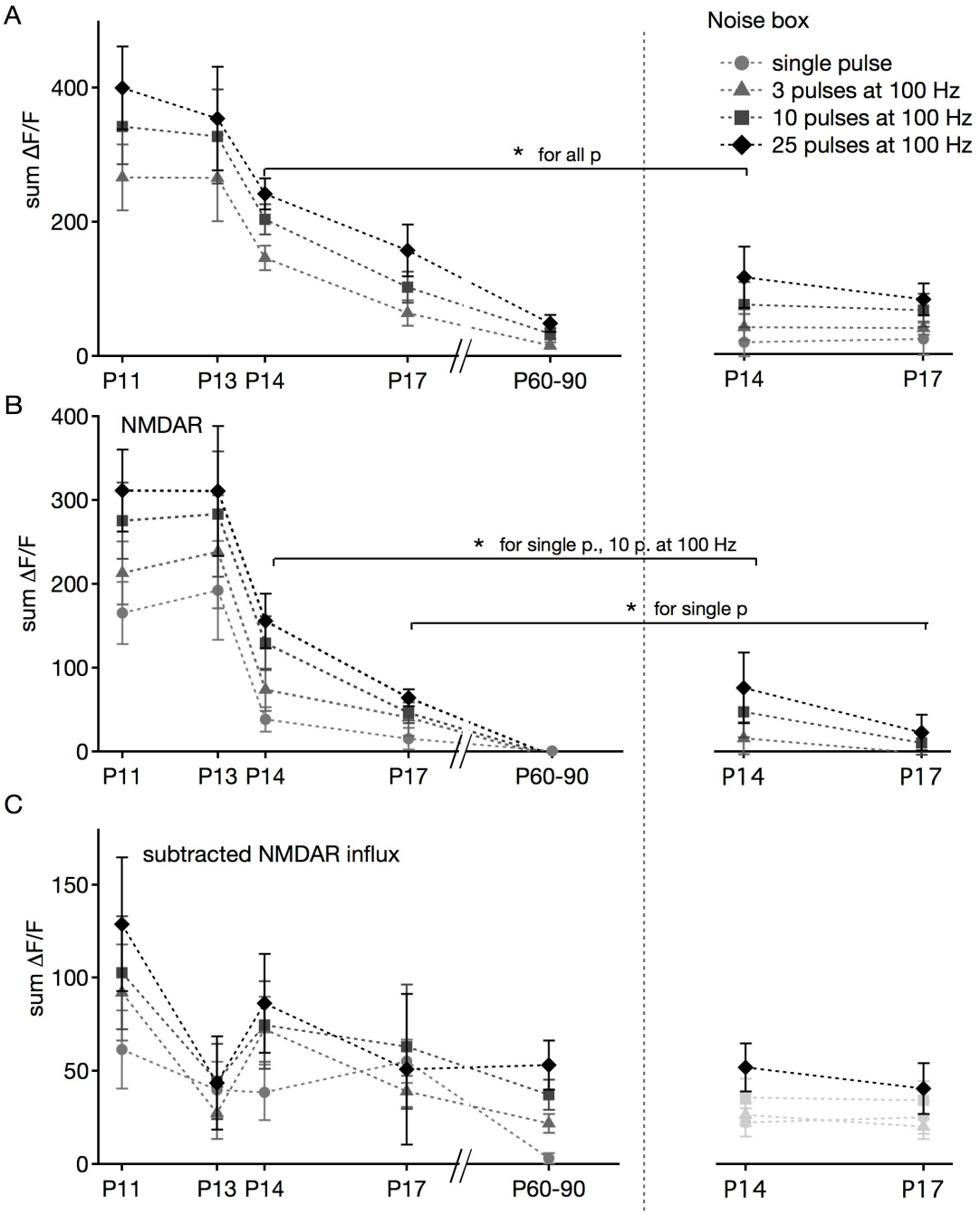

Figure 18: Calcium influx through AMPARs and NMDARs was developmentally downregulated. Each symbol represents mean over all cells for one stimulation train. ΔF/F summed values are presented to cover the whole signal. A: Developmental downregulation of calcium influx through AMPARs and NMDARs for all used pulse trains. Second panel: Calcium influx through AMPARs and NMDARs was significantly changed after omnidirectional exposure for P14 but not P17 for all used pulse trains. B: Calcium influx through NMDARs decreased during development and was undetectable at P60-90. Second panel: NMDAR mediated calcium influx was significantly changed by omnidirectional noise exposure for single pulse and 10 pulses at 100 Hz at P14 as well as for a single pulse at P17. C: From overall calcium influx subtracted AMPAR calcium influx. AMPAR mediated calcium influx was present at all ages but it also decreased throughout development. Second panel: Omnidirectional noise exposure (noise box) did not influence AMPAR mediated calcium influx refinement.

Summed ΔF/F values showed a slight decrease in overall calcium influx from P11 (single pulse: 188.87 ± 40.48; 3 pulses: 266.19 ± 48.88; 10 pulses: 341.91 ± 56.41; 25 pulses: 399.71 ± 62.12; n = 7) to P13 (single pulse: 231.87 ± 60.69; 3 pulses: 265.30 ± 64.86; 10 pulses: 327.10 ± 70.34; 25 pulses: 353.92 ± 77.10; n = 7) for all pulses (Figure 18, A).

From P13 on the calcium influx decreased rapidly. The influx in response to a single pulse decreased from 231.87 ± 60.69 at P13 (n = 7) to 76.63 ± 20.31 at P14 (n = 8) and was at 41.88 ± 17.69 at P17 (n = 8) and 3.34 ± 2.90 at P60 (n = 11). This was the case for all stimuli used but the effect was strongest for the higher pulse numbers (Figure 18, A).

The observed decrease in calcium influx could be due to a decrease in either AMPAR or NMDAR mediated calcium influx. Thus, after baseline recordings AMPAR mediated currents were blocked using DNQX (20 µM). The remaining signal was rated as NMDAR mediated calcium influx and the AMPAR contribution was calculated by subtracting the NMDAR from the baseline signal.

AMPAR mediated calcium influx decreased but was present at all investigated developmental stages and in all pulses (single pulse: P11: 23.64 ± 20.93; P13: 39.75 ± 15.16; P14: 38.36 ± 13.22; P17: 31.48 ± 13.76; P60-90: 3.05 ± 2.90; Figure 18, B). At P11 and P13 the main calcium influx source was NMDAR (single pulse: P11: 165.23 ± 37.28; P13: 192.13 ± 58.85; Figure 18, C). At P13 NMDAR mediated calcium influx peaked and switched to predominantly AMPAR mediated by P17 until it was almost solely AMPAR at P60-90 (NMDAR single pulse response: 0.42 ± 0.40). Consequently, the most significant changes in calcium influx happened around hearing onset. Therefore, it is postulated that a

plasticity window is present around P13. The finding that the number and size of hot spots along the dendrite decreased also indicates a refinement process taking place.

To test whether the refinements in calcium influx are experience-dependent like the somatic refinement of inhibition (Kapfer et al., 2002; Werthat et al., 2008), temporal cues were overlaid by omnidirectional noise from P9 on until the day of recording (see Methods & Material). In contrast to the refinement of inhibitory inputs, the refinement of AMPAR and NMDAR mediated calcium influx seemed to be independent of experience. At P14 the overall calcium influx through AMPARs and NMDARs decreased significantly for all stimulation paradigms after the exposure to omnidirectional noise during late postnatal development (single pulse: Control (Ctrl): 76.63 ± 20.31, n = 8; noise box (NB): 17.70 ± 13.94, n = 6; p = 0.025, 3 pulses at 100 Hz: C: 145.88 ± 18.18; NB: 40.33 ± 21.42; p = 0.001, 10 pulses at 100 Hz: Ctrl: 203.71 ± 22.78; NB: 74.47 ± 33.89; p = 0.004, 25 pulses at 100 Hz: Ctrl: 241.61 ± 23.21; NB: 115.03 ± 45.90; p = 0.014, Figure 18, A: second panel). These findings indicated an earlier maturation of the synapses under the influence of omnidirectional noise, as the calcium influx at P14 in omnidirectional noise conditions is more similar to that at P17 in normal acoustic environment. At P17 the refinement of calcium entry sites was not significantly changed (single pulse: Ctrl: 41.88 ± 17.67, n = 8; NB: 22.73 ± 13.94, n = 9; p = 0.278, 3 pulses at 100 Hz: Ctrl: 66.18 ± 18.11, NB: 39.16 ± 10.11; p = 0.212, 10 pulses at 100 Hz: Ctrl: 102.35 ± 23.25; NB: 65.97 ± 24.48; p = 0.158, 25 pulses at 100 Hz: Ctrl: 157.60 ± 38.14; NB: 82.10 ± 23.68; p = 0.055), thus refinements were not persistently disturbed.

Interestingly, the mean number of activated hotspots did not change in omnidirectional noise at P14 (2.2 ± 0.58, n = 5, Figure 17, A) but was decreased at P17 (1.29 ± 0.29, n = 7, Figure 17, A). The mean hotspot size was increased at P14 (4.48 ± 1.73) and was similar to control conditions at P17 (8.13 ± 2.99). Taken together, these findings support the hypothesis that omnidirectional noise exposure did not persistently disturb the refinement process but rather lead to faster maturation.

The NMDAR mediated calcium influx was significantly different for a single and 10 pulses at 100 Hz at P14 (single pulse: Ctrl: 34.83 ± 14.54, n = 8; NB: - 5.42 ± 12.99, n = 6; p = 0.042; 10 pulses at 100 Hz: Ctrl: 129.19 ± 32.06; NB: 44.77 ± 35.82; p = 0.043; Figure 18, C: second panel). Nevertheless, it gave a trend that was close to significance level for all other stimulation trains (3 pulses at 100 Hz: Ctrl: 73.55 ± 25.28; NB: 16.70 ± 22.70; p = 0.058; 25 pulses at 100 Hz: Ctrl: 155.38 ± 32.44; NB: 67.44 ± 50.26; p = 0.059). At P17 only a single pulse at P17 showed a significant difference between control and noise box condition (single pulse: Ctrl: 16.50 ± 16.11, n = 5; NB: - 15.17 ± 3.24, n = 7; p = 0.036). However, it showed the trend that NMDAR mediated calcium influx was decreased after omnidirectional noise exposure (3 pulses at 100 Hz: Ctrl: 43.65 ± 27.39; NB: -2.29 ± 4.89; p = 0.066; 10 pulses at 100 Hz: Ctrl: 38.16 ± 15.89; NB: 10.37 ± 13.88; p = 0.13; 25 pulses at 100 Hz: Ctrl: 54.19 ± 2.71; NB: 22.58 ± 21.36; p = 0.16).

The calculated calcium influx through AMPARs was not significantly different neither at P14 nor at P17 (Figure 17, B: second panel). To exclude that the size of the calcium hot spot contaminates the result in the summed analysis

approach additionally a ΔF/F peak analysis was performed again. Interestingly, the peak ΔF/F responses changed significantly for 10 and 25 pulses at 100 Hz at P14 (Ctrl: 10 pulses at 100 Hz: 0.35 ± 0.08; 25 pulses at 100 Hz: 0.40 ± 0.08; NB: 10 pulses at 100 Hz: 0.16 ± 0.05; 25 pulses at 100 Hz: 0.17 ± 0.06; p = 0.045; p = 0.038) and at P17 (Ctrl: 10 pulses at 100 Hz: 0.07 ± 0.02; 25 pulses at 100 Hz: 0.10 ± 0.02; NB: 10 pulses at 100 Hz: 0.03 ± 0.01; 25 pulses at 100 Hz: 0.03 ± 0.01; p = 0.051; p = 0.009), but not for single pulse and 3 pulses at 100 Hz (P14: Ctrl: single pulse: 0.16 ± 0.04; 3 pulses at 100 Hz: 0.23 ± 0.02; NB: single pulse: 0.08 ± 0.03; 3 pulses at 100 Hz: 0.13 ± 0.04; p = 0.096; P17: Ctrl: single pulse: 0.04 ± 0.03; 3 pulses at 100 Hz: 0.07 ± 0.03; NB: single pulse: 0.02 ± 0.01; 3 pulses at 100 Hz: 0.02 ± 0.01; p = 0.170; p = 0.118). The fact that for higher train numbers the peak ΔF/F responses changed more than for the summed could be due to the fact that the relative fiber number that is activated does not change. Thus, the area of high ΔF/F responses does not increase and therefore the sum does not increase as much. Taken together, the two approaches indicate that the NMDAR mediated calcium influx does change after omnidirectional noise exposure.

The respective synaptic currents from these recordings were analyzed in the following experiments.

3.2.2 AMPAR and NMDAR currents

The above-described changes in calcium influx through AMPARs and NMDARs could be based on a change in receptor current and/or subunit composition. The first was assessed by measuring the evoked EPSCs and evaluating AMPAR and NMDAR currents. In general, the NMDAR mediated current decreased throughout development while AMPAR EPSCs increased in peak current (Figure 19, A).

AMPAR peak current increased during development for all stimulation trains (single pulse: P11: -1.91 ± 0.49 nA, n = 7; P13: -3.29 ± 0.70 nA, n = 7; P14: -2.23 ± 0.37 nA, n = 7; P17: -3.11 ± 0.79 nA, n = 6; P60: -6.92 ± 0.96 nA, n = 8; Figure 19, B). Exposing the developing system to omnidirectional noise did not change the AMPAR peak current at P14 for neither of the used stimulation trains (Figure 19, B: second panel). However, at P17 AMPAR peak currents were significantly increased (single pulse: -6.18 ± 1.1 nA, n = 7; 3 pulses at 100 Hz: -3.37 ± 0.84 nA, n = 4; 10 pulses at 100 Hz: 8.00 ± 0.80 nA, n = 4; 25 pulses at 100 Hz: 8.17 ± 0.84 nA, n = 4, Figure 19, B: second panel) for all used stimulation trains ($p = 0.023, 0.041, 0.026, 0.020$, respectively). At the same time the AMPAR mediated charge stayed relatively constant and only decreased from 8.14 ± 2.79 pC at P11 to 6.90 ± 1.05 pC at P60 – 90 for a single pulse (Figure 19, C).

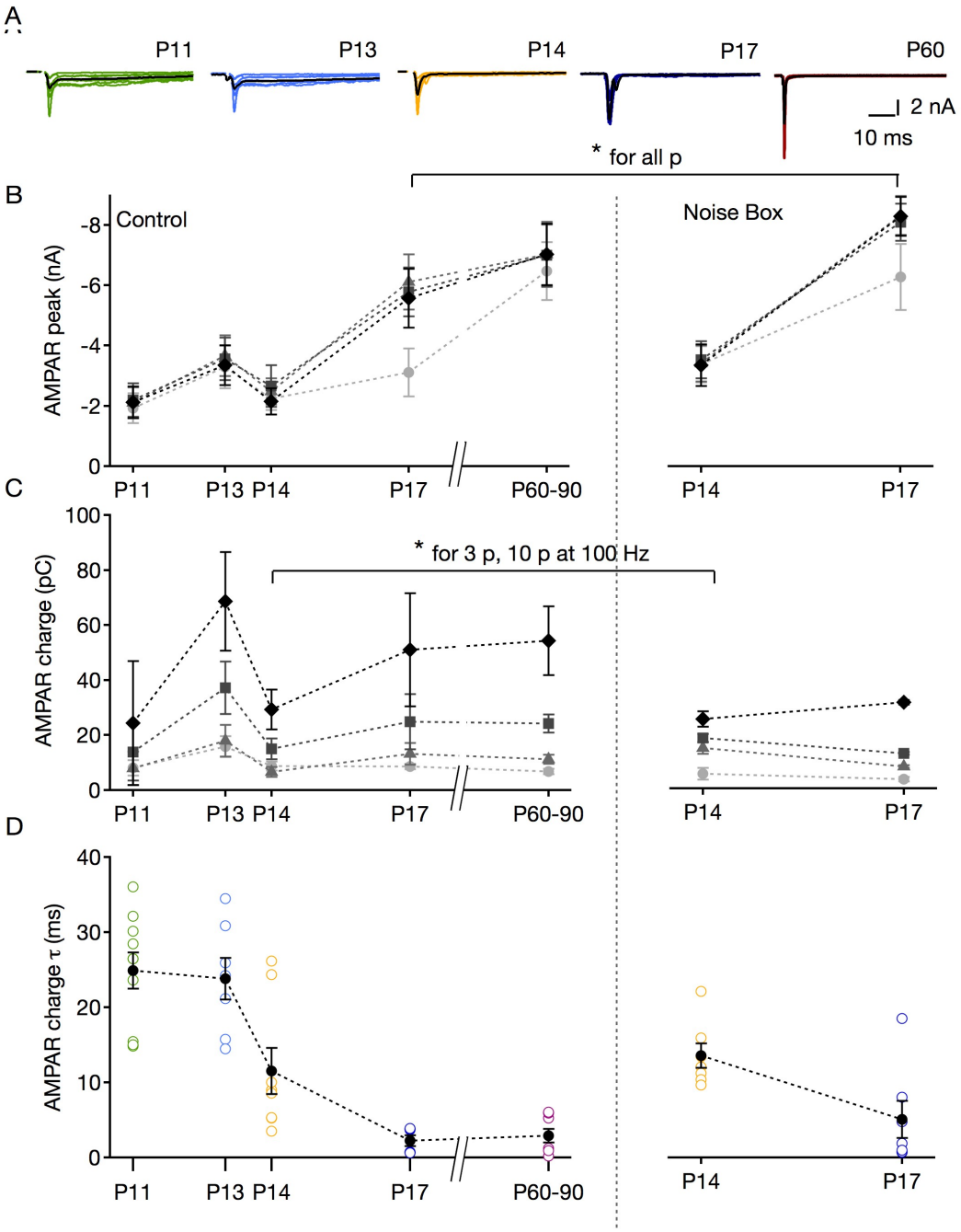

Figure 19: Development of AMPAR mediated synaptic inputs. A: Overlay of raw traces for all analyzed cells and their average (black). B: First panel: Peak AMPAR current for all used stimulation trains (circle: single pulse; triangle: 3 pulses at 100 Hz; rectangle: 10 pulses at 100 Hz; standing rectangle: 25 pulses at 100 Hz). Second panel: AMPAR mediated charge did not change after the exposure to omnidirectional noise. C: First panel: AMPAR charge in pC for all used stimuli. Second panel: AMPAR charge did not to change after noise box exposure. D: First panel: AMPAR decay time constant decreased during development. Second panel: Developmental decrease in AMPAR time constant was not changed after noise exposure.

This small decrease in charge from P14 to P17 was also seen after the exposure to omnidirectional noise (Figure 19, C: second panel). The fact that the AMPAR mediated charge decreased during development indicated an increase in its time constant. Indeed, the AMPAR charge decay time constant decreased from 24.9 ± 2.4 ms at P11 to 2.9 ± 0.9 ms at P60-90 (Figure 19, D). This developmental decrease in AMPAR decay time constant was not dependent on experience, as it did not change after omnidirectional noise exposure (Figure 19, D: second panel).

In contrast to the increase in AMPAR peak, the NMDAR mediated peak current decreased from -0.822 ± 0.134 nA at P11 to -0.004 ± 0.013 nA at P60 – 90 for a single pulse (Figure 20, A). The same was true for all stimulation trains (Figure 20, A). This developmental decrease in NMDAR peak currents was significantly different when exposing the animals to omnidirectional noise for some of the used stimulation trains (Figure 20, A).

Here at P14, the 3 and 10 pulses at 100 Hz evoked NMDAR peak currents were significantly larger (3 pulses at 100 Hz: -0.35 ± 0.007 nA, n = 6; p = 0.035; 10 pulses at 100 Hz: -0.34 ± 0.007 nA, n = 6; p = 0.045) than under normal conditions. For single and 25 pulses at 100 Hz stimulations NMDAR peak currents were not changed. Thus, NMDAR refinement was not dependent on experience.

NMDAR mediated charge decreased during development from 20.14 ± 3.59 pC at P11 to 2.68 ± 0.80 pC at P60-90 (Figure 20, B: second panel). This developmental downregulation of NMDAR EPSC mediated charge was not altered when exposing the animals to omnidirectional noise.

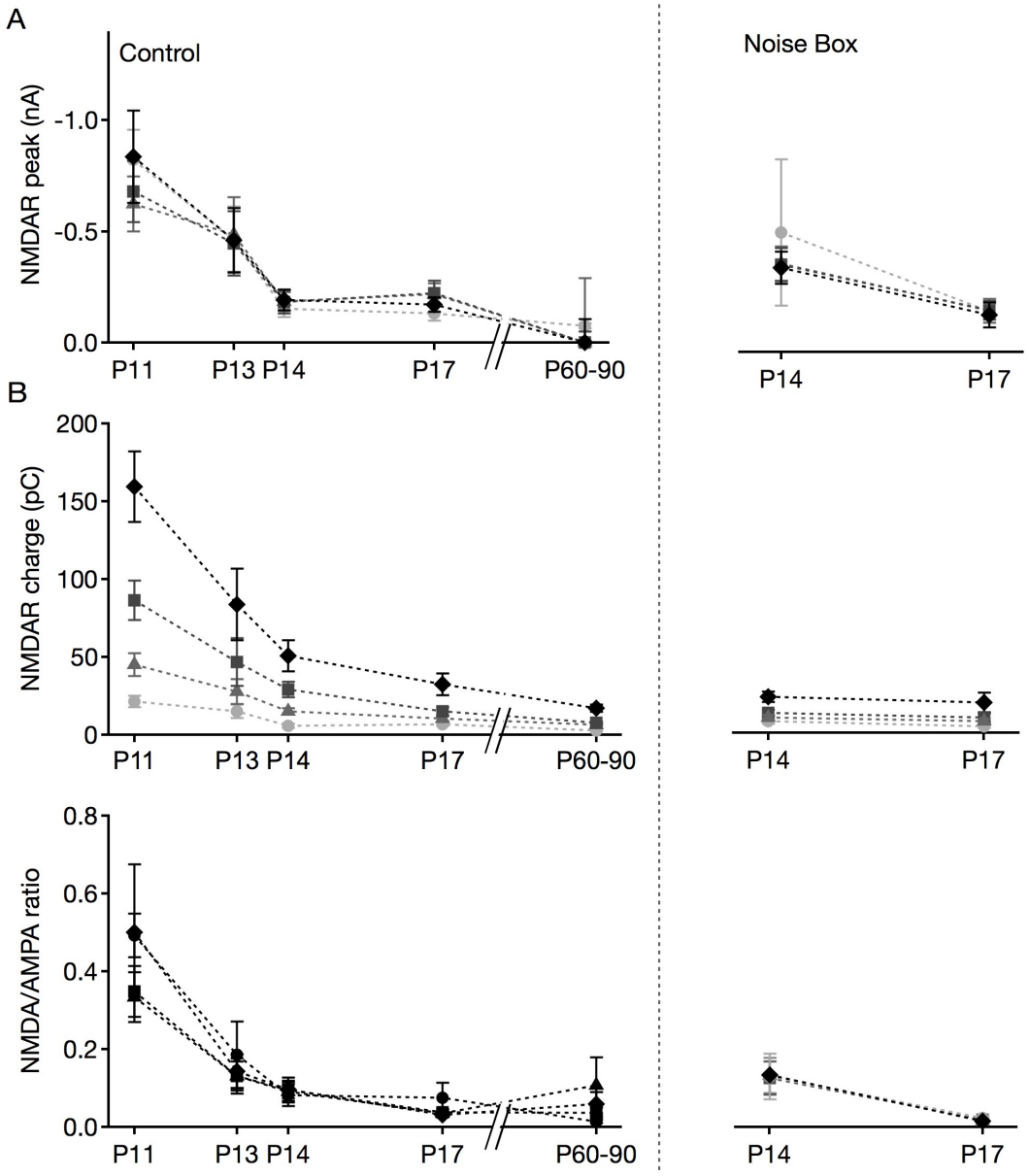

Figure 20: Development of NMDAR inputs. A: First panel: Peak NMDAR current during development for all used stimulation trains (circle: single pulse; triangle: 3 pulses at 100 Hz; rectangle: 10 pulses at 100 Hz; standing rectangle: 25 pulses at 100 Hz). Second panel: NMDAR EPSC mediated charge did not change after omnidirectional noise. B: First panel: NMDAR charge during development in pC for all used stimuli. Second panel: NMDAR charge was neither experience nor activity dependent. C: NMDAR/AMPAR peak current ratio.

Overall, the NMDAR/AMPAR peak ratio decreased during postnatal development (single pulse: P11: 0.51 ± 0.06; P13: 2.48 ± 0.29; P14: 0.18 ± 0.03;

P17: 0.08 ± 0.04; P60: 0.01 ± 0.004), leaving the mature system with basically AMPAR mediated currents only (Figure 20, C). This refinement in excitatory receptor composition seemed to be independent of experience as animals raised in omnidirectional noise showed a similar refinement (Figure 20, C). However, a slight trend that the omnidirectional noise induced a faster development of the NMDAR/AMPAR ratio could be seen but this was not statistically relevant ($p = 0.23$).

Taken together, the developmental refinements in AMPAR and NMDAR peak currents were not dependent on experience.

3.2.3 Subunit composition

The decrease in AMPAR mediated calcium influx and its faster time constant could be due to a change in AMPAR subunit composition. Using immunohistochemical stainings the current mediating AMPAR as well as NMDAR subunit composition were analyzed.

Changes in AMPAR subunit composition influence channel kinetics, deactivation and desensitization properties but also its calcium permeability (Burnashev et al., 1992; Geiger et al., 1995; König et al., 2001; Mosbacher et al., 1994; for review see Dingledine et al. 1999). AMPARs are heteromeric complexes, composed of the subunits GluR1 - 4 (Rosenmund et al., 1998; Wenthold et al., 1996) with their majority containing GluR2 (Greger et al., 2002; Wenthold et al., 1996).

AMPARs containing GluR2 show a linear current-voltage relationship (Boulter et al., 1990), are calcium impermeable, and have a relatively low single-

channel conductance. In contrast, channels lacking GluR2 are calcium permeable, have a higher conductance, and are inwardly rectifying due to a voltage-dependent block by endogenous intracellular polyamines (Bowie et al., 1995; Geiger et al., 1995; Hestrin, 1993; Jonas et al., 1994; Kamboj et al., 1995).

The high calcium permeability of GluR2 lacking AMPARs could be important during developmental processes. To understand whether the changes in calcium influx during development are due to a change in AMPAR subunit composition, the expression of GluR2 was analyzed, immunohistochemically than electrophysiologically.

The immunohistochemical approach showed that GluR2 subunit was expressed at both ages (Figure 21, A). At P13 also MSO glia showed strong GluR2 expression that was not present at P60-90. Overall GluR2 expression appeared higher at P13 than at P60-90. Additional verification of immunohistochemical findings was done electrophysiologically by investigating the rectification of AMPAR currents. To do so the patch pipette contained spermine (20 µM) to prevent the washout of endogenous intracellular polyamines (Bowie et al., 1995, Kamboj et al., 1995, Koh et al., 1995). For eight voltage steps from -70 to +70 mV the rectification indices were calculated. AMPAR currents rectified more at P13 at +70 mV (mean rectification index at 70 mV: P13: 0.157 ± 0.036, n = 8; P60-90: 0.105 ± 0.036, n = 8; p = 0.0282; Figure 21, B) matching the immunohistochemical data.

The GluR4 subunit is a subunit that mediates fast large AMPAR currents. Thus, these were expected to be expressed throughout development. Indeed, the

immunohistochemical analysis showed strong GluR4 expression around hearing onset as well as in the mature MSO (Figure 21, D).

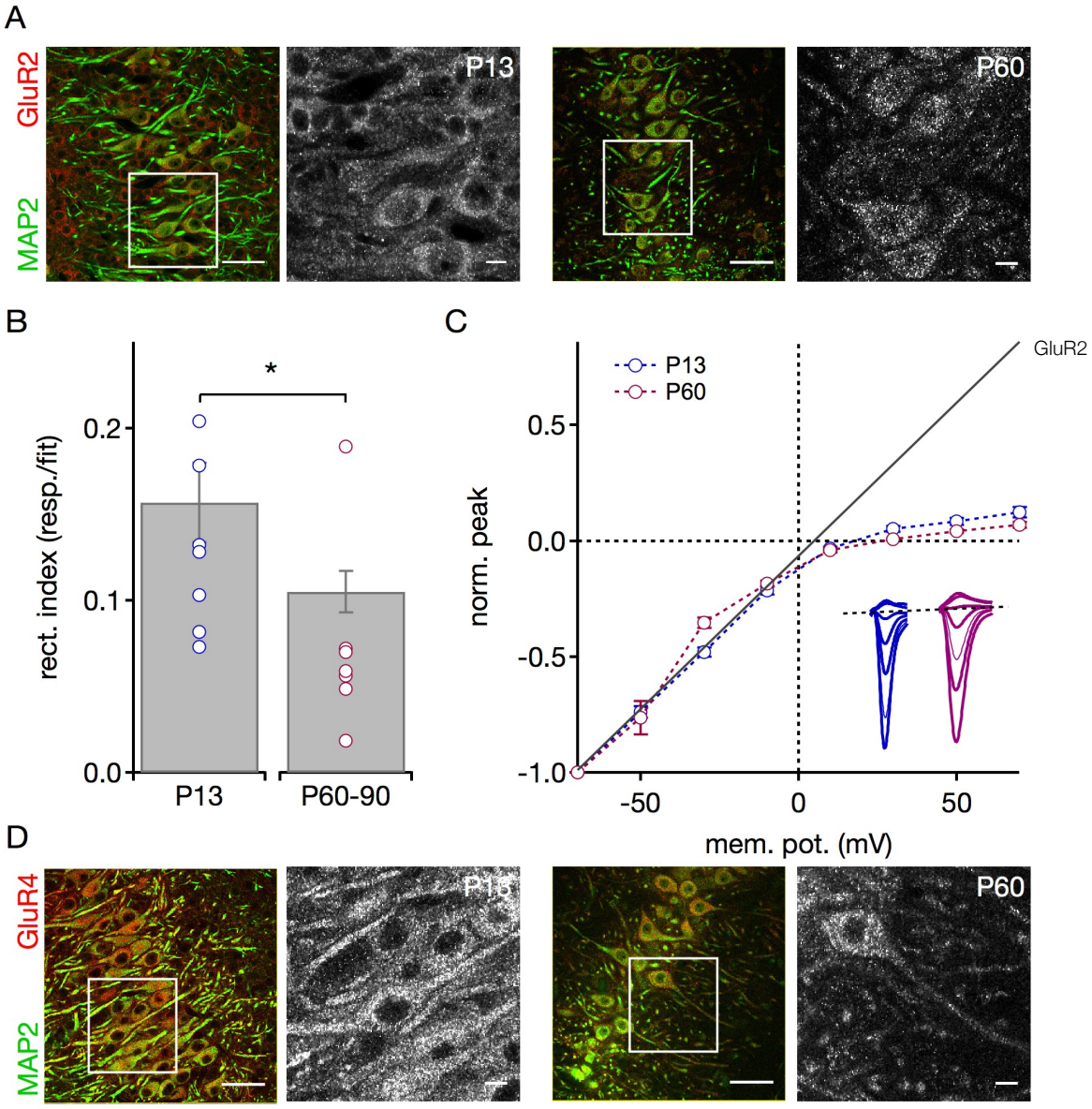

Figure 21: AMPAR subunit expression at P13 compared to P60. Scale bars in the overlay images are 50 µm and 10 µm in the zoomed-in grey scale images. A: The calcium impermeability mediating GluR2 subunit was expressed at P13 and P60-90. Grey scale image shows the zoomed-in GluR2 channel only. B: AMPAR currents have significantly stronger rectification indeces at P13 for 70 mV. Bar graphs show the means ± s.e.m and open circles are single cells. Rectification index was calculated from voltage responses to 70 mV by dividing the response current by the fit. C: Normalized rectification curves for P13 and P60-90. Peak responses were normalized to peak response at -70 mV. D: The GluR4 subunit and thus fast calcium permeable AMPARs are expressed at P13 and P60. GluR4 expression at P13 and P60 with MAP2 (green). Grey scale image is the zoomed in GluR4 channel only.

Taken together, the GluR4 subunit was expressed at both ages and GluR2 expression decreased. This fits the finding that AMPARs containing GluR4 but not GluR2 have the fastest channel kinetics (Geiger et al., 1995; Mosbacher et al., 1994). Thus, the found changes in calcium influx were most likely due to an increase in the AMPAR time constant caused by the decrease in GluR2 expression and the loss of NMDAR mediated EPSCs.

From P11 to P17 NMDARs form the second source for synaptically mediated calcium influx. The synaptically evoked NMDAR currents together with the mediated calcium influx decreased during development and vanished until P60-90. Fittingly, the receptor functionality mediating subunit GluN1 was expressed at P13 (Figure 22, A). Its expression seemed to be biased towards the dendrites at this developmental stage.

This subunit was also expressed at P60-90 (Figure 22, A) showing that functional NMDARs are still present in the mature MSO hinting at a different role in the mature system than during late postnatal development. This finding also fits earlier findings of NMDAR presence in the mature MSO (Couchman et al., 2012). To get a better understanding of NMDAR composition in the mature system the expression of the subunits GluN2A, B, C and D were also analyzed.

Channels containing GluN2A or GluN2B are more sensitive to magnesium block and mediate the most calcium influx compared to GluN2C- or GluN2D-containing channels (Monyer et al., 1994). GluN2A was expressed at both ages (Figure 22, B). Its expression appeared to be biased towards the soma and proximal dendrites at P13 as well as at P60. In contrast, the expression of GluN2B

underwent a developmental switch: at P13 it was hardly expressed and at P60 the whole MSO neuron expressed GluN2B (Figure 22, C).

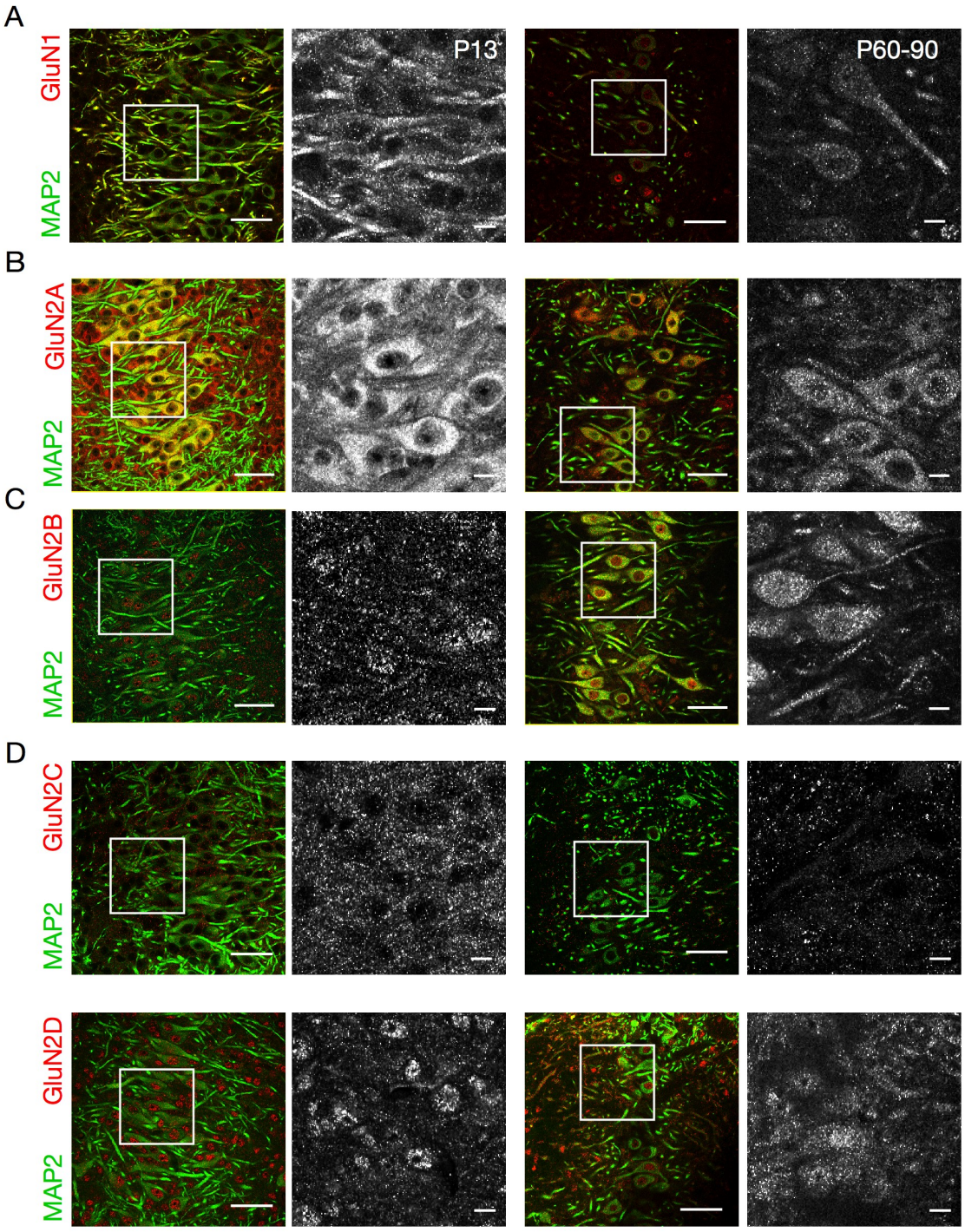

Figure 22: NMDAR subunit expression at P13 compared to P60. Scale bars in the overlay images are 50 µm and 10 µm in the zoomed-in grey scale images. Receptor staining is always depicted in red and MAP2 in green. The grey scale image is the receptor channel, respectively. A: Functional NMDARs are expressed at P13 and P60. B: GluN2A is expressed at P13 and P60. C: The GluN2B subunit is also expressed at both ages. D: The GluN2C and GluN2D subunits show no expression.

This supports the theory of a developmental switch in NMDAR function. GluN2C showed only little or no expression at both developmental stages (Figure 22, D). The GluN2D was expressed in MSO nuclei at P13 and in soma and dendrites it showed additional expression at P60-90 (Figure 22, D; lower panel).

Taken together, NMDAR channels are present that cannot be detected by electrophysiological methods at P60-90. The finding that only subunits that are highly permeable to calcium were expressed complemented this. During late postnatal development the NMDAR contribution decreased and NMDAR subunit composition changed, hinting at a change in NMDAR function in the system. Thus, it is likely that the high calcium influx during late postnatal development plays a role during plasticity mechanisms.

3.2.4 Synaptic refinements

To investigate whether during the hypothesized plasticity window refinements in synapse size happen, changes in excitatory transmission were analyzed during this period. Towards this aim the size of a single excitatory fiber synapsing on a MSO neuron at P11, P14 and P17 was measured. Here, minimal stimulation paradigms were used to estimate the single fiber evoked EPSC size. Independent fiber inputs were recorded using two different minimal stimulation protocols. First, stimulation intensities close to threshold were used to generate both, failures and EPSCs (Figure 23, A). Second, the stimulation intensities were raised in sub-voltage increments so that clear step-like increases in EPSC size were observed.

The mean peak size of a single excitatory fiber increased during late postnatal development from -0.82 ± 0.23 nA (n = 7) at P11 to -1.53 ± 0.31 nA P14 (n = 8) and further to -2.84 ± 0.78 nA at P17 (n = 7; Figure 22, B). This increase in single fiber size peak was significant from P11 to P17 (p-value = 0.0288, Figure 23, B).

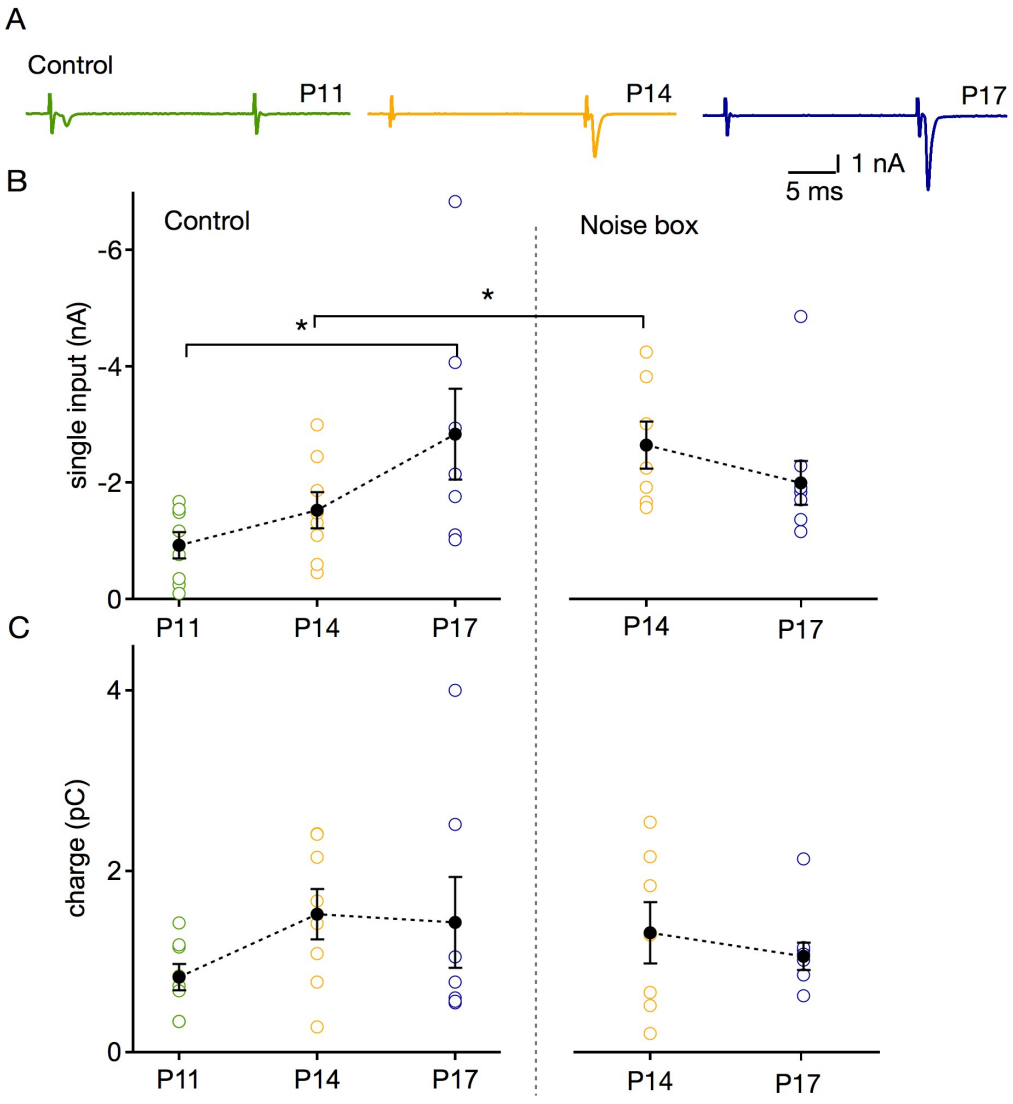

Figure 23: Analysis of basic EPSC properties. A: Excitatory fiber generated EPSC size increases from P11 to P14 and to P17. Example traces for single inputs at P11 to P17. Stimulation intensities close to threshold were used to generate both, failures and EPSCs. B: During development EPSC amplitude increased under control conditions (left panel). When animals were raised under omnidirectional noise (noise box) this increase in EPSC amplitude was faster. At P14 it was already as large as at P17. C: Single fiber mediated charge increased during late postnatal development. This did not change after the exposure to omnidirectional noise.

To test whether these refinements are dependent experience, animals were raised under omnidirectional noise in the noise box from P9 until the day of recording. This led to a significant increase in single fiber size at P14 (-2.71 ± 0.41 nA; n = 7) compared to control conditions (p-value = 0.0184; Figure 23, B). However, at P17 the single fiber size did not vary significantly from control conditions anymore (-1.66 ± 0.15 nA; p-value = 0.96; n = 8) indicating that these refinements are independent of experience.

In parallel to the changes in mediated peak current, the charge mediated per fiber also increased from 0.75 ± 0.11 pC at P11 (n = 7) to 1.53 ± 0.28 pC at P14 (n = 8) and further to 1.44 ± 0.50 pC at P17 (n = 7; Figure 23, C). However, this did not change significantly after raising the animals in omnidirectional noise: the mediated charge was 1.32 ± 0.34 pC at P14 (n = 7) and 1.06 ± 0.15 pC at P17 (n = 9; p-value = 0.13; Figure 23, C). This might be due to a change in the temporal profile of mediated currents and will be discussed later.

Next, the size of a single vesicle mediated EPSC was estimated by recording mEPSCs while exogenously blocking glycinergic and GABAergic inputs. These were extracted off-line with a threshold template matching routine as already described by others (Couchman et al., 2010; Taschenberger et al., 2000). The population median of the scored mEPSCs was determined by a Gaussian (Figure 24, A). The mean amplitude of a mEPSC did not change from P11 to P17 (P11: - 36.00 ± 4.01 pA, n = 7; P14: -43.78 ± 3.75 pA, n = 8; P17: 37.88 ± 5.64 pA, n = 7). The same was also true for the noise box condition (P14: - 40.57 ± 4.79 pA, n = 6; P17: - 37.30 ± 4.71 pA, n = 7; Figure 24, B) indicating that mEPSC size is not refined during late postnatal development.

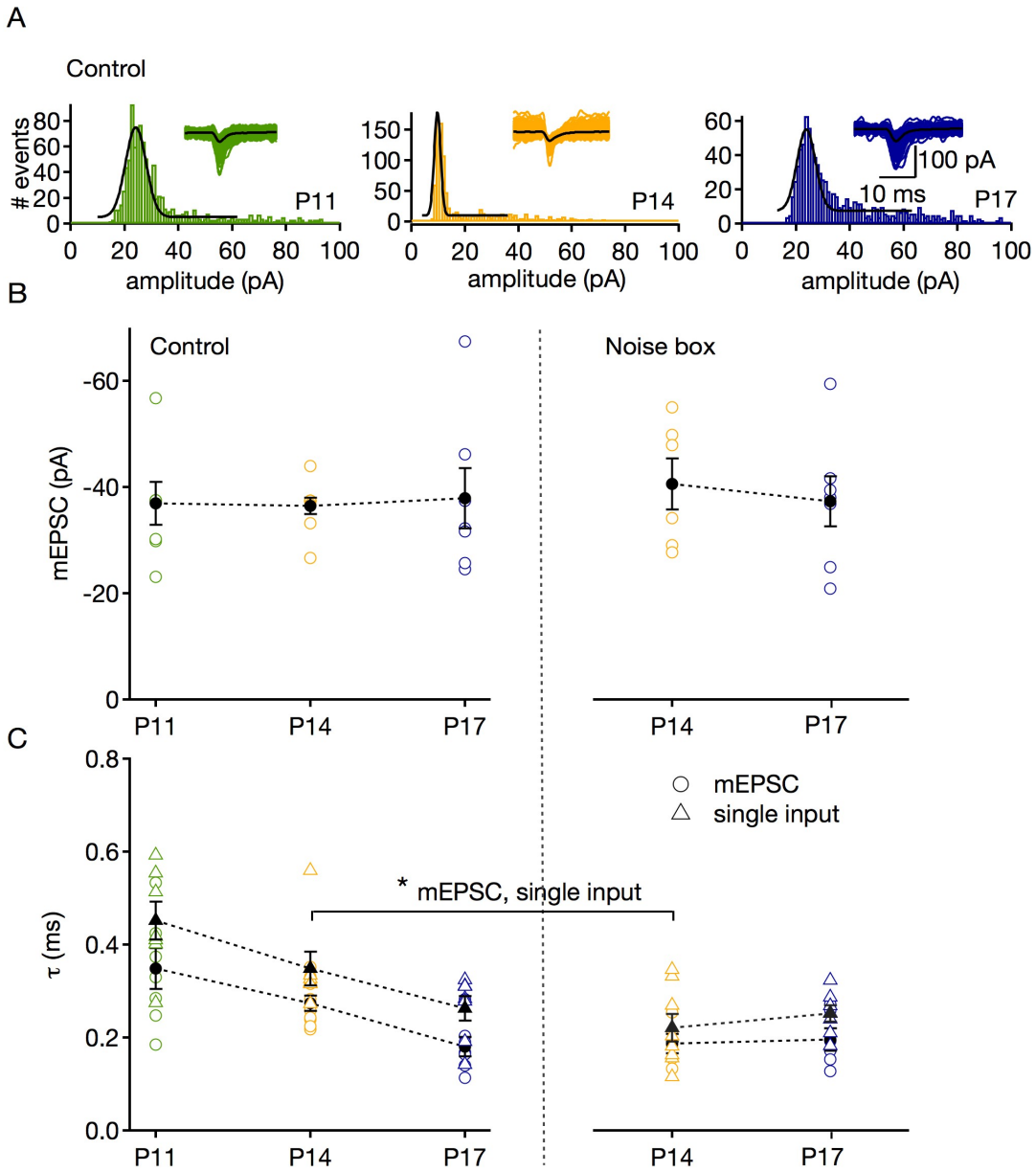

Figure 24: Analysis of mEPSC properties. **A:** Gaussian fitted mEPSC amplitudes for P11, 14 and 17. Inset shows overlay of 300 of the manually scored mEPSCs. **B:** The amplitude of mEPSC did not change from P11 to P17. The same was true after the exposure to omnidirectional noise. **C:** EPSCs as well as mEPSCs decreased in their time constants. This was changed significantly by omnidirectional noise.

The decay time constant of mEPSCs decreased from 340 ± 44 µs (n = 7) at P11 to 278 ± 18 µs (n = 8) at P14 and 180 ± 20 µs (n = 7) at P17 (Figure 24, C). Omnidirectional noise decreased the time constant from mEPSCs significantly

at P14 (186 ± 21 µs, n = 7; p-value = 0.007) and P17 (194 ± 22 µs, n = 7; p-value = 0.003; Figure 24, C).

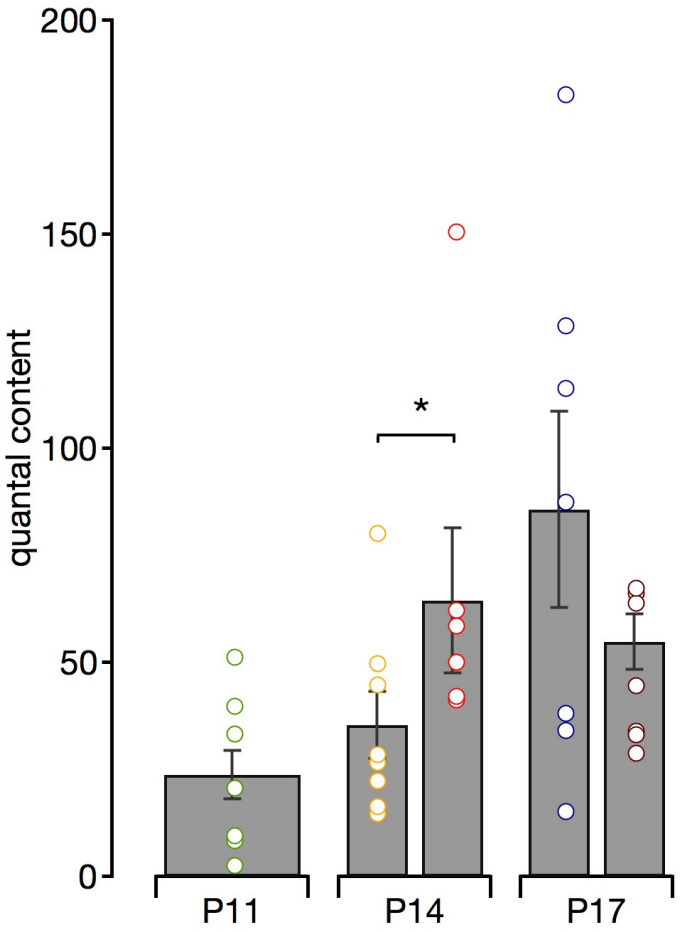

Figure 25: Quantal content increased from P11 to P17. This was changed significantly for P14 after omnidirectional noise exposure but was normal at P17. Open circles show single cell values (green: P11; yellow: P14; bright red: P14 NB; blue: P17; dark red: P17 NB).

In parallel, the time constant of single synaptic input decreased from 450 ± 41 µs (n = 7) at P11 to 349 ± 36 µs (n = 7) at P14 and to 262 ± 26 µs (n = 7) at P17 (Figure 24, C). Their time constant also changed significantly after the exposure to omnidirectional noise for P14 (202 ± 28 µs, n = 7; p-value = 0.003) but not for P17 (250 ± 18 µs, n = 7; p-value = 0.347; Figure 24, C). Taken

together, the time constant and the EPSC size showed the same developmental time course.

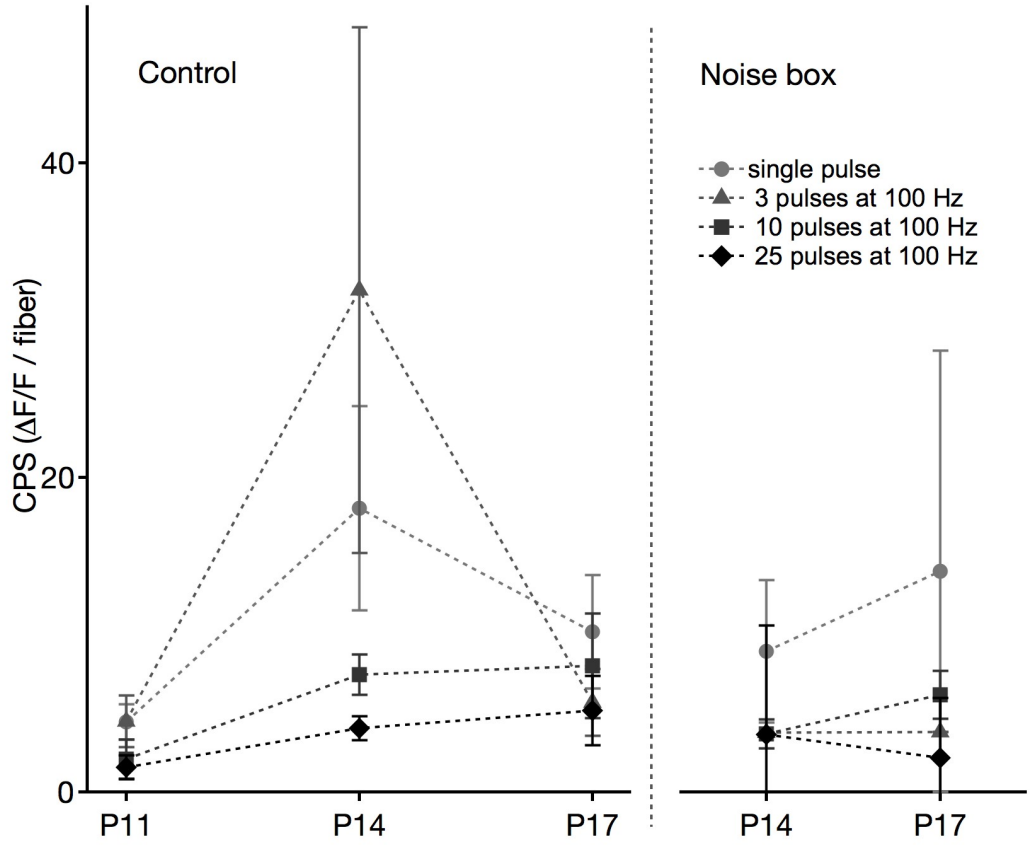

Figure 26: Changes in single fiber mediated calcium influx under control (left panel) and omnidirectional noise conditions (right panel) for all used stimulation trains. Symbols show the mean for the different pulse trains for each age. Error bars are SEMs. CPS is the calcium influx as summed ΔF/F values per single fiber.

These findings allow for quantal content estimation by dividing mEPSC size by the amplitude of a single fiber evoked EPSC. The quantal content describes the number of vesicles that are liberated with a single AP. The quantal content increased from 23.76 ± 5.64 at P11 (n = 7) to 35.31 ± 7.78 at P14 (n = 8) and to 85.68 ± 22.85 at P17 (n = 7; Figure 25). When the animals were raised in omnidirectional noise, this increase in synapse size was faster (Figure 25). Under these conditions the quantal content was significantly larger at P14 (67.38 ± 16.96, n = 7; p-value = 0.04) compared to control conditions. At P17 quantal

content size was comparable to P17 under normal conditions (45.11 ± 5.61, n = 8; p = 0.05).

Thus, the changes in synaptically mediated calcium influx and receptor composition happen in parallel to an increase in fiber size and decrease in time constant. To see whether the actual calcium influx mediated per fiber changes, the calcium influx mediated by one fiber was calculated. Towards this aim the charge evoked by the different stimulation intensities was divided by the charge mediated by a mEPSC.

The mean calcium influx mediated per fiber increased with age for a single pulse from 4.43 ± 1.13 at P11 (n = 7) to 18.03 ± 6.48 at P14 (n = 8) up to 10.16 ± 3.62 at P17 (n = 5; Figure 26). The same was true for all other pulses (3 pulses at 100 Hz: P11: 4.48 ± 1.64; P14: 31.89 ± 16.69; P17: 5.69 ± 2.11; 10 pulses at 100 Hz: P11: 2.08 ± 1.24; P14: 7.45 ± 1.27; P17: 8.02 ± 3.32; 25 pulses at 100 Hz: P11: 1.58 ± 0.75; P14: 4.04 ± 0.76; P17: 5.18 ± 2.21) under the influence of normal acoustical environment (Figure 26). After the exposure to omnidirectional noise the calcium influx mediated per fiber was not changed at P14 neither at P17 (Figure 26: second panel).

The calcium influx per overall charge also decreased from P11 to P60-90 (Figure 27). On average 25 pulses at 100 Hz mediated a charge of 184.66 ± 32.72 pC and a summed ΔF/F calcium influx of 399.71 ± 62.12 at P11 (Figure 27). At P14 the mediated charge decreased already to 79.80 ± 14.29 pC and the calcium influx to 241.61 ± 23.21. This maturation of the mediated charge continued until P17 with 71.12 ± 17.89 pC and then stayed relatively stable until P60-90 (69.65 ± 15.90 pC; Figure 27). However the calcium influx at P17 was still 130.08

± 38.85 and decreased to 48.66 ± 12.84 at P60-90. Thus, the EPSCs increased in their temporal profile with a decrease in NMDAR contribution and charge mediated calcium influx during late postnatal development.

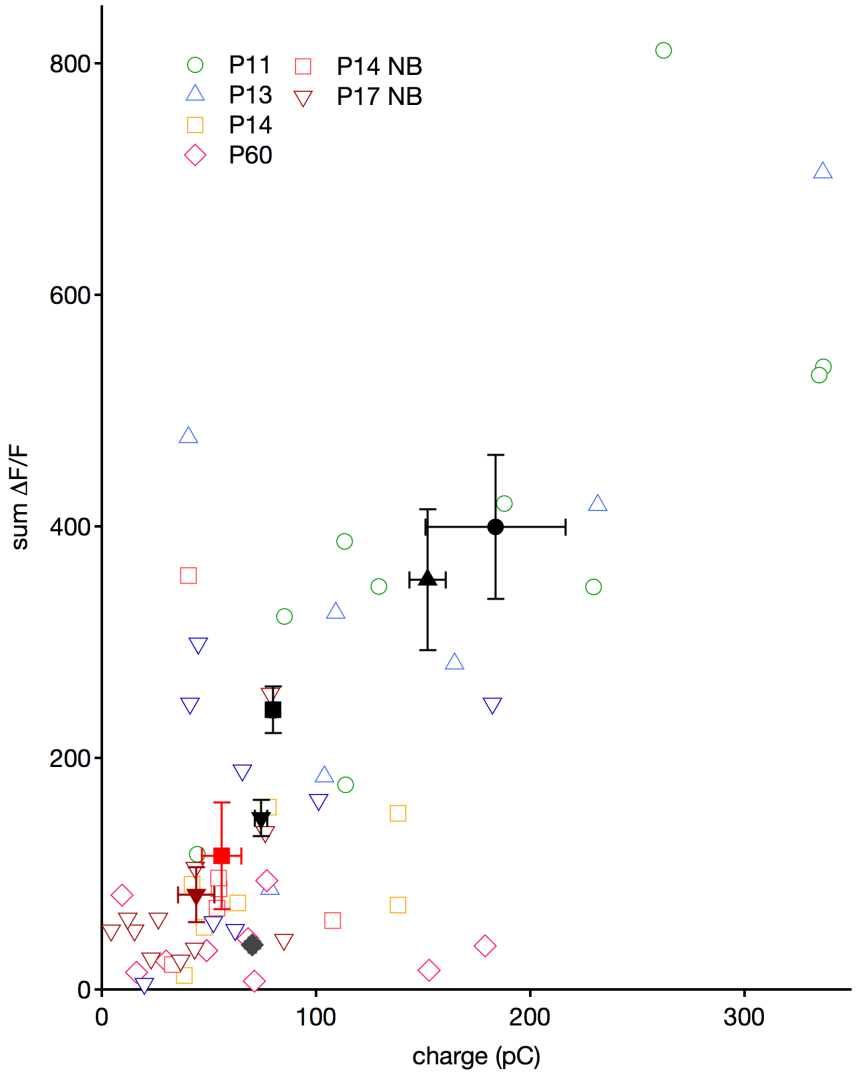

Figure 27: Overall charge mediated calcium influx decreased during late postnatal development. These refinements were independent of experience. Colored symbols represent single cell charge (pC) versus summed calcium influx in response to 25 pulses at 100 Hz. Corresponding black symbols represent the mean over all analyzed cells and their SEMs. Red and dark red show the responses for omnidirectional noise reared animals.

These refinements in calcium influx happened earlier when the animals were exposed to omnidirectional noise (Figure 26: second panel). At P14 a 25 pulse at 100 Hz stimulation mediated a comparable charge of 56.00 ± 9.14 pC (Ctrl: 79.80

± 14.29 pC; Figure 26). However the summed calcium influx was reduced by about one half (NB: 115.30 ± 45.90; Ctrl: 241.61 ± 23.21). In addition to the decreased calcium influx (NB: 82.08 ± 23.28; Ctrl: 130.08 ± 38.85) also the charge transfer in response to 25 pulses at 100 Hz was decreased to 44.03 ± 8.55 pC (Ctrl: 71.12 ± 17.89 pC). This was even less then the mediated charge at P60-90 in normal acoustic environment.

3.3 Binaural processing in the DNLL

Contribution towards this project: Experimental design came from my supervisor Prof. Dr. Felix Felmy. Introduction to setup and experimental procedure was done mainly by Helge Gleiss and partly by Dr. Ida Siveke. Dr. Annette Stange gave a short introduction to iontophoretic drug application and multi-barreled electrode construction. All of the shown cells for baseline and drug experiments were recorded by me. I built all of the used multi-barreled electrodes. Acoustic stimuli were generated together with Dr. Todd Jennings. The first steps of data analysis were done by myself in self-written Matlab programs, and graph generation for figure 28, 29 and 30 were done in these programs by myself. Dr. Ida Siveke did final analysis and figure generation, as shown in Figure 31, 32 and 33. Discussions on data analysis were always held together with Prof. Dr. Felix Felmy, Dr. Ida Siveke and Ph.D. Julian Ammer. Immunohistochemical stainings were performed, imaged and processed by myself.

3.3.1 Modification of firing frequency

In the previous chapter I could show that in the MSO, NMDARs are likely involved during developmental refinement processes and lose their significance during maturation, likely adopting a different physiological role. This is in line with the classic role of NMDARs during synaptic plasticity and learning (Jia et al., 2014; Palmer et al., 2014; Zhao et al., 2005, 2015). Their slow kinetics are ideally suited to transmit slow signals (Diamond et al., 1993), low firing rates (Schartz et al., 2012) or cause long latency spikes (Sanchez et al., 2007). Thus, NMDARs are not expected to be relevant in the mature auditory brainstem for fast information

transfer (Sanchez et al., 2015). However, in the DNLL, NMDAR signaling is established in the mature system *in-vitro* (Ammer et al., 2012; Fu et al., 1997; Porres et al., 2011; Wu et al., 1995) and also indirectly *in-vivo* (Chen et al., 1999; Kelly et al., 2000). Still, the computational and functional role of NMDAR mediated excitation for processing in the DNLL has not been fully elucidated. As introduced above, the DNLL possesses a pathway that processes auditory information in the order of the tens of milliseconds. Thus, the importance of NMDAR mediated excitation for this pathway was tested mediating the so-called persistent inhibition. Here, NMDAR subunit composition and functional role in the mature DNLL were investigated.

The presence and subunit composition of NMDARs was verified by using immunohistochemical stainings. Neurons in the mature DNLL expressed the receptor functionality mediating GluN1 subunit (Figure 28, A). This subunit was expressed in all neurons of the DNLL (Figure 28, A). GluN2A and B appeared to be expressed in most neurons of the DNLL (Figure 28, B, C). The expression of the GluN2C subunit was not as distinct but also present in neurons of the DNLL (Figure 28, D). The GluN2D subunit was weakly expressed but could be unambiguously detected in some of the neurons (Figure 28, E).

Taken together, neurons of the mature DNLL showed a heterogeneous NMDAR subunit composition.

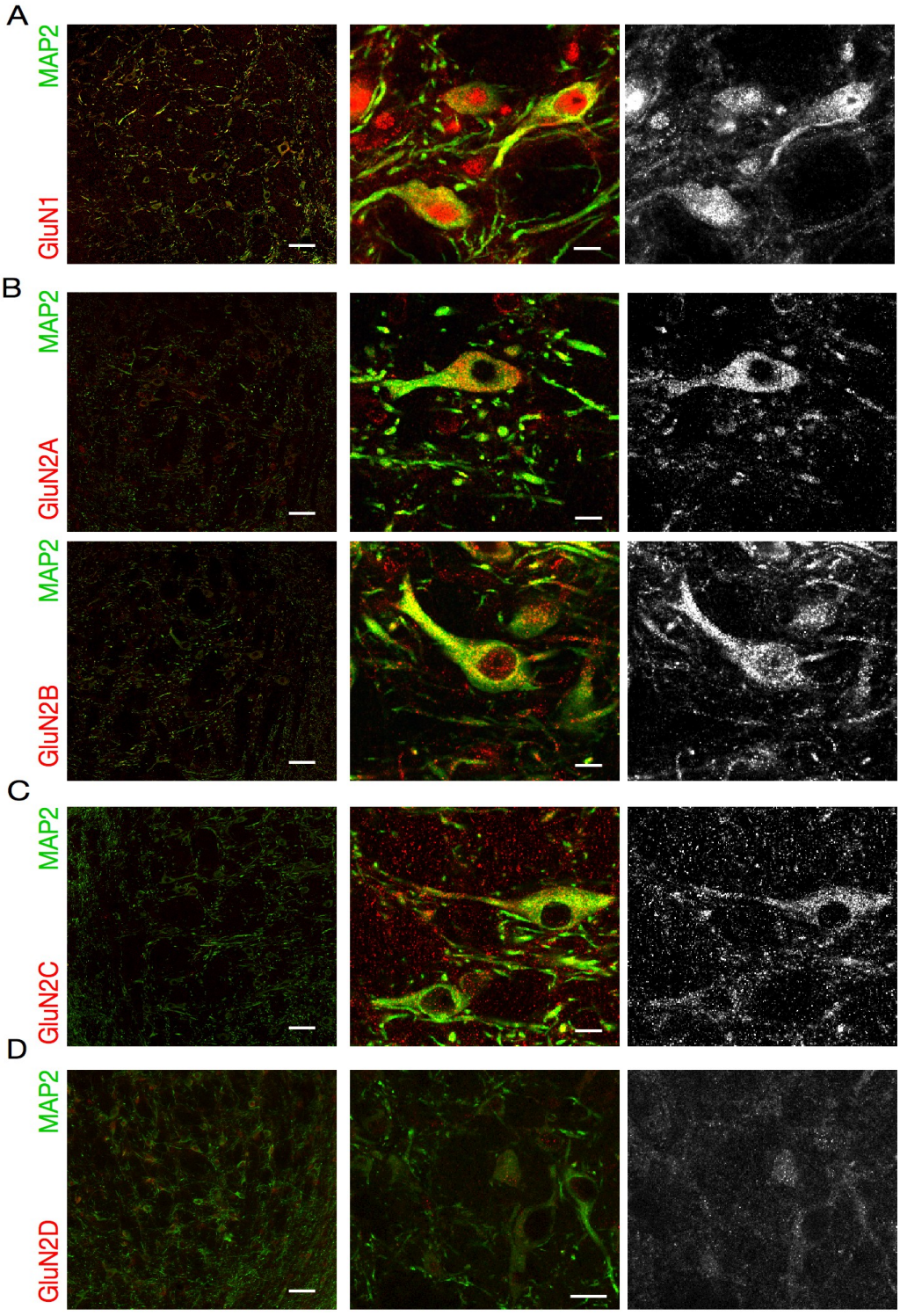

Figure 28: NMDAR expression profile in the mature MSO. A: The NMDAR functionality mediating subunit GluN1 is expressed in all neurons of the DNLL. Its expression spread along the whole neuron. B: Calcium permeability mediating subunit GluN2A is expressed in a subset of DNLL neurons. The expression of GluN2B is similar to that of GluN2A. Both subunits mediate similar calcium permeability. C: GluN2C is expressed in DNLL neurons. D: GluN2D is only expressed by a subset of DNLL neurons.

NMDARs modulate the firing rate of DNLL neurons (Porres et al., 2011). However, how its excitation and inhibition are integrated in a sound level dependent way has

not been investigated yet. To test what the actual influence of sound level is on the firing rate, extracellular *in-vivo* recordings were performed and a persistent inhibition-inducing stimulus was applied (Pecka et al., 2007). For this stimulus protocol, a long pure tone at the best frequency of the neuron was presented on the contralateral ear to excite DNLL neurons. After 50 ms of contralateral excitation an additional short tone, also at best frequency was presented to the ipsilateral ear to evoke persistent inhibition.

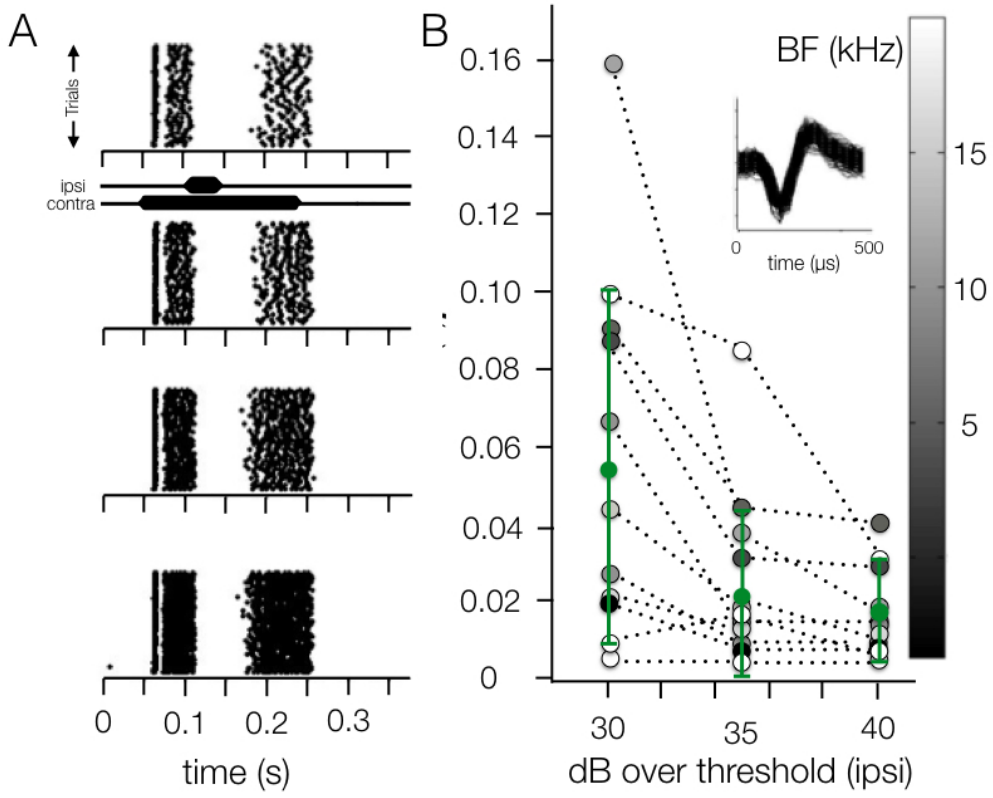

Figure 29: Level dependent changes in length of persistent inhibition for high frequency neurons (> 3 kHz). A: Raster plot of a typical DNLL neuron in response to persistent inhibition stimulus with different levels (contra: 10, ipsi: 30; contra: 15, ipsi: 35; contra: 20, ipsi: 40) but same ILD (20 dB). B: All recorded cells (n = 13) and the calculated length of persistent inhibition. Each circle represents one cell. The grey shade indicates best frequency of the neuron. Inset: Overlay of all recorded APs for the example neuron in A.

As ITDs as well as ILDs are processed in the DNLL high frequency neurons (> 3 kHz) were separated from low frequency neurons (< 3 kHz) during the first analysis to see whether there are differences.

To test whether the overall firing rate of a neuron influences the length of persistent inhibition the stimulus was applied with different sound levels at same ILD. Indeed when changing the levels of the contra- and ipsilateral stimulation the length of inhibition changed dependent on the level (Figure 29, A & B). Lower stimulation intensities lead to lower spike rates and consequently a longer lasting persistent inhibition (Figure 29, A & B). Overall increase of the sound level led to higher firing rates and shorter length of persistent inhibition (Figure 29, A & B). This was the case for 9 out of 10 for low and 12 out of 13 for high frequency neurons (Figure 29 & 30).

In high frequency neurons a contralateral stimulation at best frequency 10 dB over the neurons threshold combined with a 30 dB over threshold ipsilateral stimulation led to a mean inhibition length of 0.056 ± 0.042 s (n = 13; Figure 29, B). Increasing the sound levels to a combination of 20 and 40 dB over threshold decreased the mean length of inhibition to 0.024 ± 0.018 s (Figure 29).

This effect was also present in low frequency neurons (Figure 30) where 10 dB and 30 dB stimulation led to a mean inhibition length of 0.058 ± 0.047 s (n = 10; Figure 29, B). Decreasing the level also decreased persistent inhibition length (20 dB contra, 40 dB ipsi: 0.026 ± 0.025 s). Because of the similarity between high and low frequency neurons the data were pooled during later analysis.

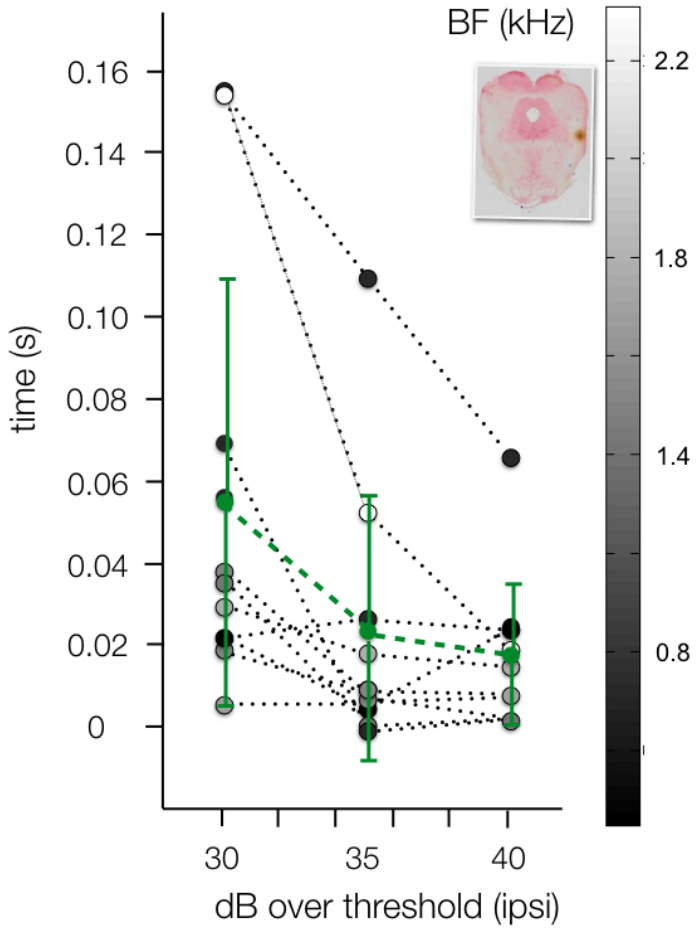

Figure 30: Level dependent changes in length of persistent inhibition for low frequency and thus mainly ITD sensitive neurons (< 3 kHz). A: All recorded cells (n = 10) and the calculated length of persistent inhibition. Each circle represents one cell, green circles indicate mean and SEM. The grey shade indicates best frequency of the neuron. B: HRP labeled recording site.

To get a better impression of the temporal profile of changes in firing rate the cumulative responses for different sound levels were plotted (Figure 31). Here, the AP suppression is indicated as plateau and periods of high firing rates as slope. This again illustrates the decrease in overall firing rate especially after the persistent inhibition (Figure 31). Additionally, the increase in length of inhibition becomes obvious.

Taken together, the length of the inhibition depended on the level and consequently on the overall firing rate of the neuron. The firing rate of DNLL

neurons has been shown to be modulated by NMDARs (Porres et al., 2011). To test whether sound level influences the firing rate and thus controls for the length of inhibition NMDARs were blocked pharmacologically. This was done by iontophoretically applying the NMDAR antagonist AP-5 through a multi-barreled electrode.

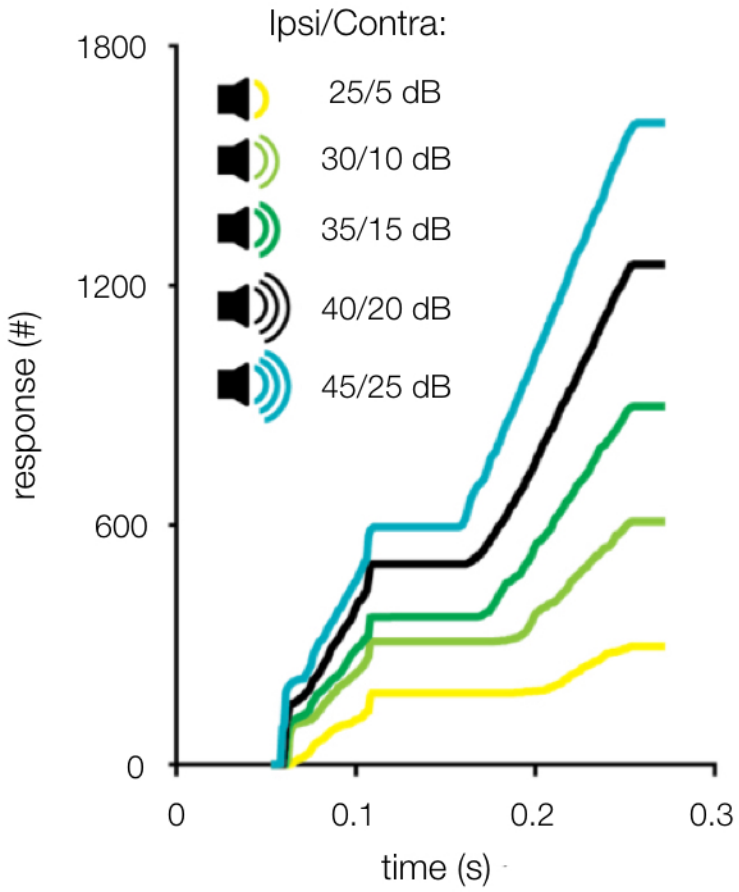

Figure 31: Sound level influences the length of persistent inhibition. Spike number versus time (s) plotted cumulative. Lower sound levels led to longer inhibition times, higher levels to shorter lengths. Different sound level intensities as indicated in graph always at same ILD. CF: 7200 Hz

Blocking NMDAR mediated excitation led to a prolonged persistent inhibition (Figure 32, A & B). The cumulative plot further illustrates the decrease in firing rate especially after the prolonged inhibition in response to ipsilateral stimulation

(Figure 32, C). Blocking NMDARs increased the length of overall AP suppression significantly from 52 ± 9.7 ms to 56 ± 11.2 ms (n = 11; p = 0.006; Figure 32, D).

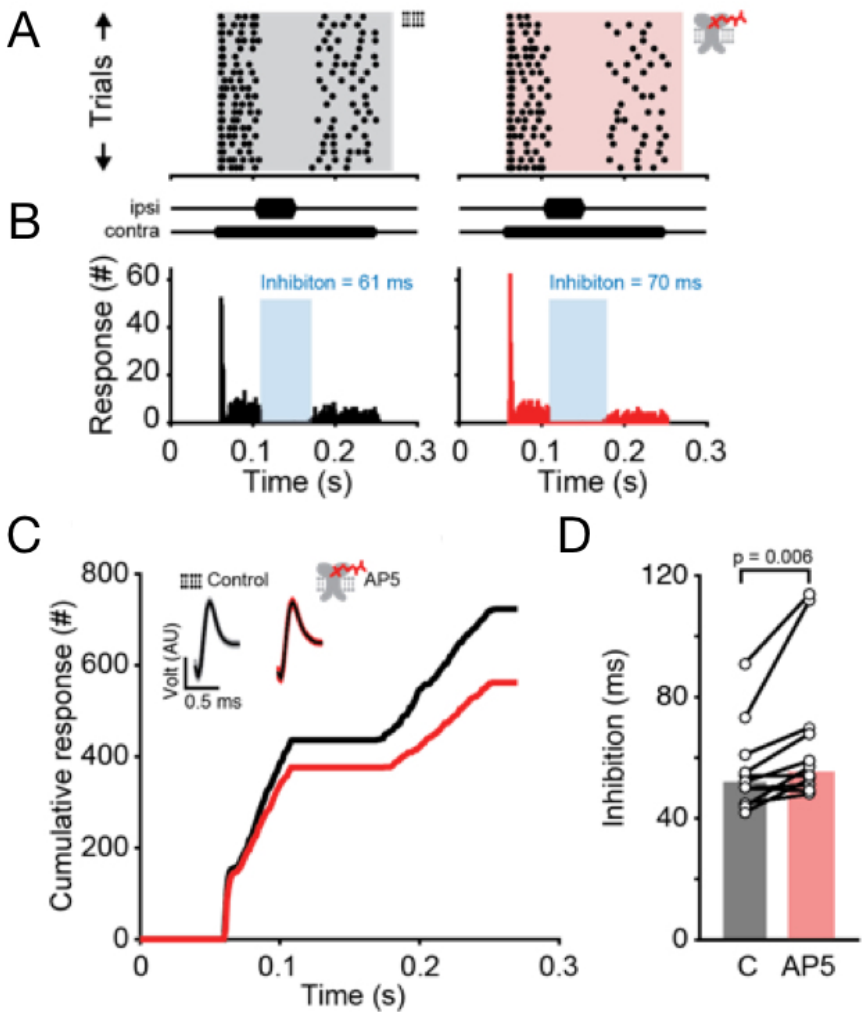

Figure 32: NMDARs increase neuronal excitability in neurons of the DNLL. A & B: stimulation: 200 ms on contralateral ear, after 50 ms followed by a 50 ms ipsilateral tone at BF. Raster plots of 20 trials and PSTHs of a single neuronal response (BF: 2600 Hz) to a binaural stimulus (40 dB ipsilateral and 20 dB contralateral above threshold) before (left) and during application of the NMDA antagonist AP5 (right). C: Cumulative plotted response of the example neuron in A shown before (black) and during AP-5 application (red). In the insets the corresponding extracellularly recorded APs are shown. The mean AP waveform is shown in black and the grey/red lines respectively indicate the standard error for the entire recording session. C: Inhibition duration for each cell (black dots) and the population means (colored bars; n = 11) during control and after NMDAR block. D: Raster plots of 20 trials for a single neuron in response to persistent inhibition stimulus presented with five different sound level combinations with same ILD (increases from top to bottom).

However, this effect could either be specific to NMDAR mediated excitation or depend on the change in firing rate of the postsynaptic neuron. Thus, in the following analysis the effect of sound level and NMDAR effect were quantitatively compared. To do so the persistent inhibition and the preceding first 50 ms firing rate were normalized for both level and NMDAR block experiments (Figure 32). For both datasets a correlation between the relative lengths of inhibition to the normalized firing rate was present (AP5: R = -0.78; p = 0.00001; n = 11; level: R = -0.99; n = 15; p = 0.008). The slopes of the two conditions were also similar (AP5: y = -0.51; level: y = -0.36).

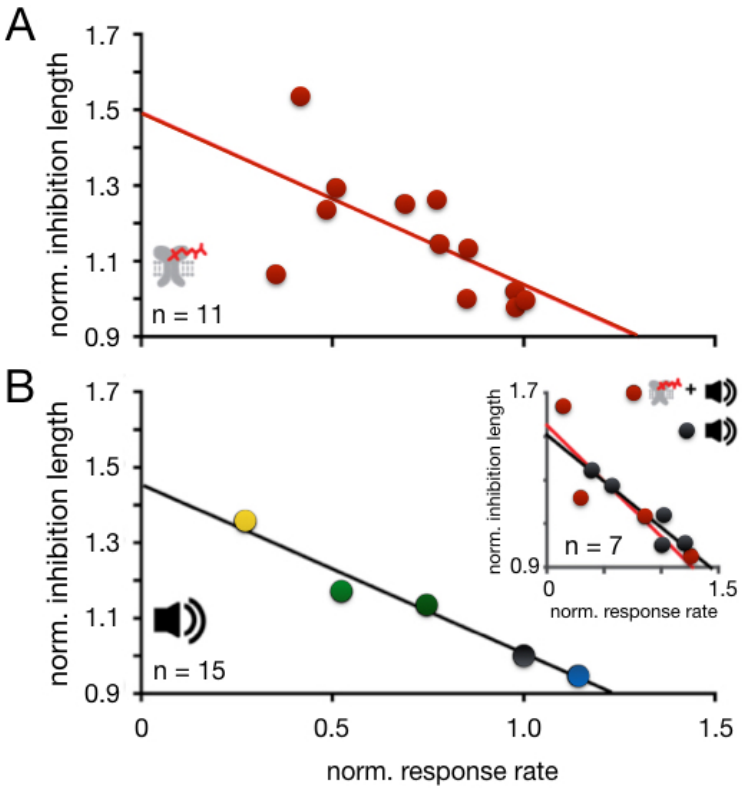

Figure 33: NMDARs and sound level changed the neuronal response rate. Normalized (to 40; 20 dB persistent inhibition stimulus without drug application) values for inhibition and response rate plotted. Each dot represents the mean value of single neuron response (drug experiments) or the population mean for a level condition (sound level experiments). A: Response rate correlated with the duration of inhibition using drug conditions. B: different sound level conditions (yellow, green, grey circles, bottom). In both conditions a correlation between the response and the duration of the inhibition is shown (drugs/top: R = -0,78, p = 0,00001; different levels: R = -0,99, p = 0,008).

Additionally, in a subset of neurons where both conditions were combined (level: R = -0.97, p = 0.0036, y = 0.56; drug and level: R = -0.72, p = 0.16, y = 0.42) showed that level modulates firing rate by NMDARs and thereby influences inhibition length (Figure 33, B; see inset).

Taken together, DNLL neuron response rates could be shown to be dependent on sound level and NMDARs. Higher sound levels recruit more NMDARs that in turn increase the overall firing rate. Thereby the length of inhibition is influenced and thus the echo suppression. This effect could not be influenced by long adaptive stimulation.

4. Discussion

Neurons in the auditory brainstem are anatomically and physiologically specialized to process the fine time scales of acoustic information. However, different nuclei are each very specialized in their structure-function relationships to extract the relevant auditory information from exceedingly subtle cues. In the MSO, for example one of the fastest signal processing in the brain takes place, stressing the need for biophysical specializations towards fast precise computation and output generation. Neurons in the DNLL receive ITD information of the MSO and enhance its information content before sending it to higher structures. The DNLL receives ITD information of the primary sound source and its echo. Thus, it has to differentiate between these two inputs and suppress the information about echolocation. This is achieved by using a inhibitory pathway that is surprisingly slow in comparison to i.e. that used for ITD computation.

4.1 Expression of Potassium channels and implications for function

Low voltage activated potassium channels

MSO neurons have been shown to exhibit many cellular specializations that contribute to maintaining temporal fidelity. In general, the spatial pattern of potassium channel expression influence AP generation, latency, duration and frequency (Brew et al., 1995; Lavine, 1971). In the MSO a varying expression profile along the neuron could show and support the different processing requirements due to its anatomical input organization (Couchman et al., 2012).

The first study revealed that neurons of the mature MSO indeed show a distinct expression profile of LVA channels, HVA channels and channels mediating the A-type current. In the first study the channels Kv1.1, 1.2, and 1.6 were shown to be expressed in the mature MSO (Figure 10 A, B, C). All of these are LVA channels (for review see Gutman et al., 2005), hence they open upon small depolarization from resting potential. Thereby they can regulate AP number and influence AP threshold (for reviews see Gutman et al., 2005, Johnston et al., 2010). Further analysis of their expression profiles along the MSO neuron showed that not all LVA channels have the same expression pattern.

Kv1.1 and Kv1.6 expression is biased towards soma and proximal dendrites (Figure 10 A, C). These findings match earlier studies that showed that more LVA channel currents, presumably Kv1.1 are present at the soma of MSO neurons (Mathews et al., 2010; Scott et al., 2005). This most likely from the soma having a higher density of LVA channels leading to more somatic currents. Kv1.2 in contrast is expressed along the dendrites (Figure 10, B). Especially at the dendrites Kv1.2 activity can prevent EPSP summation and thereby increase the temporal precision of excitatory inputs arriving at the soma.

In the MSO, LVA channels have been shown to play a role during AP repolarization speed (Scott et al., 2005). Additionally, they have been implicated in decreasing somatic AP amplitude (Scott et al., 2005). The high somatic LVA channel density also decreases the input resistance of MSO neurons, as they are partially open at resting membrane potential (Mathews et al., 2010). Thereby they decrease the membrane time constant of MSO neurons at their somata. This short membrane constant in turn enables the fast integration of excitatory with

inhibitory inputs. LVA channels thereby sharpen EPSPs (Mathews et al., 2010; Scott et al., 2005) and have the potential to interact with inhibitory postsynaptic potentials (IPSP; Roberts et al., 2013; Myoga et al., 2014). The anatomical arrangement of inhibition at the soma (Couchman et al., 2010) combined with the soma biased LVA channel expression (Figure 10) further suggests a functional relationship between inhibitory inputs and LVA channels. LVA channels are fast enough to close during the hyperpolarization phase of an IPSP. Thus, the membrane potential moves away from the potassium reversal potential thereby speeding the re-depolarizing phase. In this way LVA channels are able to speed IPSP decay kinetics. This acceleration can promote EPSP peak shifts that play a crucial role for ITD detection (Myoga et al., 2014).

LVA channels could decrease the passive voltage spread at the dendrites and thereby lead to the attenuation of backpropagating APs into the dendrites. Indeed, when LVA channels are blocked the backpropagating AP size increased by about one half (Scott et al., 2007). The remaining AP indicates that LVA channels are most likely not the only reason for the weak regenerative properties of MSO dendrites.

High voltage activated potassium channels

MSO dendrites receive large AMPAR mediated currents (Clark 1969; Couchman et al., 2012; Kil et al., 1995; Smith et al., 1993; Stotler 1953) presumably leading to large EPSPs. At least simulated EPSPs that gradually decrease in their amplitude as they travel to the soma reach amplitudes of up to 70 mV at the very distal dendrite (Mathews et al., 2010). Thus, they most likely

have the potential to open HVA channels (Mathews et al., 2010). Fittingly the expression of HVA channels along the dendrites was found (Figure 11, 12). This is consistent with the fact that in previous studies not all potassium currents were blocked by DTX (Scott et al., 2005) indicating already the presence of other i.e. HVA channels. In the mature MSO Kv2.1, 2.2, 3.1b and 3.2 are expressed (Figure 11, A, B; Figure 12, A, B). These belong to the HVA channel family as they open upon larger depolarization (Gutman et al., 2005). The HVA channels are different in their kinetics as Kv2.1 and 2.2 have relatively slow kinetics while Kv3.1b and 3.2 have faster kinetics (Critz et al., 1993, 1994; Kanemasa et al., 1995; Luneau et al., 1991; for review see Gutman et al., 2005).

In the MSO Kv2.1 and 2.2 are expressed at the soma and dendrites (Figure 11, A, B). Their similar expression profile indicates the presence of heteromeric potassium channels containing both subtypes. This formation is found rarely but does exist (Hwang et al., 1993). Both have slow deactivation kinetics and have been implicated in the modulation of neuronal excitability (Hwang et al., 1992; Kirsch et al., 1993). However, somatically measured AP amplitude is small in the mature gerbil MSO, indicating that Kv2.1 and 2.2 channels are unlikely activated by APs (Scott et al., 2005). They could alternatively play a role in protecting the soma from large depolarization and EPSP summation.

Thus, at the dendrites Kv2.1 and 2.2 expression could prevent EPSP summation, hyperpolarize the inter-stimulus interval and therefore preserve temporal fidelity of incoming inputs to the soma (Tong et al., 2013). They open upon voltages intermediate to that of Kv1 and 3 currents (Gutman et al., 2005).

This study focused on dendritic HVA channel expression, but axonal expression could have an influence on the neuronal discharge pattern. Thereby Kv2.1 and 2.2 have the potential to enhance or substitute for Kv1 and 3 channel functions for example in regulating neuronal excitability. Especially as their activation kinetics differ, a co-expression of these channels would enable MSO neurons to regulate their discharge patterns. The slow deactivation kinetics of Kv2.1 and 2.2 could play a role in increasing refractory period as these channels show prolonged deactivation at negative membrane potentials. Thereby they would slow discharge rates as has been implicated by studies in the hippocampus (Martina et al., 1998).

Kv2.1 has also been shown to play a role in mechanisms of plasticity that dynamically regulate the intrinsic excitability of neurons. Kv2.1 is subjected to rapid activity-dependent, calcineurin-dependent de-phosphorylation. This results in a more hyperpolarized threshold for Kv2.1 current activation (Misonou et al., 2004, 2005, 2006; Mulholland et al., 2008; Murakoshi et al., 1997). Possibly during these phosphorylated states somatic EPSPs and APs in the MSO are able to open Kv2.1 and thereby increase their AP repolarization in periods of high activity. After periods of high activity Kv2.1 phosphorylation and activation thresholds return to rest state (Misonou et al., 2004; Mulholland et al., 2008). Therefore these channels could play a role in dynamically modulating neuronal excitability during periods of high activity in the MSO.

In addition Kv2.1 channels have also been suggested to play a role in regulating somato-dendritic calcium influx (Misonou et al., 2005). This could be achieved by the elimination of a counteracting cation flux balancing calcium entry

to prevent calcium overload and excitotoxicity (Misonou et al., 2005). This might be of particular importance if the described AMPARs at the dendrites show high calcium permeability also in the mature system and would speak for a developmental upregulation of their expression. However, this will have to be further investigated in developmental studies. In addition, the actual influence of Kv2.1 and 2.2 on calcium influx will have to be investigated further in pharmacological *in-vitro* experiments.

Kv3.1b expression is extremely biased towards the soma while Kv3.2 expression is more biased to the soma and proximal dendrites (Figure 12, A, B). In general, Kv3 channels open upon more depolarized potentials (approximately -20 mV) than any other known mammalian Kv channel. Additionally, their currents have extremely fast rates of deactivation upon repolarization that are about an order of magnitude faster than those of any other known Kv channel. These properties indicate open channel instability at voltages around resting potential and propose a role during AP repolarization (Rudy et al., 2001). In nuclei with larger somatic APs than in the MSO they have been shown to be important for high-frequency firing as for example in the MNTB and AVCN (Brew et al., 1995; Song et al., 2005; Weiser et al., 1995; Wang et al., 1998,). Yet, the small somatic APs of MSO neurons are, under normal conditions most likely not able to activate these channels. However, the fast Kv channel kinetics combined with their similar expression profile to Kv1 and Kv2 indicates that these channels most likely interact in regulating neuronal excitability. Still, their exact functional role will have to be elucidated in further pharmacological experiments *in-vitro* and *in-vivo*.

A-type current mediating potassium channels

In addition to LVA and HVA channels, LVA channels mediating the A-type current are expressed in the mature MSO (Figure 13). These open only after prior hyperpolarization and mediate a small, rapidly inactivating A-type current. Their open voltages are the same as for other LVA channels around resting membrane potential. A-type potassium currents have been shown to be present at many stages in the auditory brainstem, as for example type II spiral ganglion neurons (Jagger et al., 2003), a sub-population of type I cells of the VCN (Rothman et al., 2003), lateral olivocochlear neurons of the LSO (Fujino et al., 1997), MNTB (Johnston et al., 2010) and in the DNLL (Fu et al., 1996).

The next part of this study showed that neurons in the MSO express the A-type current mediating channels Kv1.4, 3.3, 4.1 and 4.2 (Figure 13, A, B, C, D) on their soma and dendrites. However, Kv3.3 expression is mainly present at soma and proximal dendrites and does not spread as far into the dendrites as the other A-type channels (Figure 13, B). It is thought that the A-type current is more than half-inactivated at resting membrane potentials (Johnston et al., 2008). Consequently, half of the channels present are still open at resting potential leading to a window current below the activation curve. Therefore A-type channels could contribute to resting conductances making the cell more leaky, without being activated by prior hyperpolarization. Thus, they could still contribute to resting membrane potential.

A-type channels might contribute to AP firing in response to stimulation around voltage threshold, as here EPSPs have a slower time-course and A-type currents could be activated before AP generation. In addition, the A-type current is

largely inactivated during sustained depolarization. But when the preceding membrane potential is hyperpolarized by only -10 mV by a somatic hyperpolarizing IPSP, the A-type current increases two-fold. Then A-type channels could contribute to AP repolarization and most likely sharpen EPSPs (Johnston et al., 2008; Myoga et al., 2014). Thereby A-type channels could speed the decay kinetics of the IPSP and thus play a role in inhibition-enforced EPSP peak shifts as described before for LVA channels (Myoga et al., 2014)

Experimental data from dendritic recordings showed a prominent afterhyperpolarization on the distal dendrites (Callan et al., unpublished; Scott et al., 2007). This afterhyperpolarization could serve as the needed hyperpolarization step to activate A-type channel currents, which in turn might lead to EPSP segregation.

The first step towards understanding the functional role of Kv channels in the mature MSO is to verify their presence and location electrophysiologically. Next, it will be necessary to pharmacologically block the different channels and investigate their effect on synaptic integration and AP properties. Further, one could investigate their influence on ITD coding *in-vivo*. Especially the interaction of LVA channels with inhibition will be an interesting follow-up study *in-vivo*. Finally, the function of HVA channels during periods of high stimulation could be investigated further.

In summary, neurons in the mature MSO express a multitude of Kv channels, including the before shown LVA channels but also different HVA channels and LVA channels mediating the A-type current. Functionally, the expressed LVA channels could be involved in increasing resting conductance and

enabling a faster membrane time constant. LVA channels mediating the A-type current could interact with somatic IPSPs and speed their decay kinetics. Additionally, these LVAs could also contribute to resting conductance making the cell more leaky. The found HVA channels could be implicated in periods of high activity.

Taken together, these channels can have many different functional implications as already described for the MNTB (Brew & Forsythe, 1995; Johnston et al., 2008; Rudy & MacBain, 2001; Wang et al., 1998a for review see: Johnston et al., 2010).

4.2 Development of calcium entry sites

In the MSO the time course of integration of synaptic inputs is determined by neuronal biophysical properties and synaptic input structure (Myoga et al., 2014; Scott et al., 2005; Svirskis et al., 2002). As ITD computation requires the extraction of fine temporal information MSO neurons require not only the appropriate biophysical properties but also the synaptic inputs allowing the transmission of fine temporal information. Thus, this refined circuitry and its integrational properties need to be established during development. This thesis shows that calcium entry sites as well as excitatory synaptic inputs onto MSO neurons refine during late postnatal development (Figures 16 - 20). It further indicates that the main window of refinements is around P13 and that these refinements are activity-dependent. In particular rearing animals in omnidirectional noise did not persistently prevent the development of the refined ITD circuitry.

Refinement in excitatory synaptic inputs

This thesis could show the developmental refinement of excitatory synaptic inputs on the MSO during late postnatal development. Most refinements are calcium dependent (Chen et al., 1998; Greer & Greenberg, 2008). Thus, calcium is a good marker for the investigation of refinement processes. Here, I found that the synaptically mediated EPSCs refine from NMDAR and AMPAR mediated to almost exclusively AMPAR mediated EPSCs. This refinement happens in parallel with a decrease in overall synaptically mediated calcium influx. This decrease in calcium influx is mainly based on the strong decrease in NMDAR mediated calcium influx. Additionally, this study could show that the AMPAR charge time constant decreased together with its mediated calcium influx. Also the AMPAR single fiber size as well as its quantal content increased during late postnatal development.

The found increase in AMPAR kinetics could be based on changes in their subunit composition. AMPARs containing mostly GluR4 and only little GluR2 have the fastest channel kinetics (Geiger et al., 1995; Mosbacher et al., 1994). These channels are ideal to generate the fast time constants. The presence of AMPARs containing the GluR2 subunit can be verified electrophysiologically by measuring the rectification of their EPSCs (Bowie et al., 1995, Kamboj et al., 1995, Koh et al., 1995). The here found AMPAR rectification was only slightly higher at P60 – 90, indicating a reduced GluR2 expression compared to P13. Also in immunohistochemical staining GluR2 expression appeared higher at P13 than at P60-90. Overall AMPARs in the MSO showed relatively strong rectification indicating that only little GluR2 is expressed at both ages. The finding that GluR2 expression is rather low seems to contradict the here found decrease in calcium

influx during development. However, this decrease in calcium influx could also be due to the decrease in AMPAR charge decay time constant and the strong decrease in NMDAR mediated calcium influx. To further elucidate the GluR2 role one should test whether and how much in comparison to P13 and P60 – 90 GluR2 is expressed at P10 – P11. If expression levels are also similar to those found at P13 the decrease in calcium influx is mainly due to the decrease in charge decay time constant and loss of NMDAR mediated calcium influx.

Around P17 EPSCs and calcium influx are mainly evoked by AMPARs and only little by NMDARs (Figure 16, 18, 19, 20). At P60-90 NMDARs could not be measured electrophysiologically anymore. Preliminary tests showed that NMDARs could be activated only under intense stimulation close to the dendrite NMDARs could be activated (data not shown) but this form of stimulation was not physiologically realistic and usually resulted in cell death. NMDAR presence during maturity could also be verified immunohistochemically. At P13 NMDARs are comprised mainly of the GluN2A and GluN1 subunits, which are expressed at soma and mainly proximal dendrites of the MSO. GluN1 expression mediates NMDAR functionality (Furukawa et al., 2005). During development the expression of GluN1 and GluN2A persists while GluN2B expression is upregulated. The GluN2A and GluN2B subunit have been shown to be highly calcium permeable and are more sensitive to the magnesium block than GluN2C and GluND (Monyer et al., 1994).

Therefore, functional NMDARs are expressed in the developing and mature system but under normal circumstances they are only in some cases synaptically activated anymore in maturity (Figure 19, 20, 22; Couchman et al., 2012). In the

mature MSO NMDARs together with nitric oxide activation could be involved in calcium signaling and thereby alter synaptic transmission and postsynaptic excitability (Steinert et al., 2008; 2010). Also NMDARs in the mature MSO seem to be expressed mainly extrasynaptically (Couchman et al., 2012). This is especially true for GluN2Bs (for review see Blanke & van Dongen, 2009), which fits their developmental upregulation in expression. Thus, they are most likely activated only during periods of high activity. Thereby NMDAR activation could increase the leak conductance, decreasing the membrane time constant and shortening time windows for coincidence detection. NMDARs could slow the overall speed of excitation as it provides slow, summating responses. Thus, NMDARs could compensate for the relatively fast AMPAR kinetics and dynamically modulate timing and tune coincidence detection windows for ITD coding. As NMDARs require glycine binding for their activation, already ambient glycine concentrations may release the magnesium block and allow calcium influx and receptor activation (for review see Blanke & van Dongen, 2009). In addition, has synaptic glycine been shown to potentiate somatic NMDARs (Couchman et al., 2013).

Thereby, NMDARs could raise the membrane potential and enable a plateau potential to prevent IPSP summation and strong hyperpolarization. In this way precise synaptic integration towards ITD computation would remain possible also with many inhibitory inputs arriving at the soma. However, to elucidate the importance of NMDARs for ITD processing their function will have to be investigated *in-vivo* in relation to ITD curve tuning. This could be done by stimulating the cells at maximal firing rate, as well as with high inhibition rates with

and without blocking NMDARs pharmacologically. Then one could investigate their role on ITD coding.

AMPARs and NMDARs remain highly calcium permeable also at mature stages. This persistence of AMPAR and NMDAR calcium permeability could be necessary to enable the activation of Ca^{2+}-sensitive ion channels and the activation of second messenger systems. More generally, the presence of calcium-permeable glutamate channels could enable rapid control of extracellular Ca^{2+} concentration in the synaptic cleft (Jahr & Stevens, 1993; Otis et al., 1995).

Taken together, refinements in AMPAR single fiber size, quantal content, as well as its decay time constants and peak currents happen in a period of high calcium influx and high NMDAR current prevalence. After this period of refinements, around P14, NMDAR currents and their mediated calcium influx decrease rapidly.

Plasticity window

Interestingly, the NMDAR mediated calcium influx peaked around P13. As NMDAR currents together with a postsynaptic increase in calcium are central for neuronal plasticity (Malenka et al., 2004), this indicates a period of high plasticity around P13. Indeed, subsequently the overall calcium influx as well as NMDAR mediated calcium influx decrease quickly. Also the synaptic currents refine during this period. Around P11 to 13 most of the currents and charge are mediated by NMDARs. These then change until at P17 most currents are AMPAR mediated.

These findings support the hypothesis that around P13 excitatory transmission is refined by plasticity mechanisms involving NMDAR currents and

synaptically mediated calcium influx. Indeed also the AMPAR quantal content increases from P14 to P17. Gerbils have been shown to have adult-like hearing around P13 - 14 but still with elevated level thresholds and ITD curves not properly adjusted (McFadden et al., 1996; Seidl & Grothe, 2005). These refine only at P15 - 30 (McFadden et al., 1996; Seidl & Grothe, 2005). Thus, a period for high NMDAR and calcium activity around P13 could be involved in this late refinement phase from P15 to 30 when hearing matures. During this period electrical properties as well as synaptic time constants of gerbil MSO neurons mature (Magnusson et al., 2005; Scott et al., 2005; Svirskis et al., 2002, 2004). Also the glycinergic inhibition pattern refines from somatic and dendritic to somatic projection in an experience-dependent way (Werthat et al., 2008). The shift of ITDs into the physiologically relevant has been shown to be experience-dependent (Seidl & Grothe, 2005).

Activity-dependency of refinements

Next, I aimed to investigate whether the found refinements in excitatory inputs depend on experience. Towards this aim, animals were raised in omnidirectional noise from P9 until P14 or 17. By masking most low-frequency sounds with white noise, experience-dependent processes should show deficits. Omnidirectional white noise is a source of a high binaural activity but in an uncorrelated manner. This temporal profile of inputs has been shown to be necessary for the refinement of inhibitory inputs to the soma of mature MSO neurons and ITD tuning during late postnatal development (Kapfer et al., 2002; Seidl & Grothe, 2005; Werthat et al., 2008).

This study showed that the refinement of excitatory inputs was mostly independent of experience as it developed also in omnidirectional noise. The late postnatal refinement to fast AMPAR currents from AMPAR and NMDAR currents was not persistently altered by omnidirectional noise. However, AMPAR peak currents were larger in omnidirectional noise. This could be due to the higher activity or hint at a slight experience-dependency of this refinement.

The overall calcium permeability of the AMPARs and NMDARs present indicated a faster maturation of the inputs. At P14 the overall calcium influx was already at levels of P17 control animals. This faster decrease in calcium permeability seemed to be based on a faster developmental change in NMDAR subunit composition. This hypothesis is based on the finding that NMDAR EPSCs were not significantly changed but their synaptically mediated calcium influx. The calcium impermeability mediating GluR2 subunit is expressed at P13 and P60 – 90 in control conditions. In parallel to the AMPAR mediated calcium influx, its decay time constant decreased independent of experience. Taken together, the found decrease in AMPAR mediated calcium influx is most likely based on the decrease of its decay time constant that might be based on a different expression of GluR2. This change in GluR2 expression would then be independent of experience and most likely also activity-independent. For further verification though the GluR2 expression profile for the different developmental stages in control and omnidirectional noise conditions will have to be investigated.

The developmental increase in quantal content was found to be mostly independent of experience. Omnidirectional white noise exposure led to a faster increase in single input size and quantal content. At P14 it was about the size of

P17 control synapses. This faster maturation indicated an activity-dependency as by P17 the quantal content was not different from control conditions anymore.

In summary, refinement of AMPAR and NMDAR EPSCs was independent of experience. As these did not show any changes in their refinement in response to high activity they could also be independent of activity. In contrast, the refinement in calcium permeability and quantal content could be hypothesized to be activity-dependent as the high activity in omnidirectional noise increased the speed of their maturation.

Studies mainly on the visual system indicate that for the emergence of mature circuit connectivity correlated activity among synaptic afferents is required (Goodhill et al., 1995; Miller et al., 1989; Shatz, 1990b). This can either be spontaneous or sensory-evoked activity and has to be coupled with the ability of the postsynaptic neuron to correlate this patterned activity, for example by the presence of NMDARs.

In this study, exposing the developing system to omnidirectional white noise lead to a subtle increase in maturation speed for NMDAR calcium permeability and single fiber size. Thus, it can be hypothesized that sensory evoked activity is at least partially involved in the refinement of these excitatory input properties. Also the high prevalence of NMDARs and calcium permeability around P13 supports this hypothesis as they form the classical basis for LTP induction (for reviews see Malenka et al; 2004; Bear & Malenka, 1993; Bear & Abraham, 1996; Malenka & Nicoll, 1993). Thus, a possible mechanism for the excitatory input refinements from AMPAR and NMDAR currents to AMPAR, synaptic strengthening and changes in subunit composition could be LTP

induction. Therefore NMDARs would function as coincidence detectors of pre- and postsynaptic activity leading to synaptic strengthening as suggested by the results of this study.

However, especially for the refinement from AMPAR and NMDAR mediated EPSCs to mainly AMPAR EPSPCs, mEPSC size and maybe also AMPAR calcium permeability a role of spontaneous activity cannot be ruled. It has been shown that spontaneous activity is generated by transmitter release in the inner ear and activates auditory nerve fibers already before hearing onset (Beutner et al., 2001; Glowatzki et al., 2002; Johnson et al., 2011; Tritsch et al., 2007, 2010). It is more likely though that this spontaneous activity is more important for crude circuit formation, as has been shown already (Kandler & Friauf, 1993; Person et al., 2004; Kil et al., 1995; Sanes & Takacs, 1993), and later refinements are guided by sensory evoked activity. This would also explain the temporal profile of the found refinement processes as they happen after hearing onset. Additionally, some of these refinements show faster maturation when the MSO inputs are driven binaurally at high rates but temporally uncorrelated.

Summary development of calcium entry sites

To summarize, excitatory and inhibitory inputs refine between P10/11 and P16/17 leaving the system with precisely arranged and timed inputs which facilitate precise ITD computation (Chirila et al., 2007; Kapfer et al., 2002; Werthat et al., 2008). Thus, input refinement occurs mainly during the transition phase when the audible spectrum becomes adult-like and lasts until the early refinement phase when hearing thresholds mature (McFadden et al., 1996). This time window

is relatively small, as already at P15 physiological mechanisms supporting ITD processing have been shown to be in place. This is in accord with the findings of this study showing that most refinements happen until P14 and are almost finished by P17. However, the processes by which excitation and inhibition refine seem to differ as excitatory inputs refine in a relatively stable most likely activity-dependent manner while inhibitory input relocation depends on experience (Kapfer et al., 2002; Werthat et al., 2008). On the circuit level and especially towards physiological functioning this seems to make sense, as the excitatory inputs only provide a course estimation of sound location. When combined with precisely timed inhibition the peak of the ITD curve shifts into the physiologically relevant range (Brand et al., 2001; Pecka et al., 2010, Myoga et al., 2014). Thus, excitatory inputs seem to refine through acoustic activity *per se* while the refinement of inhibitory inputs needs precisely timed inputs to counterbalance the excitation and thereby fine-tune ITD curves. When excitation and inhibition refine in different ways it could also be that these processes rely on different plasticity mechanisms. While LTP could be the mechanism for excitatory refinements, STDP could be involved in the refinement of inhibition as it takes the relative timing of the incoming inputs into account and has already been proposed to be the mechanism present in the MSO (Leibold & van der Hemmen, 2005).

However, the exact mechanism by which excitatory inputs refine has not been elucidated. Further experiments will have to focus on P13 to study the involved plasticity mechanisms. The first experiments could be done *in-vitro* with different long-term plasticity protocols, testing for the plasticity rule. When this is found the underlying molecular mechanisms could be investigated.

4.3 Binaural processing in the DNLL

The main physiological hallmark of the DNLL is the persistent inhibition of APs by the contralateral DNLL after an ipsilateral stimulus. In the last study the functional role of NMDARs for echo suppression in the mature DNLL was investigated. Immunohistochemistry revealed the presence of GluN2A/ B and GluN2C/ D (Figure 27, B, C). The latter lead to NMDARs with low magnesium sensitivity that enables their opening below AP threshold. From *in-vivo* experiments it follows that NMDARs contribute to a sound intensity dependent adjustment of this persistent inhibition mediated by GABA receptors. Earlier studies already described the presence of NMDAR currents in the mature DNLL and suggested that they play a role in amplifying postsynaptic firing rate (Ammer et al., 2012; Fu et al., 1997; Porres et al., 2011; Wu et al., 1995). It has been shown that they also have the potential to counterbalance the strongly depressing AMPAR currents present in the DNLL (Porres et al., 2011). Consequently, in the mature DNLL NMDARs play a critical role in enabling high firing rates in response to ongoing activity. As mentioned above the presence of GluN2C and D with their low magnesium sensitivity could form the basis for these sustained high firing rates. The slow decay kinetics of NMDARs contribute a counterpart to the fast AMPAR currents also described in that study (Siveke et al., unpublished). These slow decay kinetics again are a property of the GluN2C and D subunit mediated NMDAR currents. Thus, the present NMDARs enables a slow sub-threshold NMDAR signaling that can counterbalance the synaptic depression of fast AMPARs. Thereby the depolarization level can be kept close to threshold, which allows the fast AMPARs to still elicit APs with high temporal fidelity.

In this way NMDARs can also influence the length of persistent inhibition by keeping the overall firing rate high. Persistent inhibition has been implicated in echo suppression but so far the neuronal mechanisms for echo suppression are still unclear and debated (Brown et al., 2015). The last study supports the role of persistent inhibition on echo suppression in the DNLL, as this persistent suppression of firing rate can now also explain a specific psychophysical behavior of echo suppression. By modulating the sound intensity it could be shown that sound intensity controls the length of persistent inhibition. This together with the finding that human listeners adjust their echo perception dependent on sound intensities (Siveke et al, unpublished) shows that the duration of sound information suppression can be explained by the duration of reciprocal inhibition in the DNLL. The basis for this echo suppression is persistent inhibition that is adjusted by NMDAR currents. However, these findings do not exclude a role of peripheral mechanisms on the level of the cochlea (Bianchi et al., 2013) or other central circuits in the precedence effect (Brown et al., 2015).

In this thesis it could be shown that sound pressure influenced the length of persistent inhibition in that higher levels lead to shorter inhibition times via NMDAR activation. Functionally this level dependence of the inhibition and thus echo suppression could be a mechanism for sound distance dependent filtering. In this case the overall level of the first stimulus and the lagging echo would represent sound source distance. Then louder stimulations would represent sound sources that are closer than fainter ones. Thereby listeners would be equipped with the ability to more rapidly detect the distance of spatial cues enabling faster reaction times to sound sources nearby.

References

Abbott LF, Nelson SB Synaptic plasticity: taming the beast. Nat Neurosci.

Adams JC, Mugnaini E (1984) Dorsal nucleus of the lateral lemniscus: a nucleus of GABAergic projection neurons. Brain Res Bull 13:585-590.

Aitkin LM, Martin RL (1987) The representation of stimulus azimuth by high best-frequency azimuth-selective neurons in the central nucleus of the inferior colliculus of the cat. J Neurophysiol 57:1185-1200.

Ammer JJ, Grothe B, Felmy F (2012) Late postnatal development of intrinsic and synaptic properties promotes fast and precise signaling in the dorsal nucleus of the lateral lemniscus. Journal of Neurophysiology 107:1172-1185.

Ammer JJ, Siveke I, Felmy F Activity-Dependent Transmission and Integration Control the Timescales of Auditory Processing at an Inhibitory Synapse. Current Biology 25:1562-1572.

Beutner D, Moser T (2001) The Presynaptic Function of Mouse Cochlear Inner Hair Cells during Development of Hearing. The Journal of Neuroscience 21:4593-4599.

Bianchi F, Verhulst S, Dau T (2013) Experimental evidence for a cochlear source of the precedence effect. Journal of the Association for Research in Otolaryngology: JARO 14:767-779.

Blanke ML, VanDongen AMJ (2009) Biology of the NMDA Receptor. CRC Press/Taylor & Francis

Bliss TV, Lomo T (1973) Long-lasting potentiation of synaptic transmission in the dentate area of the anaesthetized rabbit following stimulation of the perforant path. J Physiol 232:331-356.

Boudreau JC, Tsuchitani C (1968) Binaural interaction in the cat superior olive S segment. J Neurophysiol 31:442-454.

Boulter J, Hollmann M, O'Shea-Greenfield A, Hartley M, Deneris E, Maron C, Heinemann S (1990) Molecular cloning and functional expression of glutamate receptor subunit genes. Science 249:1033-1037.

Bowie D, Mayer ML (1995) Inward rectification of both AMPA and kainate subtype glutamate receptors generated by polyamine-mediated ion channel block. Neuron 15:453-462.

Brand A, Behrend O, Marquardt T, McAlpine D, Grothe B (2002) Precise inhibition is essential for microsecond interaural time difference coding. Nature 417:543-547.

Brew HM, Forsythe ID (1995) Two voltage-dependent K+ conductances with complementary functions in postsynaptic integration at a central auditory synapse. J Neurosci 15:8011-8022.

Brown AD, Jones HG, Kan A, Thakkar T, Stecker GC, Goupell MJ, Litovsky RY (2015) Evidence for a neural source of the precedence effect in sound localization. J Neurophysiol 114:2991-3001.

Brugge JF, Anderson DJ, Aitkin LM (1970) Responses of neurons in the dorsal nucleus of the lateral lemniscus of cat to binaural tonal stimulation. J Neurophysiol 33:441-458.

Burger RM, Pollak GD (2001) Reversible inactivation of the dorsal nucleus of the lateral lemniscus reveals its role in the processing of multiple sound sources in the inferior colliculus of bats. J Neurosci 21:4830-4843.

Burnashev N, Monyer H, Seeburg PH & Sakmann B (1992) Divalent ion permeability of AMPA receptor channels is dominated by the edited form of a single subunit. Neuron 8: 189-98

Cathala L, Brickley S, Cull-Candy S, Farrant M (2003) Maturation of EPSCs and intrinsic membrane properties enhances precision at a cerebellar synapse. J Neurosci 23:6074-6085.

Chen L, Kelly JB, Wu SH (1999) The commissure of probst as a source of GABAergic inhibition. Hear Res 138:106-114.

Chirila FV, Rowland KC, Thompson JM, Spirou GA (2007) Development of gerbil medial superior olive: integration of temporally delayed excitation and inhibition at physiological temperature. J Physiol 584:167-190.

Clark GM (1969) The ultrastructure of nerve endings in the medial superior olive of the cat. Brain Res 14:293-305.

Connor JA, Stevens CF (1971) Prediction of repetitive firing behaviour from voltage clamp data on an isolated neurone soma. J Physiol 213:31-53.

Couchman K, Grothe B, Felmy F (2010) Medial superior olivary neurons receive surprisingly few excitatory and inhibitory inputs with balanced strength and short-term dynamics. J Neurosci 30:17111-17121.

Couchman K, Grothe B, Felmy F (2012) Functional localization of neurotransmitter receptors and synaptic inputs to mature neurons of the medial superior olive. Journal of Neurophysiology 107:1186-1198.

Cramer KS, Gabriele ML (2014) Axon Guidance in the Auditory System: Multiple Functions of Eph Receptors. Neuroscience 0:152-162.

Chen HJ, Rojas-Soto M, Oguni A and Kennedy MB (1998) A synaptic Ras-GTPase activating protein (p135SynGAP) inhibited by CaM kinase II. Neuron 20:895-904

Critz SD, Wible BA, Lopez HS, Brown AM (1993) Stable expression and regulation of a rat brain K+ channel. J Neurochem 60:1175-1178.

Debanne D, Poo MM (2010) Spike-timing dependent plasticity beyond synapse - pre- and post-synaptic plasticity of intrinsic neuronal excitability. Front Synaptic Neurosci 2:21.

Diamond JS, Copenhagen DR (1993) The contribution of NMDA and non-NMDA receptors to the light-evoked input-output characteristics of retinal ganglion cells. Neuron 11:725-738.

Dingledine R, Borges K, Bowie D & Traynelis S (1999) The glutamate receptor ion channels. Pharmacological reviews 51, 7-61.

Dodson PD, Barker MC, Forsythe ID (2002) Two heteromeric Kv1 potassium channels differentially regulate action potential firing. J Neurosc 22: 6953-61.

Fischer I, Shea TB, Sapirstein VS, Kosik KS (1986) Expression and distribution of microtubule-associated protein 2 (MAP2) in neuroblastoma and primary neuronal cells. Brain Res 390:99-109.

Ford MC, Grothe B, Klug A (2009) Fenestration of the calyx of Held occurs sequentially along the tonotopic axis, is influenced by afferent activity, and facilitates glutamate clearance. J Comp Neurol 514:92-106.

Forsythe ID, Westbrook GL (1988) Slow excitatory postsynaptic currents mediated by N-methyl-D-aspartate receptors on cultured mouse central neurones. J Physiol 396:515-533.

Franks KM, Isaacson JS (2005) Synapse-specific downregulation of NMDA receptors by early experience: a critical period for plasticity of sensory input to olfactory cortex. Neuron 47:101-114.

Franzen DL, Gleiss SA, Berger C, Kümpfbeck FS, Ammer JJ, Felmy F (2015) Development and modulation of intrinsic membrane properties control the temporal precision of auditory brain stem neurons. Journal of Neurophysiology 113:524-536.

Friauf E, Lohmann C (1999) Development of auditory brainstem circuitry. Activity-dependent and activity-independent processes. Cell Tissue Res 297:187-195.

Fu XW, Brezden BL, Kelly JB, Wu SH (1997) Synaptic excitation in the dorsal nucleus of the lateral lemniscus: whole-cell patch-clamp recordings from rat brain slice. Neuroscience 78:815-827.

Fu XW, Wu SH, Brezden BL, Kelly JB (1996) Potassium currents and membrane excitability of neurons in the rat's dorsal nucleus of the lateral lemniscus. J Neurophysiol 76:1121-1132.

Fujino K, Koyano K, Ohmori H (1997) Lateral and medial olivocochlear neurons have distinct electrophysiological properties in the rat brain slice. J Neurophysiol 77:2788-2804.

Furukawa H, Singh SK, Mancusso R, Gouaux E (2005) Subunit arrangement and function in NMDA receptors. Nature 438:185-192.

Futai K, Okada M, Matsuyama K, Takahashi T (2001) High-Fidelity Transmission Acquired via a Developmental Decrease in NMDA Receptor Expression at an Auditory Synapse. The Journal of Neuroscience 21:3342-3349.

Geiger JR, Melcher T, Koh DS, Sakmann B, Seeburg PH, Jonas P, Monyer H (1995) Relative abundance of subunit mRNAs determines gating and Ca2+ permeability of AMPA receptors in principal neurons and interneurons in rat CNS. Neuron 15:193-204.

Gittelman JX, Tempel BL (2006) Kv1.1-containing channels re critical for temporal precision during spike initiation. J Neurophysiol 96: 1203-14.

Glendenning KK, Brusno-Bechtold JK, Thompson GC, Masterton RB (1981) Ascending auditory afferents to the nuclei of the lateral leminscus. The Journal of Comparative Neurology 197:673-703.

Glowatzki E, Fuchs PA (2002) Transmitter release at the hair cell ribbon synapse. Nat Neurosci 5:147-154.

Golding NL, Oertel D (2012) Synaptic integration in dendrites: exceptional need for speed. J Physiol 590:5563-5569.

Goodhill GJ, Lowel S (1995) Theory meets experiment: correlated neural activity helps determine ocular dominance column periodicity. Trends Neurosci 18:437-439.

Greger IH, Khatri L, Ziff EB (2002) RNA editing at arg607 controls AMPA receptor exit from the endoplasmic reticulum. Neuron 34:759-772.

Grothe B (2003) New roles for synaptic inhibition in sound localization. Nat Rev Neurosci 4:540-550.

Grothe B, Pecka M (2014) The natural history of sound localization in mammals--a story of neuronal inhibition. Front Neural Circuits 8:116.

Grothe B, Pecka M, McAlpine D (2010) Mechanisms of Sound Localization in Mammals. Physiological Reviews 90:983-1012.

Gutman GA, Chandy KG, Grissmer S, Lazdunski M, McKinnon D, Pardo LA, Robertson GA, Rudy B, Sanguinetti MC, Stuhmer W, Wang X (2005) International Union of Pharmacology. LIII. Nomenclature and molecular relationships of voltage-gated potassium channels. Pharmacol Rev 57:473-508.

Hestrin S (1993) Different glutamate receptor channels mediate fast excitatory synaptic currents in inhibitory and excitatory cortical neurons. Neuron 11:1083-1091.

Hollmann M, Heinemann S (1994) Cloned glutamate receptors. Annu Rev Neurosc 17:31-108

Howell DM, Morgan WJ, Jarjour AA, Spirou GA, Berrebi AS, Kennedy TE, Mathers PH (2007) Molecular guidance cues necessary for axon pathfinding from the ventral cochlear nucleus. The Journal of Comparative Neurology 504:533-549.

Hwang PM, Fotuhi M, Bredt DS, Cunningham AM, Snyder SH (1993) Contrasting immunohistochemical localizations in rat brain of two novel K+ channels of the Shab subfamily. J Neurosci 13:1569-1576.

Hwang PM, Glatt CE, Bredt DS, Yellen G, Snyder SH (1992) A novel K+ channel with unique localizations in mammalian brain: molecular cloning and characterization. Neuron 8:473-481.

Jagger DJ, Housley GD (2003) Membrane properties of type II spiral ganglion neurones identified in a neonatal rat cochlear slice. J Physiol 552:525-533.

Jahr CE, Stevens CF (1993) Calcium permeability of the N-methyl-D-aspartate receptor channel in hippocampal neurons in culture. Proc. Nat. Acad. Sci. 90: 11573-77

Jiao S, Liu Z, Ren WH, Ding Y, Zhang YQ, Zhang ZH, Mei YA (2007) cAMP/protein kinase A signalling pathway protects against neuronal apoptosis and is associated with modulation of Kv2.1 in cerebellar granule cells. J Neurochem 100:979-991.

Johnson SL, Eckrich T, Kuhn S, Zampini V, Franz C, Ranatunga KM, Roberts TP, Masetto S, Knipper M, Kros CJ, Marcotti W (2011) Position-dependent patterning of spontaneous action potentials in immature cochlear inner hair cells. Nat Neurosci 14:711-717.

Johnston D, Christie BR, Frick A, Gray R, Hoffman DA, Schexnayder LK, Watanabe S, Yuan LL (2003) Active dendrites, potassium channels and synaptic plasticity. Philos Trans R Soc Lond B Biol Sci 358:667-674.

Johnston J, Forsythe ID, Kopp-Scheinpflug C (2010) Going native: voltage-gated potassium channels controlling neuronal excitability. J Physiol 588:3187-3200.

Johnston J, Griffin SJ, Baker C, Forsythe ID (2008) Kv4 (A-type) potassium currents in the mouse medial nucleus of the trapezoid body. Eur J Neurosci 27:1391-1399.

Jonas P, Racca C, Sakmann B, Seeburg PH, Monyer H (1994) Differences in Ca2+ permeability of AMPA-type glutamate receptor channels in neocortical neurons caused by differential GluR-B subunit expression. Neuron 12:1281-1289.

Kamboj SK, Swanson GT, Cull-Candy SG (1995) Intracellular spermine confers rectification on rat calcium-permeable AMPA and kainate receptors. J Physiol 486 (Pt 2):297-303.

Kandler K, Friauf E (1993) Pre- and postnatal development of efferent connections of the cochlear nucleus in the rat. The Journal of Comparative Neurology 328:161-184.

Kandler K, Friauf E (1995) Development of glycinergic and glutamatergic synaptic transmission in the auditory brainstem of perinatal rats. J Neurosci 15:6890-6904.

Kanemasa T, Gan L, Perney TM, Wang LY, Kaczmarek LK (1995) Electrophysiological and pharmacological characterization of a mammalian Shaw channel expressed in NIH 3T3 fibroblasts. J Neurophysiol 74:207-217.

Kapfer C, Seidl AH, Schweizer H, Grothe B (2002) Experience-dependent refinement of inhibitory inputs to auditory coincidence-detector neurons. Nat Neurosci 5:247-253.

Kelly JB, Buckthought AD, Kidd SA (1998) Monaural and binaural response properties of single neurons in the rat's dorsal nucleus of the lateral lemniscus. Hear Res 122:25-40.

Kelly JB, Kidd SA (2000) NMDA and AMPA Receptors in the Dorsal Nucleus of the Lateral Lemniscus Shape Binaural Responses in Rat Inferior Colliculus. Journal of Neurophysiology 83:1403-1414.

Kelly JB, van Adel BA, Ito M (2009) Anatomical projections of the nuclei of the lateral lemniscus in the albino rat (Rattus norvegicus). J Comp Neurol 512:573-593.

Khurana S, Remme MW, Rinzel J, Golding NL (2011) Dynamic interaction of Ih and IK-LVA during trains of synaptic potentials in principal neurons of the medial superior olive. J Neurosc 24: 8936-8947

Kirsch GE, Shieh CC, Drewe JA, Vener DF, Brown AM (1993) Segmental exchanges define 4-aminopyridine binding and the inner mouth of K+ pores. Neuron 11:503-512.

Kleinschmidt A, Bear MF, Singer W (1987) Blockade of "NMDA" receptors disrupts experience-dependent plasticity of kitten striate cortex. Science 238:355-358.

König N, Poluch S, Estabel J, Durand M, Drian, M.-J., Exbravat J.-M. (2001) Synaptic and non-synaptic AMPA receptors permeable to calcium. Japan J of pharm 86: 1-17

Koh DS, Geiger JR, Jonas P, Sakmann B (1995) Ca(2+)-permeable AMPA and NMDA receptor channels in basket cells of rat hippocampal dentate gyrus. J Physiol 485 (Pt 2):383-402.

Koike-Tani M, Saitoh N & Takahashi T (2005) Mechanisms underlying developmental speeding in AMPA-EPSC decay time at the calyx of Held. The Journal of Neuroscience 25: 199-207

Kopp-Scheinpflug C, Fuchs K, Lippe WR, Tempel BL, Rübsamen R (2003) Decreased temporal precision of auditory signaling n Kcna1-null mice: an electrophysiological study in vivo. J Neurosc 23: 9199-207.

Kuwada S, Fitzpatrick DC, Batra R, Ostapoff EM (2006) Sensitivity to interaural time differences in the dorsal nucleus of the lateral lemniscus of the unanesthetized rabbit: comparison with other structures. J Neurophysiol 95:1309-1322.

Lambolez B, Robert N, Perrais D, Rossier J, Hestrin S (1996) Correlation between kinetics and RNA splicing of alpha-amino-3-hydroxy-5-methylisoxazole-4-propionic acid receptors in neocortical neurons. Proc Natl Acad Scie USA 93:1797-802.

Lavine RA (1971) Phase-locking in response of single neurons in cochlear nucler complex of the cat to low-frequency tonal stimuli. J Neurophysiol 34:467-483.

Leibold C, van Hemmen JL (2005) Spiking neurons learning phase delays: how mammals may develop auditory time-difference sensitivity. Phys Rev Lett 94:168102.

Li L, Kelly JB (1992) Inhibitory influence of the dorsal nucleus of the lateral lemniscus on binaural responses in the rat's inferior colliculus. J Neurosci 12:4530-4539.

Loskota WJ, Lomax P, Rich ST (1974) The gerbil as a model for the study of the epilepsies. Seizure patterns and ontogenesis. Epilepsia 15:109-119.

Luneau CJ, Williams JB, Marshall J, Levitan ES, Oliva C, Smith JS, Antanavage J, Folander K, Stein RB, Swanson R, et al. (1991) Alternative splicing contributes to K+ channel diversity in the mammalian central nervous system. Proc Natl Acad Sci U S A 88:3932-3936.

M Constantine-Paton HC (1998) LTP and activity-dependent synaptogenesis: the more alike they are, the more different they become. Current Opinion Neurobiology 8:139:148.

Magnusson AK, Kapfer C, Grothe B, Koch U (2005) Maturation of glycinergic inhibition in the gerbil medial superior olive after hearing onset. J Physiol 568:497-512.

Malenka RC, Bear MF (2004) LTP and LTD: an embarrassment of riches. Neuron 44:5-21.

Martina M, Schultz JH, Ehmke H, Monyer H, Jonas P (1998) Functional and molecular differences between voltage-gated K+ channels of fast-spiking interneurons and pyramidal neurons of rat hippocampus. J Neurosci 18:8111-8125.

Masterton B. Diamond IT, Harrison JM, Beecher MD (1967) Medial Superior Olive and sound localization. Science 155: 1969-1967.

Mathews PJ, Jercog PE, Rinzel J, Scott LL, Golding NL (2010) Control of submillisecond synaptic timing in binaural coincidence detectors by Kv1 channels. Nat Neurosci 13:601-609.

Mayer ML, Westbrook GL, Guthrie PB (1984) Voltage-dependent block by Mg2+ of NMDA responses in spinal cord neurones. Nature 309:261-263.

McAlpine D, Grothe B Sound localization and delay lines – do mammals fit the model? Trends in Neurosciences 26:347-350.

McAlpine D, Jiang D, Palmer AR (2001) A neural code for low-frequency sound localization in mammals. Nat Neurosci 4:396-401.

McFadden SL, Walsh EJ, McGee J (1996) Onset and development of auditory brainstem responses in the Mongolian gerbil (Meriones unguiculatus). Hear Res 100:68-79.

Miller KD, Keller JB, Stryker MP (1989) Ocular dominance column development: analysis and simulation. Science 245:605-615.

Misonou H, Mohapatra DP, Park EW, Leung V, Zhen D, Misonou K, Anderson AE, Trimmer JS (2004) Regulation of ion channel localization and phosphorylation by neuronal activity. Nat Neurosci 7:711-718.

Misonou H, Mohapatra DP, Trimmer JS (2005) Kv2.1: a voltage-gated k+ channel critical to dynamic control of neuronal excitability. Neurotoxicology 26:743-752.

Monyer H, Burnashev N, Laurie DJ, Sakmann B, Seeburg PH (1994) Developmental and regional expression in the rat brain and functional properties of four NMDA receptors. Neuron 12:529-540.

Mosbacher J, Schoepfer R, Monyer H, Burnashev N, Seeburg PH, Rupperberg JP (1994) A molecular determinant for submillisecond desensitization in glutamate receptors. Science 266: 1059-62

Muennich EA, Fyffe RE (2004) Focal aggregation of voltage-gated, Kv2.1 subunit-containing, potassium channels at synaptic sites in rat spinal motoneurones. J Physiol 554:673-685.

Mulholland PJ, Carpenter-Hyland EP, Hearing MC, Becker HC, Woodward JJ, Chandler LJ (2008) Glutamate transporters regulate extrasynaptic NMDA receptor modulation of Kv2.1 potassium channels. J Neurosci 28:8801-8809.

Murakoshi H, Shi G, Scannevin RH, Trimmer JS (1997) Phosphorylation of the Kv2.1 K+ channel alters voltage-dependent activation. Mol Pharmacol 52:821-828.

Myoga MH, Beierlein M, Regehr WG (2009) Somatic spikes regulate dendritic signaling in small neurons in the absence of backpropagating action potentials. J Neurosci 29:7803-7814.

Myoga MH, Lehnert S, Leibold C, Felmy F, Grothe B (2014) Glycinergic inhibition tunes coincidence detection in the auditory brainstem. Nat Commun 5.

Nowak L, Bregestovski P, Ascher P, Herbet A, Prochiantz A (1984) Magnesium gates glutamate-activated channels in mouse central neurones. Nature 307:462-465.

Oliver DL (2000) Ascending efferent projections of the superior olivary complex. Microsc Res Tech 51:355-363.

Otis TS, Raman IM, Trussell LO (1995) AMPA receptors with high Ca^{2+} permeability mediate synaptic transmission in the avian auditory pathway. J. Physiol. 482: 309-15

Park TJ, Klug A, Holinstat M, Grothe B (2004) Interaural Level Difference Processing in the Lateral Superior Olive and the Inferior Colliculus. Journal of Neurophysiology 92:289-301.

Pecka M, Siveke I, Grothe B, Lesica NA (2010) Enhancement of ITD coding within the initial stages of the auditory pathway. J Neurophysiol 103:38-46.

Pecka M, Zahn TP, Saunier-Rebori B, Siveke I, Felmy F, Wiegrebe L, Klug A, Pollak GD, Grothe B (2007) Inhibiting the Inhibition: A Neuronal Network for Sound Localization in Reverberant Environments. The Journal of Neuroscience 27:1782-1790.

Porres CP, Meyer EMM, Grothe B, Felmy F (2011) NMDA Currents Modulate the Synaptic Input–Output Functions of Neurons in the Dorsal Nucleus of the Lateral Lemniscus in Mongolian Gerbils. The Journal of Neuroscience 31:4511-4523.

Rautenberg PL, Grothe B, Felmy F (2009) Quantification of the three-dimensional morphology of coincidence detector neurons in the medial superior olive of gerbils during late postnatal development. The Journal of Comparative Neurology 517:385-396.

Rietzel HJ, Friauf E (1998) Neuron types in the rat lateral superior olive and developmental changes in the complexity of their dendritic arbors. J Comp Neurol 390:20-40.

Roberts Michael T, Seeman Stephanie C, Golding Nace L A Mechanistic Understanding of the Role of Feedforward Inhibition in the Mammalian Sound Localization Circuitry. Neuron 78:923-935.

Rogowski BA, Feng AS (1981) Normal postnatal development of medial superior olivary neurons in the albino rat: a Golgi and Nissl study. J Comp Neurol 196:85-97.

Rosenmund C, Stern-Bach Y, Stevens CF (1998) The tetrameric structure of a glutamate receptor channel. Science 280:1596-1599.

Rothman JS, Manis PB (2003) The roles potassium currents play in regulating the electrical activity of ventral cochlear nucleus neurons. J Neurophysiol 89:3097-3113.

Rudy B, McBain CJ (2001) Kv3 channels: voltage-gated K+ channels designed for high-frequency repetitive firing. Trends Neurosci 24:517-526.

S. RyC (1907) Histologie du systeme nerveux de l'homme et des vertebrates. Paris:Malonie.

Sanchez JT, Gans D, Wenstrup JJ (2007) Contribution of NMDA and AMPA receptors to temporal patterning of auditory responses in the inferior colliculus. J Neurosci 27:1954-1963.

Sanchez JT, Ghelani S, Otto-Meyer S (2015) From development to disease: diverse functions of NMDA-type glutamate receptors in the lower auditory pathway. Neuroscience 285:248-259.

Sanes DH, Takacs C (1993) Activity-dependent refinement of inhibitory connections. Eur J Neurosci 5:570-574.

Schneggenburger R, Tempia F & Konnerth A (1993) Glutamate- and AMPA-mediated calcium influx through glutamate receptor channels in medial septal neurons. Neuropharmacology 32: 1221-8.

Schuller G, Radtke-Schuller S, Betz M (1986) A stereotaxic method for small animals using experimentally determined reference profiles. J Neurosci Methods 18:339-350.

Scott LL, Hage TA, Golding NL (2007) Weak action potential backpropagation is associated with high-frequency axonal firing capability in principal neurons of the gerbil medial superior olive. J Physiol 583:647-661.

Scott LL, Mathews PJ, Golding NL (2005) Posthearing Developmental Refinement of Temporal Processing in Principal Neurons of the Medial Superior Olive. The Journal of Neuroscience 25:7887-7895.

Seidl AH, Grothe B (2005) Development of sound localization mechanisms in the mongolian gerbil is shaped by early acoustic experience. J Neurophysiol 94:1028-1036.

Shatz CJ (1990a) Competitive interactions between retinal ganglion cells during prenatal development. J Neurobiol 21:197-211.

Shatz CJ (1990b) Impulse activity and the patterning of connections during CNS development. Neuron 5:745-756.

Shneiderman A, Oliver DL, Henkel CK (1988) Connections of the dorsal nucleus of the lateral lemniscus: an inhibitory parallel pathway in the ascending auditory system? J Comp Neurol 276:188-208.

Siveke I, Pecka M, Seidl AH, Baudoux S, Grothe B (2006) Binaural Response Properties of Low-Frequency Neurons in the Gerbil Dorsal Nucleus of the Lateral Lemniscus. Journal of Neurophysiology 96:1425-1440.

Smith AJ, Owens S, Forsythe ID (2000) Characterisation of inhibitory and excitatory postsynaptic currents of the rat medial superior olive. J Physiol 529 Pt 3:681-698.

Smith PH, Joris PX, Yin TC (1998) Anatomy and physiology of principal cells of the medial nucleus of the trapezoid body (MNTB) of the cat. J Neurophysiol 79:3127-3142.

Song P, Yang Y, Barnes-Davies M, Bhattacharjee A, Hamann M, Forsythe ID, Oliver DL, Kaczmarek LK (2005) Acoustic environment determines phosphorylation state of the Kv3.1 potassium channel in auditory neurons. Nat Neurosci 8:1335-1342.

Steinert JR, Postlethwaite M, Jordan MD, Chernova T, Robinson SW, Forsythe ID (2010) NMDAR-mediated EPSCs are maintained and accelerate in time course during maturation of mouse and rat auditory brainstem in vitro. J Physiol 588:447-463.

Stotler WA (1953) An experimental study of the cells and connections of the superior olivary complex of the cat. Journal of Comparative Neurology 98:401-432.

Svirskis G, Kotak V, Sanes DH, Rinzel J (2002) Enhancement of signal-to-noise ratio and phase locking for small inputs by a low-threshold outward current in auditory neurons. J Neurosci 22:11019-11025.

Svirskis G, Kotak V, Sanes DH, Rinzel J (2004) Sodium Along With Low-Threshold Potassium Currents Enhance Coincidence Detection of Subthreshold Noisy Signals in MSO Neurons. Journal of Neurophysiology 91:2465-2473.

Taschenberger H, von Gersdorff H (2000) Fine-tuning an auditory synapse for speed and fidelity: developmental changes in presynaptic waveform, EPSC kinetics, and synaptic plasticity. J Neurosci 20:9162-9173.

Tong H, Kopp-Scheinpflug C, Pilati N, Robinson SW, Sinclair JL, Steinert JR, Barnes-Davies M, Allfree R, Grubb BD, Young SM, Jr., Forsythe ID (2013) Protection from noise-induced hearing loss by Kv2.2 potassium currents in the central medial olivocochlear system. J Neurosci 33:9113-9121.

Tritsch NX, Rodriguez-Contreras A, Crins TTH, Wang HC, Borst JGG, Bergles DE (2010) Calcium action potentials in hair cells pattern auditory neuron activity before hearing onset. Nat Neurosci 13:1050-1052.

Tritsch NX, Yi E, Gale JE, Glowatzki E, Bergles DE (2007) The origin of spontaneous activity in the developing auditory system. Nature 450:50-55.

van der Heijden M, Lorteije Jeannette AM, Plauška A, Roberts Michael T, Golding Nace L, Borst JGerard G Directional Hearing by Linear Summation of Binaural Inputs at the Medial Superior Olive. Neuron 78:936-948.

Walger M, Hessel H, Ernst S, von Wedel H (1997) Ontogeny of electrically evoked brain stem potentials in neonatally deafened gerbils (Meriones unguiculatus) after cochlear implantation. Am J Otol 18:S15-16.

Walger M, Laska M, Schneider I, Diekmann H, von Wedel H (1993) Maturation of auditory evoked potentials in young guinea pigs with binaural conductive hearing loss. Eur Arch Otorhinolaryngol 250:362-365.

Wang LY, Gan L, Forsythe ID, Kaczmarek LK (1998) Contribution of the Kv3.1 potassium channel to high-frequency firing in mouse auditory neurones. J Physiol 509 (Pt 1):183-194.

Weiser M, Bueno E, Sekirnjak C, Martone ME, Baker H, Hillman D, Chen S, Thornhill W, Ellisman M, Rudy B (1995) The potassium channel subunit KV3.1b is localized to somatic and axonal membranes of specific populations of CNS neurons. J Neurosci 15:4298-4314.

Wenthold RJ, Petralia RS, Blahos J, II, Niedzielski AS (1996) Evidence for multiple AMPA receptor complexes in hippocampal CA1/CA2 neurons. J Neurosci 16:1982-1989.

Werthat F, Alexandrova O, Grothe B, Koch U (2008) Experience-dependent refinement of the inhibitory axons projecting to the medial superior olive. Developmental Neurobiology 68:1454-1462.

White LE, Coppola DM, Fitzpatrick D (2001) The contribution of sensory experience to the maturation of orientation selectivity in ferret visual cortex. Nature 411:1049-1052.

Woolf NK, Ryan AF (1984) The development of auditory function in the cochlea of the mongolian gerbil. Hear Res 13:277-283.

Wu SH, Kelly JB (1995) In vitro brain slice studies of the rat's dorsal nucleus of the lateral lemniscus. II. Physiological properties of biocytin-labeled neurons. Journal of Neurophysiology 73:794-809.

Yang L, Pollak GD (1994) The roles of GABAergic and glycinergic inhibition on binaural processing in the dorsal nucleus of the lateral lemniscus of the mustache bat. J Neurophysiol 71:1999-2013.

Zhang S, Trussell LO (1994) A characterization of excitatory postsynaptic potentials in the avian nucleus magnocellularis. J. Neurophysiol. 72: 705-18

Abbreviations

AMPAR – α-amino-3-hydroxy-5-methyl-4-isoxazolepropionic acid receptor

AP – action potential

DAB – diaminobenzidine

DNLL – dorsal nucleus of lateral lemniscus

EPSC - excitatory postsynaptic current

HVA channel – high voltage activated potassium channel

IC – inferior colliculus

Ih – hyperpolarization activated cation channel

ILD – interaural level intensity

ITD – interaural time intensity

IPSP – inhibitory postsynaptic potential

Kv channel – voltage gated potassium channel

LSO – lateral superior olive

LTD – long-term depression

LTP – long-term potentiation

LVA channel – low voltage activated potassium channel

mEPSC – miniature excitatory postsynaptic current

MNTB – medial nucleus of traperoid body

MSO – medial superior olive

NMDAR – N-Methyl-D-Aspartat receptor

P – postnatal day

PBS – phosphate buffered saline

PFA – paraformaldehyde

SOC – superior olivary complex

STDP – spike time dependent plasticity

Eidesstattliche Versicherung / Affidavit

Hiermit versichere ich an Eides statt, dass ich die vorliegende Dissertation „Structure function relationships in the auditory brainstem“ selbstständig angefertigt habe, mich außer der angegebenen keiner weiteren Hilfsmittel bedient und alle Erkenntnisse, die aus dem Schrifttum ganz oder annähernd übernommen sind, als solche kenntlich gemacht und nach ihrer Herkunft unter Bezeichnung der Fundstelle einzeln nachgewiesen habe.

I hereby confirm that the dissertation „Structure function relationships in the auditory brainstem“ is the result of my own work and that I have only used sources or materials listed and specified in the dissertation.

München, den

Munich, date

Contributions

Potassium channel expression in the mature MSO

The contributions to this project were the following: the idea for the project came from my supervisor Prof. Dr. Felix Felmy. I managed project organization, realization and literature research for further steps. These points were discussed on a regular basis with my supervisor. I supervised the master student, which included the preparation of procedure sheets for perfusion, antibody protocols, imaging and analysis. I taught her all the methods needed for this project and prepared a weekly plan for the first 6 weeks. For the results shown here, I supervised all of the taken steps including the imaging and image procession. Subsequent image analysis with semi-quantitative analysis was the idea of my supervisor and performed by Alisha Nabel under the supervision of Prof. Dr. Felix Felmy. I was present during meetings and took part in discussions on data. Alisha Nabel, under the supervision of Prof. Dr. Felix Felmy, assembled the final graph showing the channel distribution (Figure 15).

Development of calcium entry sites in the MSO

Contributions towards this project: Experimental design for calcium imaging and electrophysiology towards fiber stimulation experiments came from my supervisor Prof. Dr. Felix Felmy. The idea for minimal fiber stimulation, GluR2 rectification experiments and initial thoughts on activity-dependency experiments came from me. Final experimental design for noise box experiments was evolved together with Delwen Franzen and Prof. Dr. Felix Felmy. All cells for fiber

stimulation (in total: control: n = 44; noise box: n = 17) were recorded and analyzed by myself for the control and noise box condition. Two of the nine recorded cells for P11 minimal fiber stimulation experiments in control condition were recorded by my colleague Delwen Franzen. Additionally, for the noise box condition three of the P14 cells (n = 7) and three of the P17 cells (n = 7) were recorded by her. I recorded all other cells. All of these cells were analyzed by myself. All analysis and figure generation were done by myself. Calcium imaging analysis procedures were written in Matlab in collaboration with Christian Kellner.

All immunohistochemical stainings were planned, performed, imaged and further processed by me. In addition, all cells towards the analysis of the rectification index for AMPAR currents were recorded and analyzed by myself. All shown figures were generated by myself.

NMDAR driven modification of binaural processing in the mature DNLL

Contribution towards this project: Experimental design came from my supervisor Prof. Dr. Felix Felmy. Introduction to setup and experimental procedure was done mainly by Helge Gleiss and partly by Dr. Ida Siveke. Dr. Annette Stange gave a short introduction to iontophoretic drug application and multi-barreled electrode construction. All of the shown cells for baseline and drug experiments were recorded by me. I built all of the used multi-barreled electrodes. Acoustic stimuli were generated together with Dr. Todd Jennings. The first steps of data analysis were done by myself in self-written Matlab programs, and graph

generation for figure 28, 29 and 30 were done in these programs by myself. Dr. Ida Siveke did final analysis and figure generation, as shown in Figure 31, 32 and 33. Discussions on data analysis were always held together with Prof. Dr. Felix Felmy, Dr. Ida Siveke and Ph.D. Julian Ammer. Immunohistochemical stainings were performed, imaged and processed by myself.

_____ _____

Prof. Dr. Felix Felmy Sarah Gleiss

Acknowledgments

Thank you …

… Felix Felmy for being the best supervisor I could think of. Especially your never-ending enthusiasm for science has always been a great motivation and made it a lot of fun to work with you. Your knowledge and your way of looking at data and immediately understanding a million things that I could not always follow immediately have always been impressing and inspiring. Hopefully I have learned only bits of this way of thinking.

… Benedikt Grothe, for your support and always-helpful input. Thank you for enabling a look into a third floor that has all the techniques one can dream of and giving me the possibility to learn as many as I could.

… Florence Bareyre, Christian Lohmann and Michael Pecka for valuable input and discussions during my thesis committees.

… Ida Siveke for showing me the *in-vivo* world and collaboration that was a lot of fun, including late night recordings with alcohol-free beer and crisps.

… Alisha Nabel for being a nice, hard working and always happy Master student and most of all a colleague; I enjoyed working with you a lot.

… Helge Gleiss, Annette Stange-Marten and Todd Jennings for their help on the *in-vivo* setup, building multis, programming, etc.

… Christian Kellner for collaboration in the calcium influx project, it was a lot of fun. Special thanks for your patience in explaining Matlab to a complete naïve person.

… Christian Lohmann for collaboration that was not part of this project but an interesting insight into the imaging world.

… Mike Myoga, Christoph Kayser Martina Blunder and Helge Gleiss for proofreading and critical, helpful comments. I know it was not easy with me and my writing, thanks for your patience.

… GSN office team for their help, instantaneous reimbursements and the organization of all the wonderful social events. It was a great time being part of this school.

… the whole Felmy lab but especially Franzi, Delwen and Stephan who were always there to help, talk, support and motivate whenever necessary. It was so much fun to work with you and I will miss it a lot!

… all the people on the third floor for their help, support and interesting discussions in the kitchen. Especially to the people that made all this possible by keeping everything up and running and always having an open ear for me: Franziska, Monika, Sabrina, Horst and Simone. But especially to Hilde, Olga and Dieter for so much help with basically anything.

… den besten Eltern und der besten Schwester der Welt. Ihr habt alles möglich gemacht und mich so tatkräfitg unterstützt, dass ich meine Arbeit nicht nur anfangen sondern auch fertig stellen konnte. Danke für euren niemals endenden Glauben an mich.

… den lieben Schwiegereltern die immer tatkräftig zur Seite standen und es mir somit ermöglichten mit (eigener) Familie fertig zu promovieren.

… Helge für deine schier endlose Geduld mit mir. Du hast mich immer wieder motiviert und unterstützt im Glauben an mich selbst.

… Luisa du musstest einiges an gemeinsamer Zeit opfern damit ich weitermachen konnte, aber du warst meist verständnisvoll und kooperativ.

List of publications

Gleiss SA*, Franzen DL*, Berger C*, Kümpfbeck FS, Ammer JJ, Felmy F (2015) Development and modulation of intrinsic membrane properties control the temporal precision of auditory brain stem neurons. Journal of Neurophysiology

* these authors contributed equally

Trattner B, Berner S, Grothe B, Kunz L. (2013) Depolarization-induced suppression of a glycinergic synapse in the superior olivary complex by endocannabinoids. Journal of Neurochemistry

In preparation:

Siveke I*, Ammer JJ*, Gleiss SA, Lingner A, Grothe B, Leibold C, Felmy F. NMDA Receptor currents adjust binaural processing in the adult auditory brainstem.

* these authors contributed equally